Universidad
Carlos III de Madrid

PhD. Thesis

Synthesis of carbon nanomaterials by catalytic chemical vapor deposition: Growth mechanisms on metal powders and foils

Author:

Pablo Romero Rodríguez

Director:

Dr. Roberto Guzmán de Villoria

A thesis submitted for the degree of Doctor of Philosophy

Departamento de Ciencia e Ingeniería de Materiales e Ingeniería Química

Universidad Carlos III de Madrid

January 13th 2017, Leganés

Universidad Carlos III de Madrid

TESIS DOCTORAL

Synthesis of carbon nanomaterials by catalytic chemical vapor deposition: Growth mechanisms on metal powders and foils

Autor: Pablo Romero Rodríguez

Director: Dr. Roberto Guzmán de Villoria

Firma del Tribunal Calificador:

Firma:

Presidente:

Vocal:

Secretario:

Calificación:

Leganés, 13 de Enero de 2017

A Isabel,
por ayudarme a verlo claro.

Acknowledgements

I am very grateful to my supervisor, Dr. Roberto Guzmán de Villoria, for his help and trust, which has been an endless source of courage during my PhD.

I am thankful to all the people behind the collaborations raised during these four years, specially to Professor José Manuel Torralba, Dr. Raquel Oro and Dr. Mónica Campos for their collaboration and help at the beginning of this work. This gratitude is extended to Dr. Yuwen Cui and Dr. Guanglong Xu. This thesis presents a great deal of work carried out in collaboration with Dr. Pablo Aitor Postigo, Estela Baquedano, Dr. Javier Martínez, Dr. Alberto Boscá, Blanca Jalvo, Dr. Javier Santiago-Morales, Dr. Roberto Rosal, Dr. Ignacio Martín Gullón, Dr. Adrián Gómez and Dr. Ignacio Carabias. Thank you very much for your time and interest in my PhD studies.

In this moment, I also remember the scientific instructions from Dr. Miguel Monclús, Dr. Jon Molina, Dr. Juan Pedro Fernández, Dr. Manuela Cano as well as the constructive conversations with my thesis colleagues Fernando Naya, Arcadio Varona, Luis Herrera and Angel Alvaredo. I would like to highlight the exceptional technical work and support I received from Juan Carlos Rubalcaba, Vanesa Martínez, José Luis Jiménez, Marcos Angulo, Miguel de la Cruz and Miguel Castillo. From the personal point of view, these years have been a real gift and I will always remember the variety of exciting conversations we have shared at IMDEA Materials.

Finally, I would like to thank my close friends and family for their unconditional support and understanding.

Preface

This dissertation is submitted for the degree of Doctor of Philosophy to the "Universidad Carlos III" (Madrid). It is based on the work carried out at IMDEA Materials Institute (Madrid) between October 2012 and September 2016, under the supervision of Dr. Roberto Guzmán de Villoria.

This work was also supported by collaborations with Dr. Raquel Oro (TU Wien, Viena), Dr. Mónica Campos ("Universidad Carlos III", Madrid), Professor José Manuel Torralba (IMDEA Materials, Madrid), Dr. Yuwen Cui (IMDEA Materials, Madrid) and Dr. Guanglong Xu (IMDEA Materials, Madrid) in those aspects relating to characterization of metal catalysts and Dr. Ignacio Martín-Gullón (Universidad de Alicante) for the thermal treatments and characterization of carbon nanofibres. Those tasks relating to electrical and optical characterization of carbon thin films were carried out under collaborations with Dr. Pablo Aitor Postigo ("Instituto de Microelectrónica", Madrid), Estela Baquedano ("Instituto de Microelectrónica", Madrid), Dr. Javier Martínez (ISOM, Madrid), Dr. Alberto Boscá (ISOM, Madrid), and Blanca Jalvo ("Universidad de Alcalá", Madrid), Dr. Javier Santiago-Morales ("Universidad de Alcalá", Madrid) and Dr. Roberto Rosal ("Universidad de Alcalá" and IMDEA Water Institute, Madrid) for experiments to characterize surface wettability of carbon thin films.

This work starts with an introductory Chapter I which reviews some existing carbon nanomaterials and their production by chemical vapor deposition, followed by the statement of objectives in Chapter II. In Chapter III, main experimental techniques used along the thesis are explained. Results are presented in Chapters IV, V and VI, which focuses on the synthesis of carbon fibres and nanofibres on pure nickel and $Fe_{64}Ni_{36}$ powders, vertically aligned carbon nanotubes on stainless steel foils and carbon thin films on copper foils, respectively. Finally, physical properties of the carbon thin films described in Chapter VI are analysed in Chapter VII, which focuses on the characterization of the electrical and optical conductivities, on the surface wettability properties and on a highly scalable polymer-assisted transfer process by thermal shocks.

The results obtained during the course of this PhD thesis, by the moment of its submission, have led to three peer-reviewed manuscripts which have been published in top international journals, three submitted manuscripts, another one under preparation and a patent application in the Spanish Patent Office (OEPM):

- **P. Romero**, R. Oro, M. Campos, J. M. Torralba, R. Guzmán de Villoria. "Simultaneous synthesis of vertically aligned carbon nanotubes and amorphous carbon thin films on stainless steel", Carbon 82 (2015) 31–38.
- **P. Romero**, P.A. Postigo, E. Baquedano, J. Martínez, A. Boscá, R. Guzmán de Villoria. "Controlled synthesis of nanocrystalline glass-like carbon thin films with tuneable electrical and optical properties", Chemical Engineering Journal 299 (2016) 8–14.
- B. Jalvo, J. Santiago-Morales, **P. Romero**, R. Guzmán de Villoria, R. Rosal. "Microbial colonization of transparent glass-like carbon films triggered by a reversible radiation-induced hydrophobic to hydrophilic transition", RSC Advances 6 (2016) 50278-50287.
- **P. Romero**, I. Martín-Gullón, R. Guzmán de Villoria. "Strong temperature effect on the synthesis by chemical vapor deposition of high-yield multi-armed carbon microstructures and graphite-covered nickel micro/nanoparticles", *under review*.
- **P. Romero**, Guanglong Xu, Yuwen Cui, R. Guzmán de Villoria. "Direct synthesis of carbon nanostructures on $Fe_{64}Ni_{36}$ micro-particles by CVD", *under review*.
- N. Rodríguez-Losada, **P. Romero**, R. Guzmán de Villoria, J. A. Aguirre. "Cell survival and differentiation with nanocrystalline glass-like carbon using substantia nigra dopaminergic cells derived from transgenic mouse embryos", *under review*.
- **P. Romero**, R. Guzmán de Villoria. "Polymer-assisted thermal shock delamination of CVD carbon thin films from copper foils", *manuscript in preparation*.
- R. Guzmán de Villoria, **P. Romero**. "Process for obtaining carbon fibres using polyhedral Ni or Ni alloys microparticles", Application P201530731 (May 27th 2015, *patent pending*).

This work has also been well received by experts at International Conferences, workshops and seminars in the field of carbon materials and composites:

- **P. Romero**, J. C. Rubalcaba, R. Guzmán de Villoria. "Síntesis de nanotubos de carbono verticalmente alineados para su uso como refuerzo en materiales compuestos", X Congreso Nacional de Materiales Compuestos, Matcomp'13. Algeciras, Spain (July 2013).
- **P. Romero**, R. Oro, M. Campos, J. M. Torralba, R. Guzmán de Villoria. "Synthesis of Vertically Aligned Carbon Nanotubes and Nanocrystalline aC Film on Stainless Steel by Chemical Vapour Deposition", MRS Fall Meeting & Exhibit. Boston, Massachusetts (December 2014).
- **P. Romero**, R. Oro, M. Campos, J. M. Torralba, R. Guzman de Villoria. "Carbon Nanotube/Carbon Film Nanostructures for Nanoengineered Composites", Carbon Conference. Dresden, Germany (July 2015).
- **P. Romero**, R. Oro, M. Campos, J. M. Torralba, R. Guzman de Villoria. "Híbrido de Nanotubos de Carbono Verticalmente Alineados y Película de Carbono y su potencial uso en Materiales Compuestos", XI Congreso Nacional de Materiales Compuestos, Matcomp'15. Madrid, Spain (July 2015).
- Two internal seminars, IMDEA Materials Institute, Madrid, Spain (November 2014, February 2016).

Abbreviations

ΔG	Gibbs free energy
∆E	Binding energy
AFM	Atomic force microscopy
AO	As-oxidized
AR	As-received
BCC	Body centered-cubic lattice
CA	contact angle
cCVD	Catalytic Chemical vapor deposition
CNF	carbon nanofibre
CNT	carbon nanotube
CVD	Chemical vapor deposition
E_a	Activation energy
EBSD	Electron backscatter diffraction
EDS	energy-dispersive X-ray spectroscopy
FCC	face centered-cubic lattice
FIB	Focused ion beam
FWHM	Full width half maximum
ITO	indium tin oxide
La	graphite in-plane crystal
Lc	graphite stacking crystal sizes
LPE	liquid phase exfoliation
MD	Metal dusting
Q	Total flow rate
RH	Room humidity
sccm	Centimetre squared per minute at standard conditions
SEM	Scanning electron microscopy
TCE	Transparent conductive electrodes
TEM	Transmission electron microscopy
UV	Ultraviolet
XPS	X-ray photoelectron spectroscopy
XRD	X-ray diffraction

Resumen

Actualmente, las excelentes propiedades proporcionadas a escala nanométrica por los nanomateriales de carbono, como nanotubos y grafeno, motivan la propuesta teórica de un gran número de aplicaciones. Estos nanomateriales se pueden producir por deposición química en fase vapor (CVD), que consiste en la descomposición térmica de hidrocarburos sobre catalizadores metálicos. La técnica de CVD permite, a través del control de las condiciones de síntesis y la composición y morfología del catalizador, la producción controlada de estructuras altamente organizadas como nanotubos de carbono verticalmente alineados o formando una fibra continua, así como películas de un único átomo de espesor. Sin embargo, la producción de catalizadores altamente controlados requiere técnicas de alto coste y difícilmente escalables a nivel industrial. Una alternativa es la síntesis directa y de bajo coste empleando catalizadores metálicos comerciales en forma de polvo o placa para la producción de nanomateriales de diferentes morfologías y cristalinidades. A pesar de que esta alternativa ya se ha demostrado con anterioridad, la mayoría del trabajo experimental publicado se centra en la caracterización del carbono producido, y existe una necesidad de estudios experimentales enfocados en el mecanismo de crecimiento de nano-estructuras sobre estos catalizadores. En este trabajo, se presenta el uso de polvos metálicos de base níquel y de placas de acero y cobre, como catalizadores de bajo coste para la producción de nanomateriales de carbono por la técnica de CVD. Se demuestra la obtención de nanofibras, nanotubos verticalmente alineados y películas delgadas, así como los mecanismos de crecimiento en cada una de los catalizadores empleados. Finalmente, se demuestra un proceso de producción de películas poliméricas compuestas de películas delgadas de carbono amorfo con alto potencial de escalado industrial, lo que amplía la lista de carbonos nano-estructurados disponibles con potencial uso como superficies multifuncionales.

Abstract

Carbon nanomaterials such as carbon nanotubes (CNTs) or monolayer graphene are proposed for a wide variety of theoretical applications due to the superior properties provided at the nanoscale. They can be produced by chemical vapor deposition (CVD), which consists on the thermal decomposition of hydrocarbons over metal catalysts. Highly ordered structures like CNTs arrays and fibres as well as large-area monolayer graphene films can be grown in a highly controlled manner at laboratory scale by selecting the proper CVD conditions, the metal catalyst composition and morphology. However, the highly controlled catalysts needed for their synthesis are currently produced by expensive techniques which are hard to scale. Alternatively, the use of commercially available bulk metal catalysts like powders, foils and meshes are shown to be a fast and low cost approach for the production of carbon nanomaterials with several morphologies and crystallinities. This alternative is already demonstrated in the literature, however most of the experimental work on synthesis on bulk metals focuses on the carbon produced, and there is a need of experimental work focused on growth mechanisms of carbon nanomaterials on these metal catalysts. We used nickel-based powders and stainless steel and copper foils for the production of carbon fibres, nanofibres, CNTs arrays and thin films by CVD, providing supported explanations on the carbon nanostructure growth mechanisms. Highly scalable processing developments in the production of graphene-based composite thin films are also presented, which expand the available portfolio of nanostructured carbon materials with potential applications in multifunctional surfaces.

Contents

1
Introduction

1.1. Carbon materials, bonding and structures

The carbon atom holds six electrons with a $1s^2 2s^2 2p^2$ configuration, the latest four of which are valence electrons ($2s^2 2p^2$). Since the energetic difference between 2s and 2p orbitals is low compared to the energy released when the chemical bonding takes place, these orbitals can totally or partially mix to form sp hybridized orbitals (σ bonds). As shown in the **Figure 1**a, sp^3 hybrid orbitals form a tetrahedron and give rise tetrahedral carbon networks like diamond, sp^2 hybrid orbitals give rise to planar structures like graphite and sp hybridized carbon form linear chains like carbyne. The p orbitals not taking part in sp^2 or sp hybridization, form additional π bonds.

Ideally, graphite (sp^2) is a repetition of layers (*xy* plane) stacked in *z* direction by Van der Waals interactions (**Figure 1**b). Individual layers, known as graphene, are composed of one-atom-thick honey-comb lattice of carbon atoms placed at the corners of regular hexagons. Each atom is bonded to three carbon atoms by three σ bonds, and since only three out of four valence electrons are participating in the hybridization, the remaining electron forms the π bond constituting a delocalized cloud over and below the graphene layer. This in-plane bonding gives graphene and graphite high electrical and mechanical properties along the graphite in-plane direction. Such configuration results in a distance between adjacent atoms in a graphene layer of ~0.1415 nm and the distance between two graphene layers of ~0.3354 nm [1].

Because the weak interaction between graphene layers along the *z* direction, these layers can translate forming two modifications of graphite; the hexagonal or α-graphite, where individual graphene layers are sequenced in ABAB stacking and B-layer atoms situated in the centre of A-layer atoms (**Figure 1**b), and the rhombohedral or ß-graphite (frequent in natural graphites) stacked in an ABCABC. ß-graphite can be transformed into α-graphite by heat up above 1000ºC.

Due to stacking disorder in real graphites, interplanar distance of some layers may increase up to ~0.344 nm, decreasing the interaction between graphene layers and enabling their rotation around z axis, creating the so-called turbostratic graphite. Graphitic materials are usually characterized by the length of their crystals along the in-plane direction (L_a) and the stacking direction (L_c).

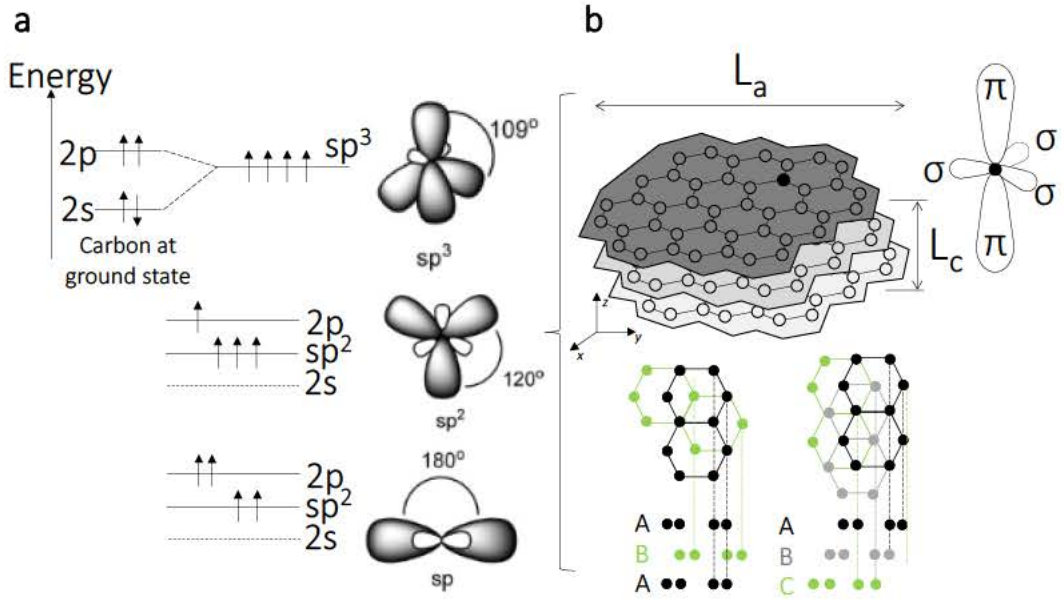

Figure 1 Hybridization of carbon [1] (a) and structure of graphite based on the sp^2 hybridization (b).

The sp^2 hybridization presented in **Figure 1**b gives rise to a wide variety of graphitic materials depending on the crystal size (L_a, L_c), the orientation/order of these crystals, and the morphology/shape of the structure to which they belong. One of the most well-known sp^2-bonded carbon materials used in engineering are the carbon fibres used to reinforce polymers in aerospace applications. These fibres are mainly composed by graphitic crystals aligned parallel to the length axis **(Figure 2**a). This alignment grants the combination of good thermal and mechanical properties along the fibre axis, and the more crystalline and parallel the graphitic planes, the better the electrical, thermal and mechanical properties.

Besides the good properties of long-range order crystalline graphite (large in-plane crystal size L_a), there are amorphous carbon materials of interest in engineering which represents the great ability of carbon to exist and to perform good properties with different microstructures. Among them, there are two that may be highlighted

due to their industrial relevance. The first is soot, also known as carbon black, which is used to increase wear and tear resistance on rubber tires. It is a turbostratic graphitic material (mostly sp^2 bonded) whose interplanar distance is expanded up to ~0.344 nm. Carbon black forms a powder composed by nanoparticulate aggregates from 2 to 300 nm, whose graphitic planes are stacked like roof tiles (**Figure 2**b). The second example of carbon material with amorphous microstructures is glass-like or glassy carbon, which is composed by ribbon and fullerene-like entangled domains (**Figure 2**c). This microstructure gives these materials high hardness, impermeability to gases and liquids as well as excellent chemical resistances. Glass-like carbons are widely used as electrode in electrochemistry.

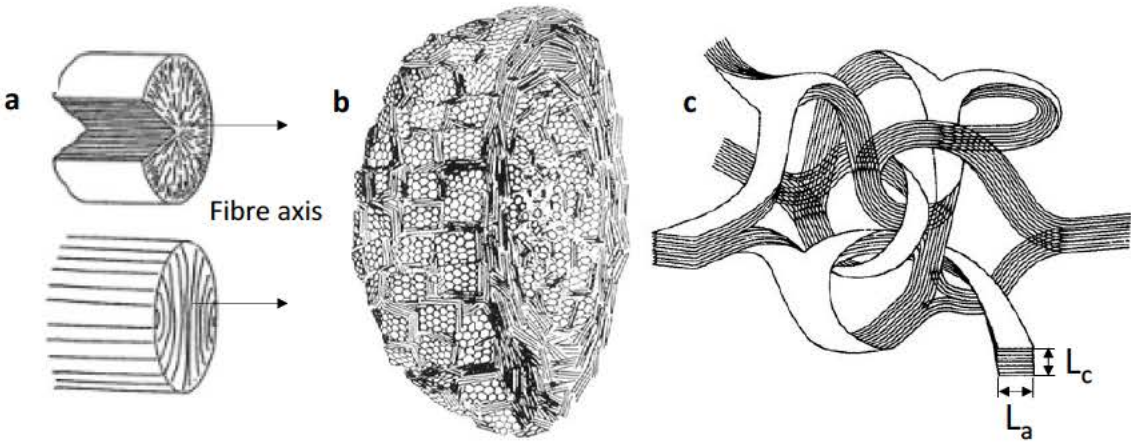

Figure 2 sp2-bonded carbon materials used in engineering, like (a) carbon fibres [1], (b) carbon black [2] and (c) glass-like carbon [3].

1.2. Carbon nanomaterials

Beside macroscopic carbon materials and similar to carbon black, carbon also forms other materials and structures with single units sized between 1 and 1000 nm in at least one direction. These nanostructures are also called carbon nanomaterials, and may form 1-atom-thick films and fibres with diameters down to 1 nm. The strong interest in the last two decades on carbon nanomaterials is based on their ability to provide different and enhanced properties at nanoscale compared to bulk, and their nanometer-size makes them excellent candidates to provide multifunctional properties to superior structures [4], [5]. The explanation of the most well-known carbon nanomaterials is presented in the next section, highlighting the difference

between nanofibres and thin films, both showing highly crystalline and amorphous microstructures.

1.2.1. Nanotubes and nanofibres

A carbon nanotube (CNT) can be visualized as a rolled up graphene layer or layers forming a cylindrical cavity with a nanometre-sized diameter [6], [7], with the graphite planes parallel to the fibre length axis. Several types of CNTs have been found depending on the number of graphene layers (single-wall or concentric multi-wall) and the graphene rolling direction (**Figure 3**a). Diameters range from 0.4 nm to 15 nm in single-wall CNT and from 10 nm to 100 nm in multi-walled CNT [1], [8], with lengths reaching cm-scale resulting in outstanding aspect ratios of length/diameter up to 10^7 [9]. Since the properties of CNTs strongly depend on their diameter, number of walls and the rolling direction, a large dispersion of values can be extracted from the literature, highlighting electrical conductivities up to 10^7 S/m [10] (of the order of copper), thermal conductivities up to 5800 W/mK [11], [12] (greater than graphite), Young's modulus greater than 1 TPa [13] and strength up to 63 GPa [14], [15] (greater than steel).

Besides CNTs, where the graphite plane is parallel to the fibre length axis forming a cylindrical cavity, there are a wide variety of nanofilaments not exceeding 500 nm in diameter with different graphite crystal orientations (**Figure 3**b), known as nanofibres [16]. Most common carbon nanofibres are platelet nanofibers (composed of small graphene layers, perpendicularly disposed to the fibre axis), fishbone hollow core nanofibers (where the graphene layers are inclined with respect to the fibre axis, with an either a hollow or a solid core), ribbon nanofibers (straight and unrolled graphene layers parallel to the fibre axis with non-cylindrical cross-sections) and stacked-cup nanofibers (formed by individual and continuous nanocones stacked along the longitudinal direction of the fibres). Given the lack of long range continuity of the graphite crystal (L_a) in carbon nanofibers, lower values of their physical properties compared to CNTs are displayed, like Young Modulus up to 0.245 TPa, mechanical strength of 2.9 GPa [17], electrical conductivity in the range of 10^3 - 10^4 [18] and thermal conductivity up to 449 W/mK [19].

1.2.2. Graphene and amorphous thin films

Graphene can be considered the "simplest" carbon nanomaterial due to its symmetry and bidimensionality, consisting on one-atom-thick sheet of carbon atoms densely packed into a benzene-ring structure forming a sp^2-bonded honey-comb lattice (**Figure 3**d). Few-layer graphene was first experimentally studied in 2004 [20], and widely analysed since then, showing a wide range of unique properties such a very high electrical conductivity (10^8 S/m) [21] (greater than copper), near zero and tuneable bandgap, thermal conductivity up to 5300 W/mK [22]–[25] (greater than graphite), tensile modulus up to 1 TPa and mechanical strength up to 130 GPa (greater than steel), and optical transmittance of 97,7% of visible light [26].

Graphene is probably the most extensively studied carbon nanomaterial at the moment of this work, however alternative nanometre-thick amorphous carbon thin films showing a high dispersion of properties are found in the literature [27]. Diamond-like carbon (with a significant fraction of C–C sp^3 bonds) and glass-like carbon (100% sp^2 bonds with entangled microstructures) are some examples which are currently manufactured as thin films with thicknesses of few nm. Due to their amorphous nature, their properties are well below those of graphene, showing thermal conductivity of 0.374 W/mK [28], electrical conductivity up to 10^4 S/m [29], Young modulus up to 62 GPa and tensile strength of 870 MPa [30]. Despite mechanical and transport properties are not competitive as compared to graphene and CNTs, amorphous and glass-like carbons combine interesting properties such as high temperature stability, extreme resistance to chemical corrosion, high hardness, low density, and high impermeability to both gases and liquids [2], [31], [32]. A summary of the properties of the described materials is presented in Table 1.

Table 1 Summary of the properties per carbon material.

Material	Electrical Conductivity (S/m)	Thermal Conductivity (W/mK)	Young Modulus (TPa)	Tensile Strength (GPa)
Nanofilaments				
CNT	10^7	5800	1	63
CNF	10^3-10^4	449	0.245	2.9
Thin Films (nm thickness)				
Graphene	10^8	5300	1	130
Amorphous carbon	10^4	0.374	0.062	0.870
Bulk and references				
Graphite	10^6 (in-plane)	4000 (in-plane)	0.03	0.08
Carbon fibres	10^4-10^5	500	0.450	3-6
References	$6 \cdot 10^7$ (Copper)	2000 (Diamond)	0.2 (Steel)	1 (Steel)

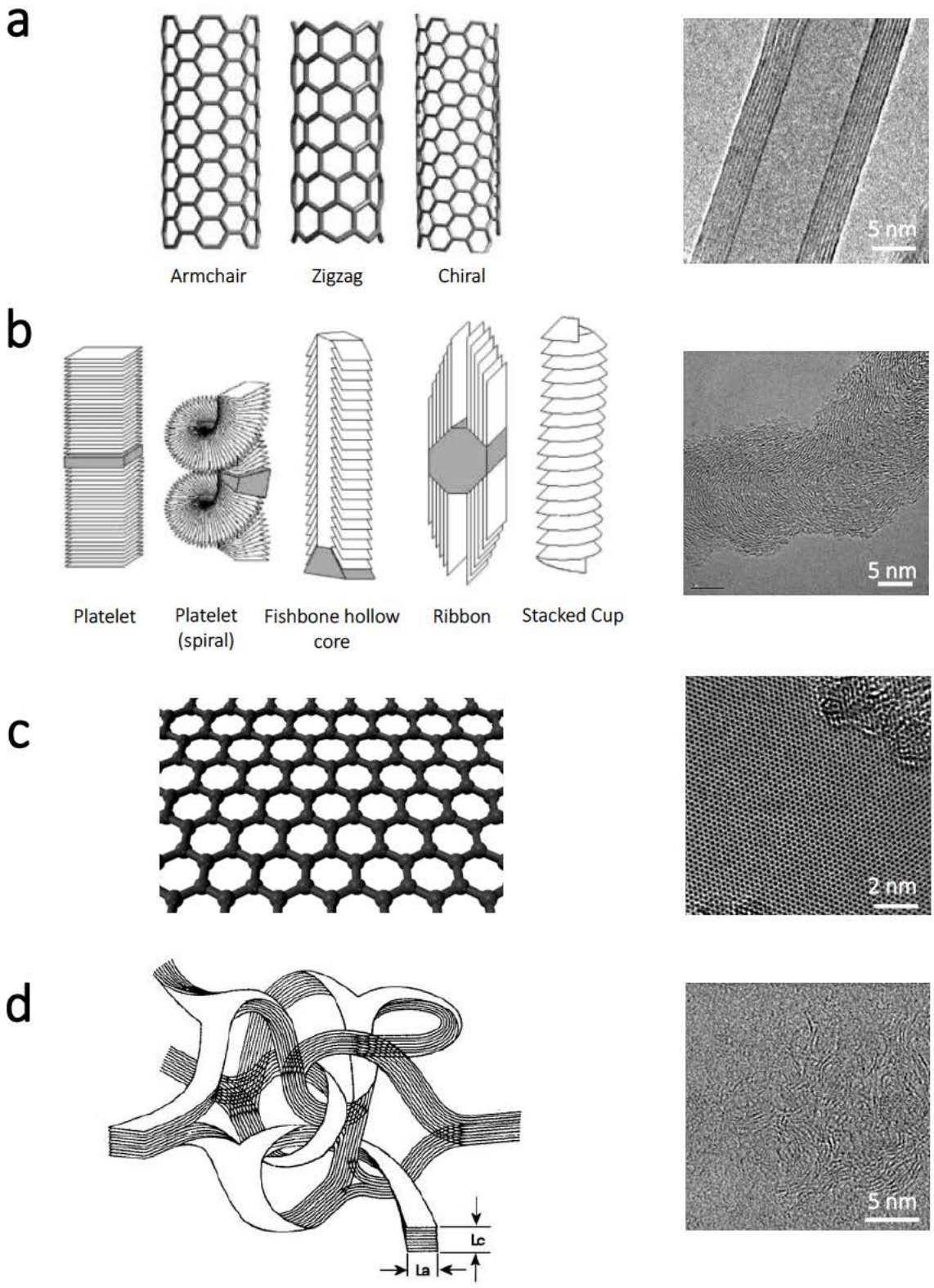

Figure 3 Main carbon nanomaterials (idealized on left and imaged by a transmission electron microscope on right). Carbon nanotubes (a), nanofibres [16] (b), graphene (c) and glass-like carbon (d).

1.2.3. Potential applications

Carbon nanomaterials may be classified by two general parameters, i) the quality or crystallinity (highly crystalline vs amorphous materials), and ii) the shape (powder vs aligned materials like fibres or films). For example, the crystallinity of carbon nanomaterials for batteries or supercapacitors is "the opposite" to those required for high performance electronics, where highly crystalline graphene films are demanded [4], [5]. It is important to highlight the different readiness level of each carbon nanomaterial and the respective issues found in their integration in real applications. Major problems are found in maintaining their properties upon up-scaling as well as on their mass production at reasonable cost. A brief description of some applications and related issues is presented in next paragraphs.

Carbon nanotubes and nanofibers

Powders of CNTs and CNFs are widely studied as fillers for the reinforcement of polymer matrixes. Despite their mass production is already demonstrated and offers competitive prices and yields [4], [33], [34], the full potential of CNTs and CNFs as mechanical reinforcement is currently limited due to their poor dispersion within the polymer matrix, which result in poor mechanical properties [35], [36]. Also, CNTs surfaces are chemically stable and interact with the matrix mainly through van der Waals forces, which are unable to provide an efficient load transfer across the filler/matrix interface, and chemical functionalization might be required to improve the adhesion. Similar problems are found when using graphene powders. On the other hand, nanomaterials in powder shape are facing toxicity issues in contact with organisms in significant quantities [37], [38]. Thus from a technical point of view, the challenge for polymer reinforcement with CNTs and graphene powders is their homogeneous dispersion and the efficient adhesion with the matrix.

The high porosity and surface area together with high electrical conductivity are highly demanded in energy storage and production systems (lithium-ion batteries, supercapacitors or fuel cells). However, carbon materials showing porous size <2 nm appear to be unsuitable for Li-ion battery electrodes, because the bigger the pore size, the higher the irreversible capacity. That is the case of CNTs, which provide a gradual loss of capacity that is unacceptable for Li-ion batteries, and have a limited

application in supercapacitors due to the lack of microporosity [38]. Alternatively, CNTs and CNFs may be useful as a conductive support for inorganic catalysts, giving rise to hybrid functional inorganic compounds with great potential in photocatalysis [39].

CNTs powders are currently applied in several commercial products like running shoes, golf shafts, armor vests, electromagnetic shielding materials, bicycles, filtration membranes [4].

Graphene films and powders

Transparent electrodes are highly demanded for electronic devices/displays and photovoltaics. Materials used in these applications should have high electrical conductivities and transparency, must be colourless, low cost and occasionally must be flexible (car windows and consumer electronics [40]–[42]). Despite transparent conductive oxides like indium tin oxide (ITO) dominates the industry, carbon nanotube networks and graphene films are currently being investigated, which provide the advantage of being highly flexible [43]. Nowadays, high quality continuous graphene films produced in the laboratory are the best carbon-based candidates that approaches ITO´s performance, with 97.4% of optical transmittance coupled with sheet resistance of 125 Ω/□ [43]. Unfortunately their production, transfer and integration are still in its infancy [5]. Graphene also enables the manufacturing of devices with extremely thin channels, and is considered a candidate for post-Si electronics by the International Technology Roadmap for Semiconductors [5]. High quality SWNTs can also be used to build thin-film transistors (TFTs) for organic light-emitting diode (OLED) displays, and may replace copper microelectronic interconnects and function both as electrical leads and heat sinks for use in high-power amplifiers. In summary, transparent conductive electrodes and electronic devices can be considered as one of the most demanding applications for carbon nanomaterials in terms of crystallinity and defect-free production process.

Currently, graphene powders are applied in several products such as graphene based inks, tennis rackets, skis, thermal pastes, bicycle race wheels, cycling helmets, cycling shoes [44] and lightbulb (Graphene Lighting PLC).

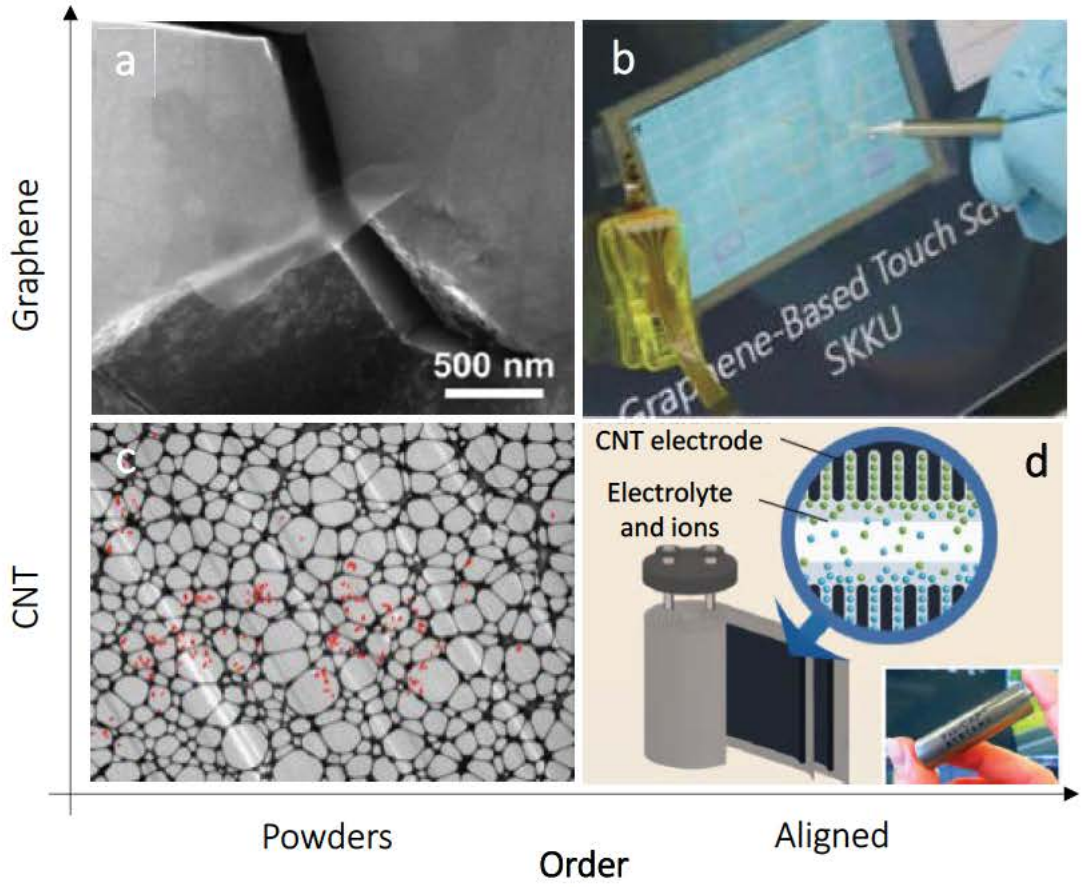

Figure 4 Emerging CNT and graphene applications depending on ordering. a) Mechanical and electrical reinforcement of Al_2O_3 with graphene powders [45], b) touch-screen panels with graphene films [43], c) Mechanical and electrical reinforcement of polymers with CNTs powders poorly dispersed and d) concept for supercapacitors based on CNT forests [46].

Other proposed applications for CNTs, CNFs and graphene are as sensors to detect chemical substances, forces, optical, electric and magnetic signals in industrial monitoring and surveillance, point-of care, environmental monitoring, etc [5]. Surfaces coated with multiwalled CNTs are currently designed for biofouling, anticorrosion applications and water purification membranes, meanwhile graphene coatings are shown to increase by a factor of four the heat transfer coefficient of copper tubing in heat exchangers [47].

Ad-hoc carbons and new applications

Despite highly crystalline CNTs or graphene are currently in the spotlight of the nanocarbons research, other carbon nanomaterials such as amorphous or glass-like carbon thin films are being investigated because they provide alternative properties

complementary to CNT and graphene. In fact, glass-like carbons in bulk state are already used in industry as electrodes due to their combination of high temperature stability and extreme resistance to chemical corrosion. Also, functional devices are being developed making use of glass-like carbon thin films for micromechanical systems [48], [49], catalysis [50], air separation [51], flexible neuroelectronic implants for dopamine sensing [52] or energy-storage applications [12], [54].

Beside improvement of existing technologies, carbon nanomaterials are expected to enable the emergence of new technologies in the future. The most inexpensive carbon-based materials and with the least requirements would be the first available (flexible solar cells, batteries and supercapacitors) while devices which require the highest quality will take more time. It is important to take into account that carbon-based materials will replace existing standard materials only if they are competitive enough to justify the cost of introduction and integration, so a parallel target is to develop novel applications rather than replace materials in already existing ones [5].

1.2.4. Production techniques

Carbon nanotubes and nanofibers

The most widely studied techniques to produce CNT and CNF powders are arc-discharge [6], laser ablation [55] and chemical vapor deposition [56]. Arc-discharge methods consist on an electrical breakdown of a gas by applying a direct current between two electrodes separated <1 mm; a cathode, usually made of pure graphite, and an anode which usually holds the carbon precursor and a catalyst (usually a metal like iron, cobalt, nickel, etc.) (**Figure 5**a). The electric arc between the electrodes generates a plasma that sublimates the carbon precursor inside the anode, which in contact with the metal catalyst at high temperature results in the production of CNTs (the growth mechanisms of CNTs from metal catalyst will be discussed in next sections). Amounts up to 100 g/h of CNTs in form of powder can be produced with this method [1]. The arc-discharge process is difficult to control because of the very high temperatures needed for graphite sublimation (~3200ºC), and also produces unwanted by-products which contaminates the CNTs. Similar to the arc-discharge method, laser ablation consists on sublimation of a graphite target at about 1200ºC using a laser beam (**Figure 5**b). By using a mixture of graphite and

catalyst, single-wall CNTs are obtained, whereas no catalyst is needed for the production of multi-wall CNTs. The CNTs formed by the laser ablation method are of a higher quality than those produced by the arc discharge method.

Although CNTs and CNFs can be produced in relatively large quantities and high quality by arc-discharge and laser ablation techniques, two important drawbacks are found: the high temperature needed in the production and more importantly, the resulting product is a powder where nanofibres are entangled and randomly mixed, which complicates the purification process and their application. A well-known and promising method to produce high quality CNTs and CNFs at high yields is by catalytic chemical vapor deposition process. This method consists on the thermal decomposition of a hydrocarbon gas over catalytic metal nanoparticles (**Figure 5**c). This method enables a higher control than arc-discharge and laser ablation methods, and a wide variety of aligned structures like macroscopic fibres, vertically aligned CNTs and films can be produced. This represents a significant advantage over other techniques, which is enabled by a highly controlled interaction between the carbon source and the catalyst. CVD is probably the most widely used technique for large scale production of CNTs and graphene films [1], [8], and is the synthesis process used in this PhD thesis.

Table 2 Comparison among the well-established approaches for CNT synthesis [57], [58].

Method	**CNT length (μm)**	**Growth rate (μm/s)**	**Quality**	**Yield**	**Temperature (ºC)**
Arc discharge	~1	up to 10^7	Low	Med	~3200 (local)
Laser ablation	~1	~0,1	Med	High	1000 at furnace surroundings, higher on ablation site)
Thermal CVD	0,1-10^5	0,1-10	High	Med	500-1200
Plasma enhanced CVD	0,1-10	0,01-1	Low	Low-Med	100-800

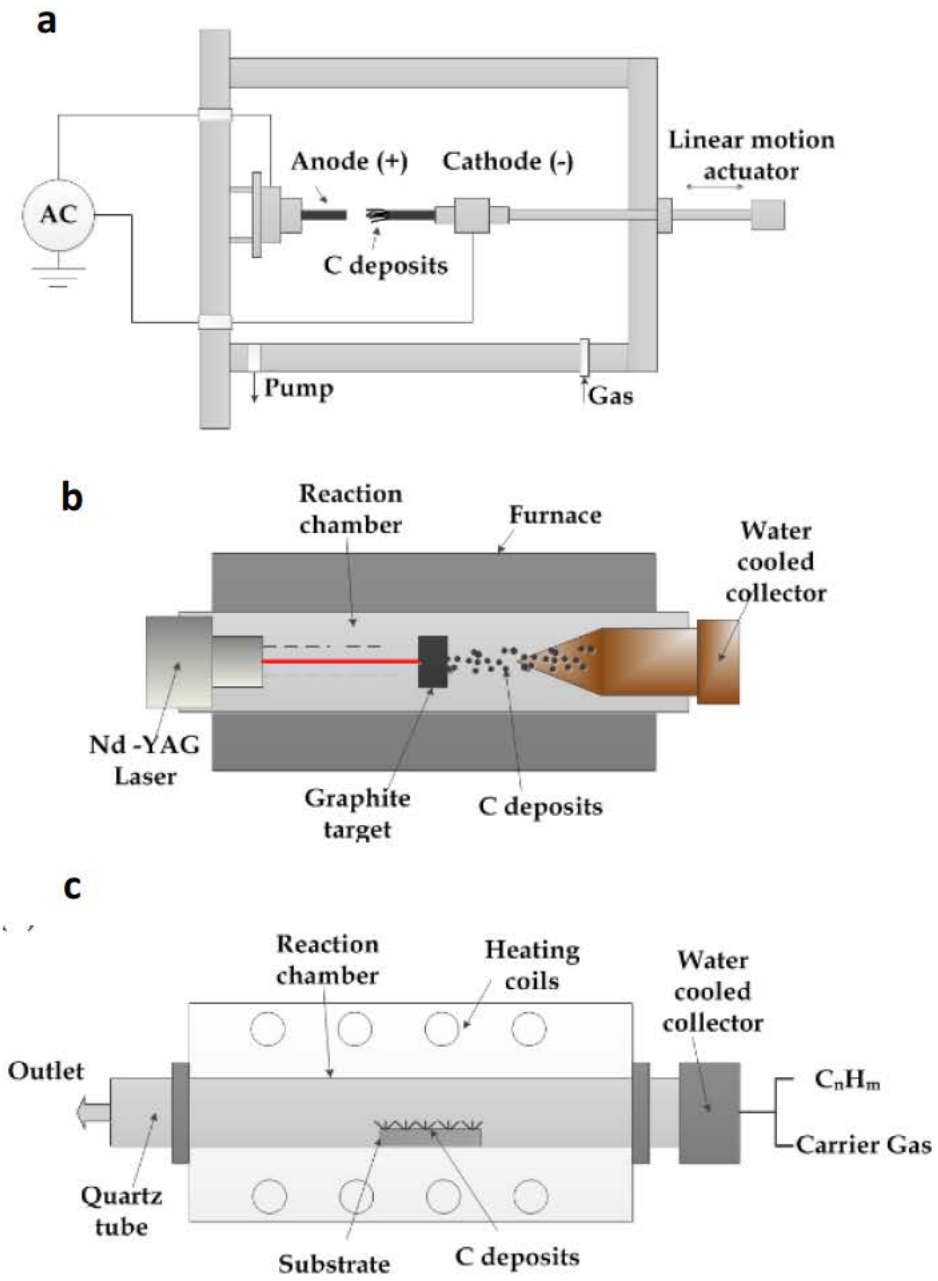

Figure 5 Arc-discharge (a) laser ablation (b) and chemical vapor deposition (c) processes for the mass production of CNTs [59].

Graphene powders and films

Monolayer graphene crystals can be obtained by mechanical cleavage of graphite, which is a dry exfoliation technique consisting on splitting layered materials into atomically thin sheets via mechanical forces (**Figure 6**a). This method yields high quality monolayer graphene with sizes limited by the crystal grains of the starting graphite, up to 1 mm [60]. Although mechanical cleavage is the method of choice for

the preparation of graphene samples for fundamental studies, it is impractical for large-scale applications.

Graphite can also be exfoliated by using liquids (liquid phase exfoliation, LPE), process by which graphene powders can be produced at large scales and low cost (**Figure 6**b). This technique consists on high-shear mixing using rotating blades or ultrasounds [33], [34], and the major problem is that the graphene flakes are highly dispersed with regard to their thickness and lateral dimensions. On the other hand, monolayer and few-layer graphene large sheets up to 1 m (diagonal) can be produced by epitaxial growth on SiC above 1000ºC (**Figure 6**c). This method consists on the sublimation of the near surface Si atoms of SiC. Since SiC is a stablished substrate for power electronics, this is a promising method to produce graphene for nanoeletronics, despite cost issues as compared to Si electronics are still to be fully solved (SiC wafers ~$150-250 vs Si ~$5-10, prices on 2011 [5]). Alternatively, large sheets of monolayer graphene can be produced by chemical vapor deposition using metal foils as catalyst [5], following a similar procedure to obtain CNTs and CNFs. In the next section we provide a further explanation on the chemical vapor deposition process.

Table 3 State of the art (as of August 2014) of the main production approaches of graphene powders, films and foreseen applications [5].

Method	**Crystallites Size, L_a (μm)**	**Sample Size, mm**
Micromechanical cleavage	1000	1
LPE of graphite	0.01-1	0.1-1 (∞ as overlapping flakes)
Growth on SiC	100	100
CVD	50000	1000

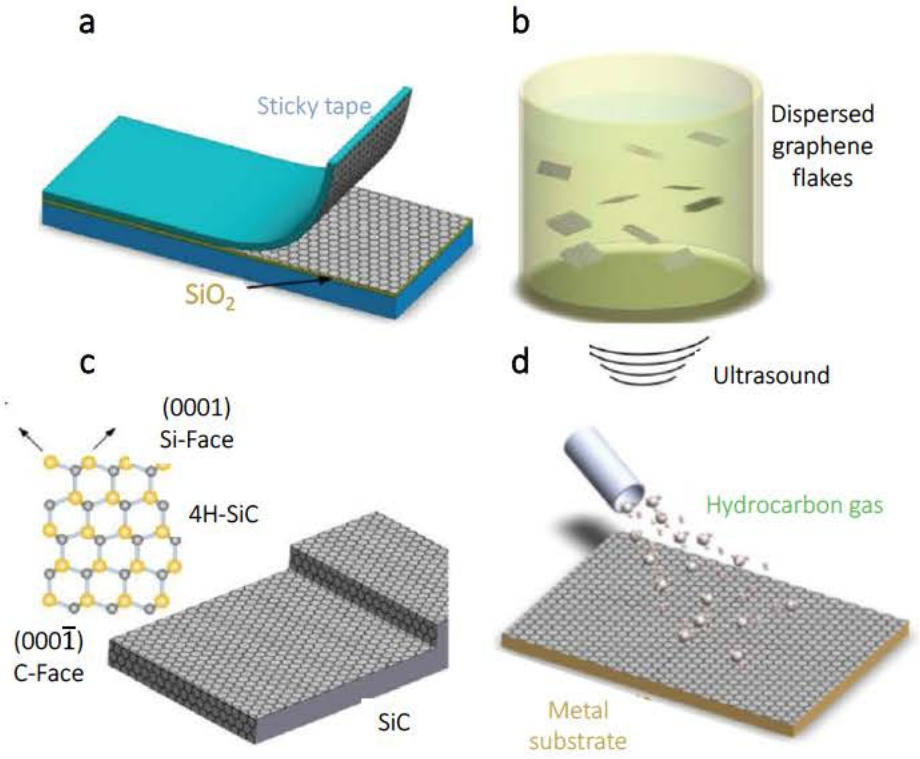

Figure 6 Schematic illustration of the main experimental setups for graphene production. (a) Mechanical cleavage (b) liquid phase exfoliation, (c) growth from SiC (structure of 4H-SiC and the growth of graphene on SiC substrate). Gold and grey spheres represent Si and C atoms, respectively. At elevated temperatures, Si atoms evaporate (arrows), leaving a C-rich surface that forms graphene. (d) CVD process [5].

Amorphous carbons

A wide range of amorphous and semi-crystalline thin films with thicknesses of few nanometres can be obtained depending on the technique. On the one hand, deposition techniques from graphite targets such as ion-assisted carbon deposition, sputtering, cathodic vacuum arc or plasma-assisted deposition mostly result in highly amorphous films with high content of sp^3 bonds, also known as diamond-like carbons [27]. On the other hand, carbon thin films with structural order only at nanoscale, known as glass-like carbons, can be produced either by heat treatments [48] or ion/electron beam irradiation [49] of polymer precursors.

Next, the chemical vapor deposition process using metal catalysts is presented. As it was mentioned in previous sections, CNTs, CNFs and carbon thin films including

monolayer graphene can be produced by this technique, and is considered one of the most versatile and scalable technique to produce carbon nanomaterials.

1.3. Catalytic chemical vapor deposition

Chemical vapor deposition (CVD) is a technique to produce coatings, powders, fibres and monolithic components widely used in the manufacturing of semiconductor and electronics components, coatings for corrosion resistance or machine tools [61]. The deposited material comes from precursors such as metals, carbides, nitrides, oxides and II-VI semiconductor compounds, which are heated by lasers, microwaves or a furnace and deposited on top of a substrate.

CVD of carbon materials normally uses gaseous precursors and furnaces or microwaves as heating sources. A large number of carbon-containing molecules can be used including hydrocarbons, alcohols and aromatic compounds. An inert gas, commonly N_2, helium or argon, is usually introduced to maintain the adequate carbon precursor concentration and rate during the synthesis of carbon nanomaterials. When the CVD process also makes use of metal catalysts to accelerate the decomposition of the precursors, the process is known as catalytic CVD or cCVD. This procedure provides a high control during growth of carbon nanostructures due to the possibility to finely tune the interaction between the carbon source and the catalyst down to atomic scale. In fact, monolayer graphene, CNTs and CNFs can be produced by cCVD by selecting the appropriate metal catalyst, which makes cCVD one most widely used processes to produced carbon nanomaterials.

The metal catalyst can be introduced within the gas phase (floating catalyst CVD) or by previously placing it in the reaction chamber (supported catalyst) and the process normally takes place between 500ºC and 1200ºC. On the other hand, low pressure cCVD permits a more controlled growth mechanism compared to those at atmospheric pressures, however the latter are more scalable. In this section we review the fundamentals of catalytic reactions and the growth mechanism involved in the synthesis of carbon nanomaterials by cCVD, which will serve as a basis for the selection of the catalysts and the discussion of the results presented in next chapters.

1.3.1. The role of metal catalysts

Transition metals have the ability to adsorb and dissociate carbon precursors into carbon atoms [62]. During the cCVD, the transformation of a carbon containing gas molecule into a growing graphitic structure follows a temperature-dependent four-step process (**Figure 7**), as described in references [63], [64]:

(i) **Adsorption** of the gaseous carbon precursor on the catalyst surface. For simplification an acetylene molecule is illustrated, despite it is commonly accepted that the carbon-containing molecule reaches the catalyst surface partially dissociated [62], [65].

(ii) **Dissociation** of the adsorbed precursor into a carbon-intermediate compound (dehydrogenation). This step involves an activation energy barrier E_a, which is overcome in good catalysts.

(iii) **Diffusion** of the dissociated carbon-intermediate compound through or over the catalyst, which involves an energy barrier (ΔE), and also is overcome in good catalysts. This diffusion process may include the dissociation of a surface carbide if it was previously formed. Some carbides are highly stable at CVD conditions, which is translated into a high energy barrier.

(iv) **Nucleation** of a graphitic structure, whose growth rate results as a balance between dissociation rate (ii) and diffusion rate (iii).

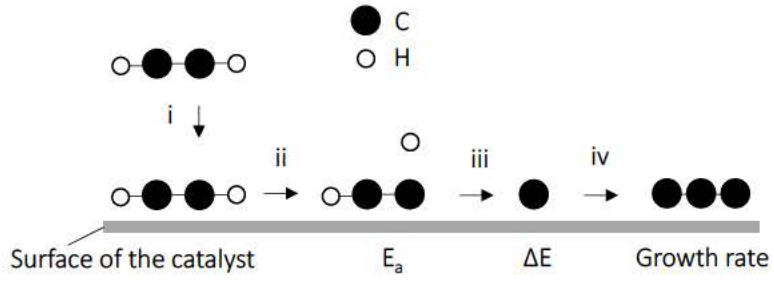

Figure 7 Steps taking place in the catalytic chemical vapor deposition of carbon materials from acetylene (C_2H_2).

Noble metals like copper or gold do not readily dissociate adsorbed precursors (slow step ii in **Figure 7**), meanwhile early transition metals like titanium have too strongly bound carbides which limits the carbon diffusion (slow step iii), as discussed

in reference [64]. In this paper, the authors demonstrated that good catalysts, like iron and nickel, have intermediate carbon solubility and forms metastable carbides. This situation makes binary phase diagrams an interesting tool to evaluate catalytic capabilities of metals. For example, copper shows a very low carbon solubility down to 0.008 weight % at 1084ºC [66] as shown in the phase diagram **Figure 8**a, and does not form any carbide. Due to this low interaction with carbon, copper provides low growth rates which are very adequate for the controlled synthesis of monolayer graphene. Nickel, which is a better catalyst than copper, reveals higher carbon solubilities of 0.02 weight % at 530ºC and 0.6 weight % at 1326ºC, and do not form stable carbides above 500ºC [67]–[70] (**Figure 8**b). Iron shows similar catalytic behaviour as nickel, whose carbon solubility increases with the temperature from 0.02% at 723ºC to 2% at 1147ºC [71], and forms more stable carbides, especially below ~723ºC (**Figure 8**c). Nickel and iron are widely used in the synthesis of CNTs and CNFs. In the next sections we will explain in detail the growth mechanism CNTs and graphene on metal catalysts.

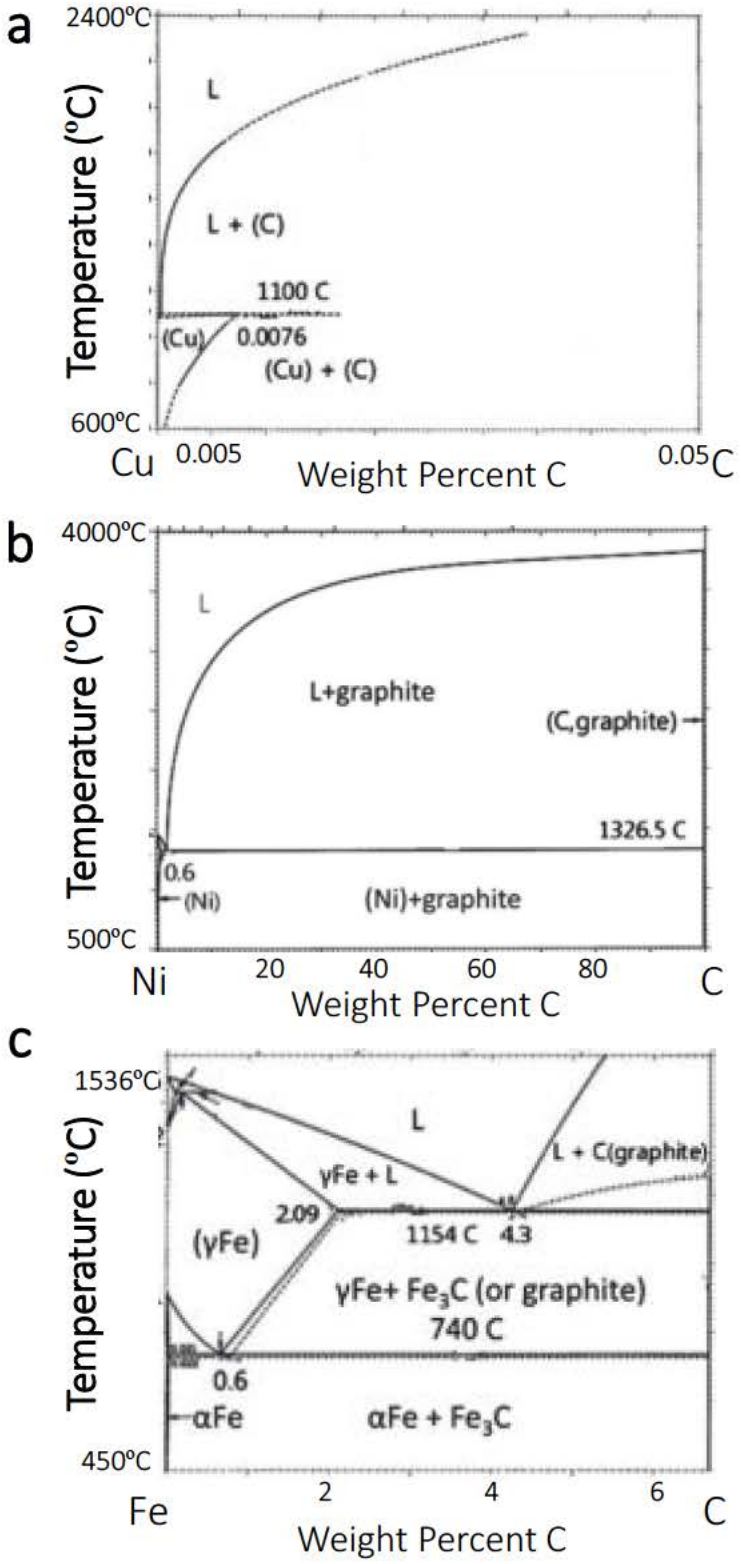

Figure 8 Phase diagram of Cu-C (c), Ni-C (d) and Fe-C (e) [72].

1.3.2. Growth mechanisms of carbon nanotubes and nanofibres

CNTs and CNFs grow from metal nanoparticles in the cCVD process, which act as seeds that extrudes the graphitic planes when the carbon concentration overcomes the solubility limit on the catalyst [62], [64]. These nanoparticles can be continuously introduced in the CVD reactor where they float (organometallics compounds like ferrocene) or can be previously deposited in a substrate (Al_2O_3, SiO_2) [73]. Commonly used catalyst are nickel, iron and cobalt nanoparticles, but a long list of elements have been proven suitable [62].

In the case of floating catalyst, which are normally injected as a liquid solution and brought at ~1200ºC, every point in the surface of the nanoparticles are exposed to hydrocarbon to an exact degree, so a promoter (i.e. sulphur) is added to the gas that helps to promote a directional extrusion of the graphitic planes (**Figure 9**a) [74], [75]. In the absence of sulphur, the majority of the catalyst nanoparticles are encapsulated by carbon layers [75]. Other elements like selenium and tellurium were recently demonstrated to promote the growth of CNTs [76]. If the catalyst nanoparticles are deposited on top of a substrate (**Figure 9**b), its interaction modifies the properties of the nanoparticles during the cCVD process, giving rise to two possible growth mechanisms: i) "tip-growth", at which the CNT precipitates out from the bottom of the metal, pushing the metal particle off the substrate [77], [78], and ii) "base-growth", at which CNT precipitates out from the top of the metal, so the catalyst remains rooted to the substrate. The change from one mechanism to the other is thought to be based on the force of interaction between substrate and catalyst and its size, and nanoparticles are normally identified inside the CNT [79]. CVD of CNTs on highly controlled substrate-supported catalyst results in the collaborative growth of vertically aligned CNT [80].

The solubility and diffusion parameters of carbon in metal nanoparticles are difficult to determine due to their nanometre-size, since the melting point of metal nanoparticles may decrease several hundreds of degrees reaching even the liquid state during cCVD [81]. Because of that, the identification of diffusion mechanisms (bulk and surface diffusion) as well as the chemical state of the catalyst (oxide, metallic or carbide) represent a hard task, and is a highly debated issue. In general,

the activation barriers are lower for surface diffusion than for bulk diffusion [43], [44], and both metallic and carbide phases are found to catalyse the growth of CNTs [82], [83].

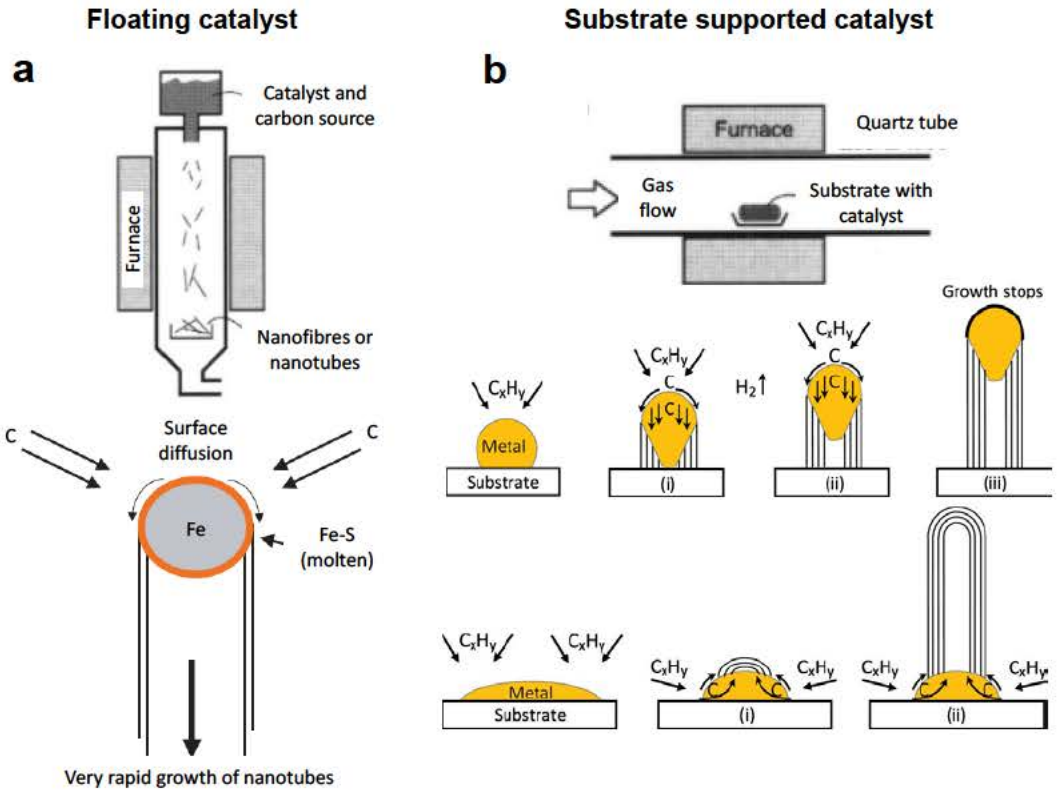

Figure 9 Growth mechanisms of CNT from metal nanoparticles in floating [74] (a) and substrate supported [84] (b) catalysts.

Different types of CNFs are also obtained following these method [16], [85]–[95], and are found to grow from metal nanoparticles with different morphologies. As shown in **Figure 10**, the morphology of the metal nanoparticle at CVD conditions defines the orientation of the graphitic planes within the nanofibre.

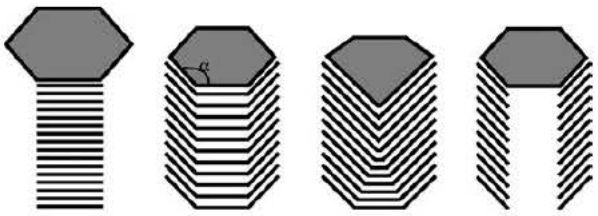

Figure 10 Growth mechanism of carbon nanofibres from polyhedral metal catalysts [86].

1.3.3. Growth mechanisms of graphene and thin films

Graphene films have been synthesized on different metal catalyst like copper, nickel, cobalt, ruthenium, iridium and platinum, either by high vacuum or atmospheric-pressure cCVD [72]. However, nickel and copper have received the most attention due to their low cost, commercial availability and their microstructural stability as they do not tend to form carbides. Despite both nickel and copper are appropriate to synthesize monolayer and continuous graphene films [72], their behaviour under cCVD conditions is fundamentally different due to their different carbon solubilities, as shown in their corresponding binary phase diagram (**Figure 8**c, d).

Graphene formation on copper is mainly produced from the catalytic decomposition of carbon species with a minimal carbon diffusion into the metal, leading to a self-limited surface adsorption process [96], [97], following a classic nucleation and growth mechanism (**Figure 11**a). As a consequence, once the surface is fully covered with a monolayer graphene (and under the appropriate CVD conditions), the growth terminates because the carbon source and the surface of the catalyst are no longer in contact. Due to the very low affinity with carbon, graphene growth mechanism on copper surfaces is highly controllable, and because of that copper is considered as the catalyst of choice for the synthesis of monolayer graphene at large scales.

The higher carbon solubility in the nickel lattice in comparison to copper at the synthesis temperatures (about one order of magnitude), has important implications in the growth of graphene in this metal. Carbon diffuses during the CVD synthesis step into the nickel lattice, which acts as a carbon reservoir, and segregates and precipitates in the surface during the CVD cool down step (**Figure 11**b), when the solubility of carbon decreases [98]. The carbon precipitation process can be diminished by using a controlled and thin nickel film (the lower the nickel the lower the carbon) and/or by using high cooling rates in order to obtain just a single monolayer graphene film [98]–[100]. Although these methods help to control the final thickness of the carbon film, carbon preferentially precipitates out at the grain boundaries of the nickel catalyst during the CVD cool down, resulting in non-homogeneous thickness carbon films.

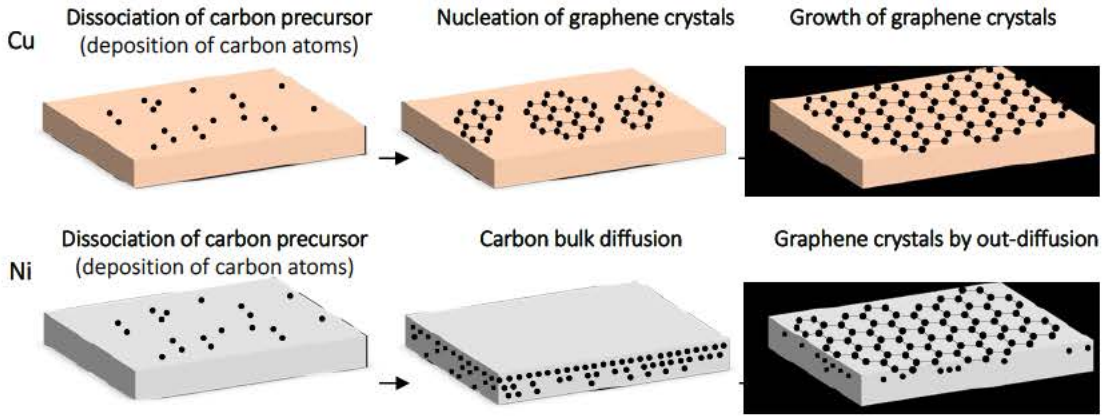

Figure 11 Growth mechanism of graphene on copper and nickel, highlighting the different mechanism between copper (with low carbon solubility) and nickel (high carbon solubility).

One of the most important parameter to control during the synthesis of graphene films is the oxygen content during the CVD process. Oxygen greatly affects the growth mechanisms of graphene [101], and the synthesis temperature can be reduced down to 300°C in an oxygen-free CVD system [102].

Two main sources of oxygen can be present in a CVD system. The native oxide layer in the metal foils, which can be partially removed by dipping the catalysts in diluted acids [103] and with a pre-annealing step under a hydrogen reducing atmosphere. The latter method also diminishes the metal grain boundaries (and their related defects) by increasing the grain size and rearranges the metal surface morphology reducing structural defects and atomic steps [104], [105]. Oxygen can also be present in the CVD atmosphere, which can be reduced by using low-pressure CVD and ultra-pure gases. Depending upon the final application, different qualities of graphene may be demanded, and as a consequence different CVD equipment may be used.

1.4. Scalable production of ordered carbon nanostructures by cCVD

The industrial use of carbon nanomaterials requires large scale and cost effective production methods that provide a balance between the fabrication route and final material quality. Since 2006, the production of CNT powders has increased at least 10-fold reaching 4.5 kTon in 2011 [4], boosted by an increasing number of companies offering CNT powders (list provided in references [4], [106]), and a similar scenario

is found in the production of graphene powders [107]. A shorter list of producers of ordered carbon structures is found, such as aligned CNT (NanoLab, Inc, N12 Technologies, US Research Nanomaterials, Inc.), CNT fibres (Nanocomp Technologies, Inc.), or graphene films (Graphenea, ACS Materials LLC), to cite some examples. The interest of highly ordered carbon structures lies on a better performance as demonstrated in composite reinforcement using aligned CNTs [108] or highly conducting transparent electrodes made out of continuous monolayer graphene [42].

As it was previously mentioned, cCVD offers a highly controllable reaction which can be tuned to produce such ordered structures at large scales. In this section we review some catalyst preparation techniques and some scalable cCVD approaches existing in the literature to produce ordered carbon nanostructures like films, fibres and arrays. Finally we propose the alternative and direct approach of using commercially available metal catalysts with different morphologies and compositions to obtain ordered structures and reduce the cCVD costs.

1.4.1. Catalyst preparation

Metal nanoparticles

Several methods have been applied to produce catalyst nanoparticles for the synthesis of CNTs and CNFs by cCVD. Floating catalyst methods use volatile metal-organic compounds such as ferrocene that generate a CNT aerogel inside the CVD reactor [75]. Supported catalyst is mostly prepared by precipitation of metal salts (nitrates, sulphates and chlorides) on top of a support followed by drying, calcining and grinding [81]. This process generally leads to a wide particle size distribution, resulting in heterogeneous products after synthesis. A more controlled process consists on the use of microfabrication techniques like e-beam or sputtering to deposit a few-nm-thick film of catalyst on top of insulating substrates like Al_2O_3/SiO_2 [73]. Under proper conditions, this catalyst film evolves at CVD conditions to produce the needed nanoparticles that support the growth of CNTs [109]. CNTs arrays of several millimetres tall can be synthesized using e-beam or sputtering catalyst preparation methods [110].

Metal films and foils

Nickel and copper catalyst films needed for the synthesis of graphene films can also be prepared by microfabrication techniques like e-beam or sputtering [111], [112], obtaining a thin film from few to hundreds of nm over a SiO_2 wafers. Caution have to be taken in order to prevent the de-wetting and coalescence of the catalyst into nanoparticles at CVD temperatures. Contrary, a more straightforward and low cost method is the use of commercially available pure metals foils with different qualities and thicknesses (25-100 μm thickness and purities of 99.8-99.999%). A great number of studies demonstrated the feasibility and scalability of commercially available foils as catalyst for the synthesis of monolayer graphene films [72] or reticulated nickel foams for the synthesis of 3D free-standing graphene foams [113]. Surface imperfections on commercial catalysts like atomic step edges, defects roughness and impurities play a role as active sites for graphene nucleation and have to be controlled in order to obtain repetitive samples.

1.4.2. Continuous catalyst feeding

CNTs fibres and arrays on floating and supported catalyst

The cCVD process using a floating catalyst is currently exploited to produce a continuous CNT fibre by direct spinning [74], [75], [80], [114]. Due to the high speed of CNT growth rate (up to 1 mm/s) at the high temperature used in this process (~1250ºC), it is possible to synthesize CNT fibres at rates of 10-70 m/min [75], [115]. Illustration of the use of floating catalyst for the synthesis of CNT fibre by direct spinning can be found in **Figure 12**a,b,c. Similar CNT fibres can be spun from vertically aligned CNT arrays, whose CNT length are more controllable in comparison to the previous floating catalyst technique [80].

The continuous synthesis of CNT arrays was demonstrated in a moving substrate ($Fe/Al_2O_3/Si$) using a cold wall chemical vapor deposition reactor and multiwall CNT arrays with heights of ~1 mm were achieved at substrate speeds of 2.4 mm/s [116], [117]. Despite the synthesis of CNT arrays using e-beam/sputtering techniques demonstrates very good results in terms of control and yield, it suffers of obvious problems for its scalability, in particular due to their vacuum requirements. Thus, alternative catalyst preparation was developed consisting on the continuous-feed

evaporative self-assembly process (blade-casting) of iron oxide nanoparticles [118]. This versatile method enables control of the density of CNT arrays by solution concentration and substrate velocity (up to 0.4 mm/s), and is scalable and cost effective compared to vacuum deposition methods. Illustration of the use of supported catalyst for the synthesis of CNT arrays by direct spinning can be found in **Figure 12**d,e,f.

Graphene continuous synthesis and roll-to-roll polymer transfer

In 2011, it was demonstrated the continuous cCVD process of multi-layer graphene on copper foils, with catalyst feeding rates of 1–40 cm/min [119] and one year later by plasma-enhanced cCVD process at 30 cm/min which resulted in a low quality graphene [120]. More recently, interesting new designs using concentric tubes were proposed [121]. An important bottleneck in the large scale application of graphene films is its transfer from the CVD catalyst to the final device. First transfer processes demonstrated in 2010 consisted on depositing a protecting polymer film (PMMA) and dissolving the copper catalyst by chemical etching [43]. In 2013 the whole continuous synthesis, polymer application and etching-transfer at 10 cm/min was demonstrated [122]. Alternatively to etching treatment, which destroys the copper catalyst, other non-destructive transfer methods like the electrochemical delamination of graphene/copper interface are being developed and demonstrated to have a similar rate as the CVD synthesis [123], reaching values up to 2 cm/s. Illustration of the use of copper foils for the continuous synthesis of graphene films and the final graphene/polymer composite can be found in **Figure 12**g,h,i.

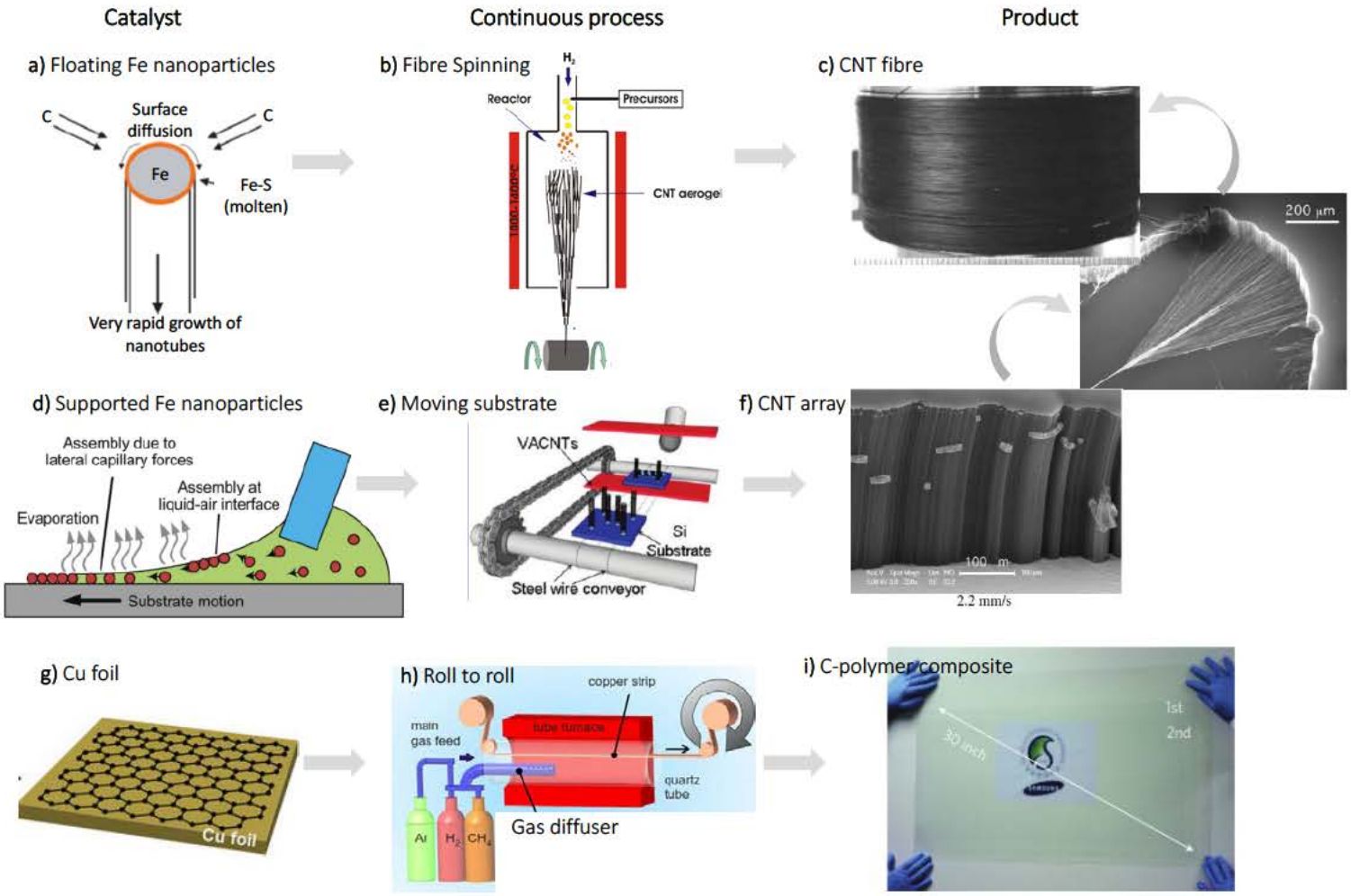

Figure 12 Scalable schematics for the catalytic CVD for the production of various carbon nanomaterials: CNT fibre on iron floating catalyst [74], [115], [124] (a, b, c) and CNT arrays from iron supported nanoparticles [116]–[118] (d, e, f) and carbon films on copper foils [43], [102], [119] (g, h, i).

1.4.3. Current study of powders and foils catalysts

As it was explained, active metal catalyst in the synthesis of CNTs and CNFs by cCVD are normally particles at the nanoscale (below 100 nm), and different CNTs and CNFs might grow depending on their size [125], the catalysts nature, the hydrocarbon source and the temperature of synthesis [16]. It was also explained that there exists two major cCVD scalable processes for the synthesis of ordered carbon structures, i) the floating catalyst method using metal-organic compounds, and ii) the substrate method by depositing a catalyst thin film by microfabrication techniques. Alternatively, ordered CNTs and CNFs can be produced at large scales by using commercial metal powders [126], [127] foils and meshes [128]–[142] as catalyst. This straightforward approach, which is already demonstrated in the synthesis of graphene on commercial bulk copper foils, reduces or eliminates the catalyst preparation processes and yields ordered CNFs and CNTs.

Metal powders catalysts. Nickel and iron powders produced in the laboratory by precipitation techniques are demonstrated to catalyse the growth of a wide variety of carbon nanofibres, like fishbone CNF with small diameter (25 nm - 500 nm) [143], octopus-like structures with 4 arms of about 400 nm in diameter [144] or helical and straight stacked-like carbon nanofibers [145], [146]. Similar results have also been demonstrated when using iron-nickel alloys [16], [147], [148]. The direct synthesis of carbon nanofibers on the surface of commercially available copper powders with a controlled size (5-10 μm in diameter) was also studied [149], despite yielding a low quantity of carbon nanofibres.

Metal foils catalysts. Stainless steel foils have also been used as catalytic substrate for the direct synthesis of CNT [128], [130], [131], [133], [138], [139]. Besides its low cost and commercial availability, its chemical composition (rich in iron and nickel) permits the direct growth of CNTs without any pretreatment [138]. Some pretreatments improve the length and yielding of CNTs in these metallic substrates, and a higher density of vertically aligned CNT arrays was obtained by chemical etching of the stainless steel foil [130]–[133]. The etching treatment removes the Cr_2O_3 passive protection layer that is always present in stainless steels and which produces an increment of iron oxide on the steel surface [133]. Oxidation–reduction pretreatments also produces iron catalytic nanoparticles on the stainless steel

surface [131]. Mechanical treatments such as polishing [135] and argon ion bombardment [134] were also reported as effective stainless steel pretreatment methods. Interestingly, both stainless steel [150] and pure iron foils [151] were recently used as catalysts for the synthesis of polycrystalline graphene structures, which demonstrates the versatility and potential of iron-based foils.

Behaviour of bulk metals at cCVD conditions. Despite the possibility of synthesizing CNFs and CNTs on bulk metals is already known, the control of the growing nanostructure, its quality and homogeneity represents a challenge since the starting catalyst greatly evolves under the cCVD conditions due to its micrometre size, leading to the formation of new phases [62], precipitation of carbon [152] or migration of species [138]. Interestingly, bulk metals can break up by the effect of deposited carbon following a process known as metal dusting, well-known in the steam reforming industry. Metal dusting is a corrosion mechanism taking place on metals under carburizing atmospheres between 400°C to 900°C, which results in its fragmentation into small nanoparticles, carbides and carbon filaments [153]–[155]. In close relation to the role of metal catalysts during cCVD described in the section 1.3.1, two main mechanisms of metal dusting have been proposed (**Figure 13**); a first one involving the direct carbon deposition on the metal (nickel-based alloys), the second involves the formation of carbides (as in the case of iron) [153]–[163], which normally leads to the fragmentation of the catalyst surface (**Figure 13**b). The study of the metal behaviour and its influence in growth mechanism of carbon structures is the main objective of this work.

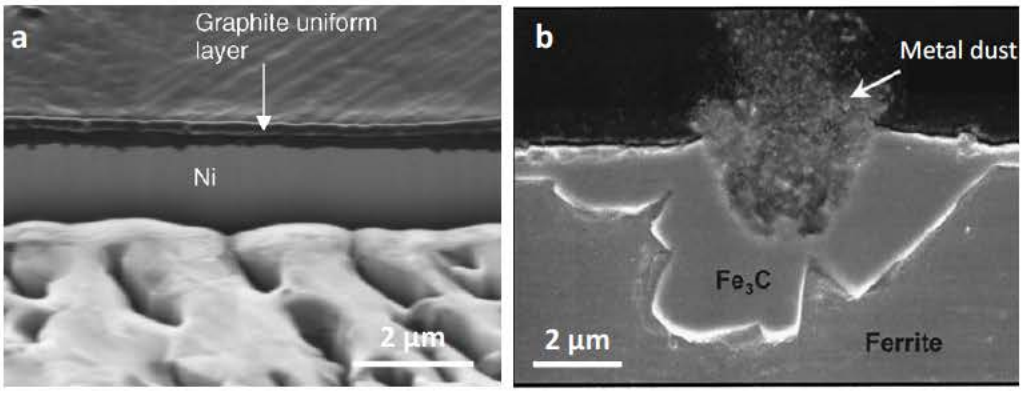

Figure 13 Carbon deposition on nickel [162] (a) and iron (ferrite) [164] (b), the first involving the direct deposition and the second the generation of iron-carbide intermediate, which is decomposed into dust, giving name to metal dusting phenomena.

2
Motivation and thesis outline

2.1. Motivation and objectives

Carbon is a very versatile element, and is able to form a variety of crystalline and amorphous materials which are currently in an extensive use in engineering. The recent in-depth characterization of graphene [20] has renewed the interest in carbon nanomaterials and related nanostructures which are proposed for a wide variety of applications such as electronics, energy production/storage, biomedical, among others. However, main issues in maintaining carbon nanomaterial properties and performance upon mass production and integration are still to be solved before they can display their expected industrial relevance.

Nanocarbons with different morphologies and crystallinities can be produced by catalytic chemical vapor deposition (CVD). It consists on the thermal decomposition of hydrocarbons (carbon source) over metal catalysts, and offers high controllability, scalability and adaptability to fabricate on-demand carbon nanomaterials like films, fibres, arrays and other highly organized structures.

In this thesis, it is proposed the use of a custom-made CVD reactor and commercial bulk metals like powders and foils as catalysts for the production of carbon nanomaterials. Such a straightforward approach reduces/eliminates the catalyst preparation processes that in some cases requires expensive and hard-to-scale microfabrication techniques.

This thesis aims at the following objectives:

i. Understand the behaviour and mechanism of interaction of commercially available bulk metals (such as metal powders and foils) in a CVD reactor during the production of carbon nanomaterials.

ii. Study the effect of catalyst composition, the temperature of synthesis and the effect of gas flow (rate and composition) on the growing carbon nanomaterial during CVD.

iii. Produce final materials, in form of powders and thin films, by using highly-scalable CVD processes, with special focus on carbon-based thin films.

iv. Characterize some physical properties of carbon-based thin films, compared them to already existing competitors, and evaluate the applicability of low crystalline or amorphous carbon materials.

2.2. Thesis outline

This thesis is organized in the next chapters.

Chapter III: Experimental techniques

A summary and brief description of the experimental techniques used during this thesis is presented in Chapter III. A custom-made CVD reactor is explained as well as the synthesis procedure. The chemical composition and microstructure of carbons and catalyst materials were characterized with electron microscopy and spectroscopy techniques. Surface roughness or carbon films were measure by atomic force microscopy.

Chapter IV: Synthesis of carbon nanostructures on nickel and Invar powders

Pure nickel and Invar ($Fe_{64}Ni_{36}$) powders are the first catalysts used for the direct synthesis of carbon nanomaterials using several CVD synthesis conditions (from 530ºC to 830ºC and from 1 to 1400 minutes). We have obtained a multidirectional growth mechanism of carbon fibres at low temperatures leading to ultrahigh yield of 400 over the catalyst mass. Synthesis at high temperatures produced the fragmentation of the nickel powders (the so-called metal dusting process), producing metal-graphite core-shell nanoparticles. A similar fragmentation process is detected

when using Invar powders as catalyst regardless of the synthesis temperature. We studied and took advantage of the fragmentation behaviour of the Invar powder under CVD conditions for the *in-situ* production of catalytic nanoparticles, which enabled the growth of a wide variety of carbon nanomaterials, like nanofibres and carbon-metal core-shell nanoparticles.

Chapter V: Synthesis of CNT arrays and carbon thin films on stainless steel foils

This chapter presents the simultaneous growth of vertically aligned carbon nanotubes and amorphous carbon thin films directly on stainless steel foils. A simple air oxidation treatment followed by CVD was used to synthesize the carbon nanostructures. A detailed study of the effect of the CVD synthesis conditions in the stainless steel was performed, identifying key processes taking place in the stainless steel during the nanostructure formation. Two important aspects highlight the use of low-cost stainless steel foils, which are the absence of a catalyst preparation for the growth of the CNT arrays and the simultaneous and physically connected growth of the CNT arrays to a carbon thin film.

Chapter VI: Synthesis of carbon thin films on copper foils

This chapter presents the controlled synthesis of nanocrystalline glass-like carbon thin films (area *ca.* 10cm^2) directly on copper foils by CVD. We follow a similar process to that used in the production of graphene films, but using a wide range of gas concentrations to enable easy film-thickness control from 5 to 300 nm. We obtained transparent and conductive glass-like carbon thin films formed by randomly oriented and curved graphitic nanocrystallites within an amorphous carbon matrix, which might be an alternative to graphene films in application not requiring the highest crystallinity.

Chapter VII: Glass-like carbon thin films: Physical characterization and polymer-assisted transfer by thermal shocks

Among all the carbon nanomaterials produced during this thesis, the carbon thin films presented in the Chapter VI have been selected for their characterization. Two applications have been selected, which are i) as transparent and flexible electrodes for which optical and electrical characterization was carried out, as well as the

comparison with other carbon-based flexible electrodes, and ii) biocompatible applications, thus surface wettability was measured. Finally, a highly scalable and ultrafast-transfer process of glass-like carbon thin films to polymer films is presented.

Chapter VIII: Conclusions and future work

This final Chapter summarizes all the results and conclusions extracted along this PhD Thesis and propose further research work on synthesis of carbon nanomaterials on bulk metal catalysts and applications of related materials.

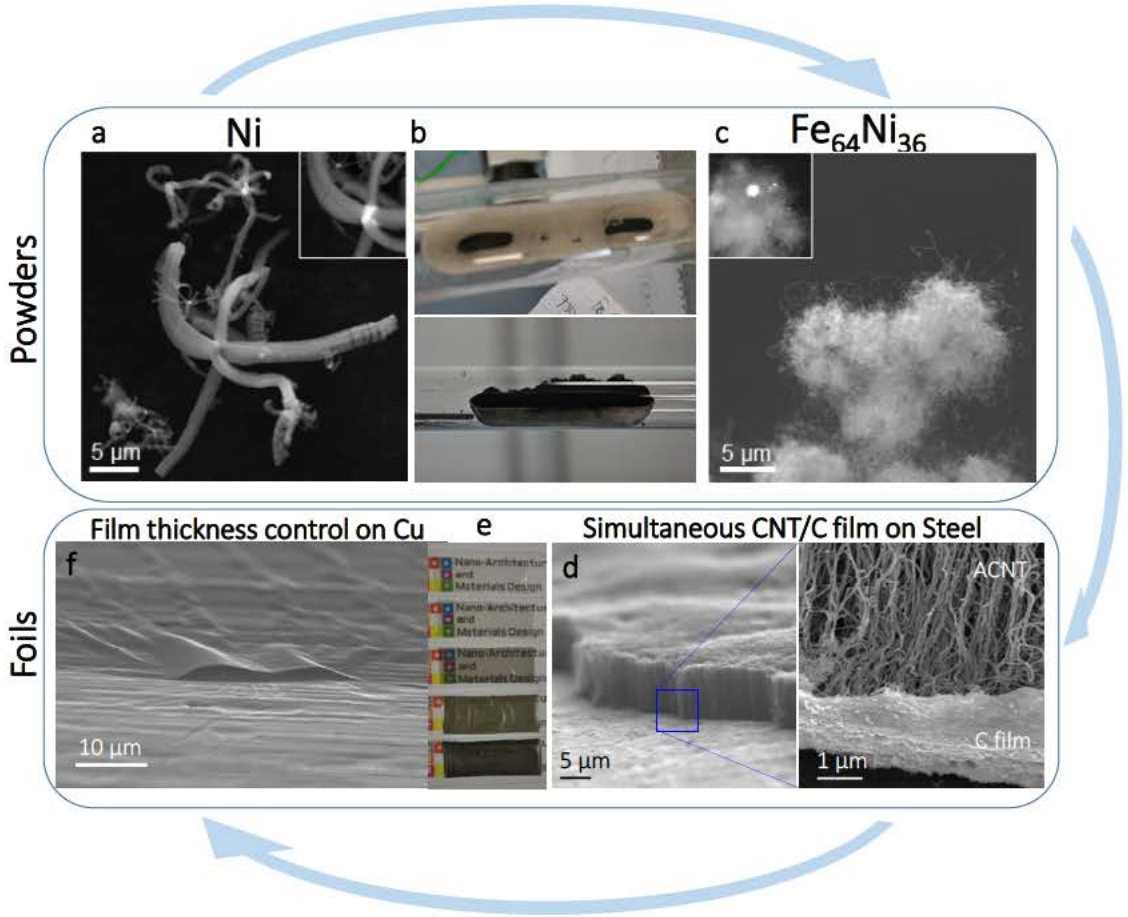

Figure 14 Thesis outline showing the main products obtained from each catalyst. Chapter IV (a, b, c) presents the performance of nickel and Invar ($Fe_{64}Ni_{36}$) powders for the synthesis of carbon fibres and nanofibers. SEM images of nickel (a) and Invar (c) and the mass production after CVD (b). Chapter V (d) presents the use of stainless steel foil for the synthesis of vertically aligned CNT, which grew attached to a carbon thin film. Chapter V (e, f) presents the use of copper foils for the synthesis of carbon thin films (f) and the preparation of polymer composites (e).

3
Experimental techniques

The methodology followed to synthesize carbon nanomaterials and the characterization techniques used in this work is specified in this chapter.

3.1. Synthesis of carbon nanomaterials by catalytic chemical vapor deposition

A custom-made CVD reactor was built to carry out all the synthesis processes (Nabertherm R50/250/12 furnace). This system consisted of a furnace mounted on a mobile platform which allowed us to perform fast heating and cooling ramps [165]. As detailed in the **Figure 15**, position (a) corresponds to warm-up and cool down and position (b) to catalyst annealing and synthesis of carbon nanomaterial.

The process starts by positioning the metal catalysts in the middle of a cleaned quartz tube (22-mm diameter), which corresponds to the centre of the horizontal tube furnace during the synthesis step.

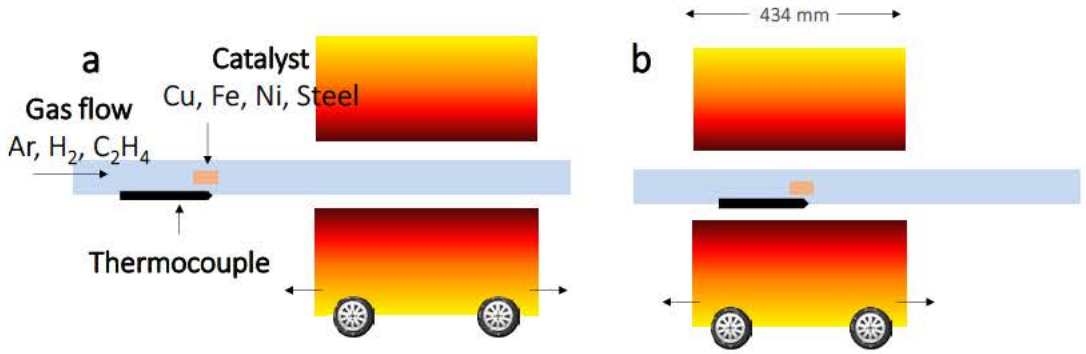

Figure 15 The custom-made chemical vapor deposition reactor.

The quartz tube is previously cleaned by opening and heating the furnace up to 800°C during 1 hour at position b, so all deposits in the synthesis area are burned by oxidation. Then, the furnace is taken to the desired synthesis temperature and stabilized for 1 hour approximately.

The CVD normally involves 4 steps (**Figure 16**):

i) **Flushing**: all the lines connected to the system are flushed for 10 minutes (Ar=H_2=C_2H_4=300 sccm) followed by 10 additional minutes of Ar to displace trapped air from the system (Ar=1000 sccm).

ii) **Annealing**: the furnace is rapidly moved (*ca.* 3 s) until the catalyst is located in the middle of the heating zone. The catalyst suffers a fast annealing from room temperature to synthesis temperature with a first heating rate of about 500°C/min, which is enabled by the possibility to move the warm reactor. This process takes between 5 and 20 minutes, with different gas mixtures which are summarized in Table 4.

iii) **Synthesis**: Ethylene (C_2H_4) is added to the previous gas flowing in different concentrations depending on the carbon nanomaterial to be synthesized. We carried out synthesis experiments from 1 to 1400 minutes.

iv) **Cool down**: The furnace is moved back to cool down the carbon product under a 1000 sccm Ar flowing, taking about 20-30 minutes. Finally the carbon material can be extracted.

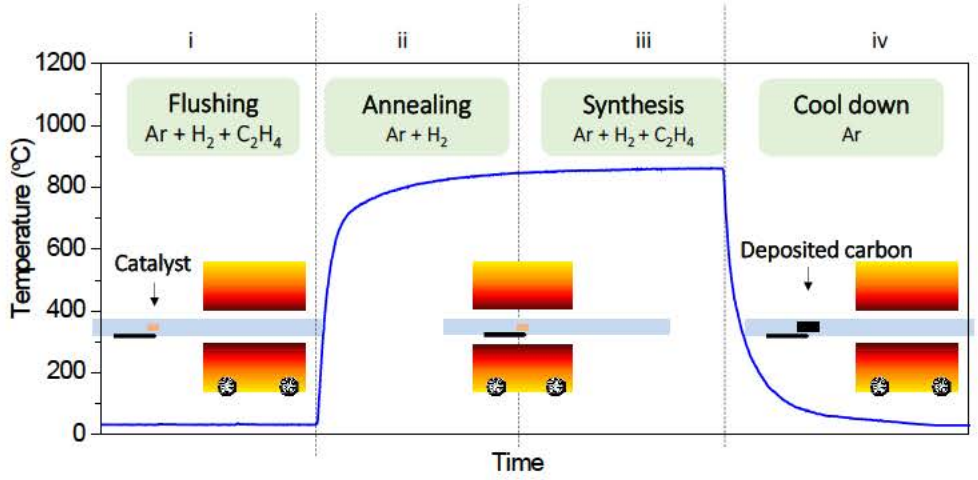

Figure 16 Steps taking place in during our CVD synthesis process.

Several CVD experiments were explored using different catalyst compositions and morphology at different synthesis times and temperatures. A first set of experiments was designed to study the effect of alloying in nickel and iron-nickel powders as catalyst for the direct synthesis of carbon nanofibers (Alpha Aesar 99.8% and Invar

$Fe_{64}Ni_{36}$ Sandvik Osprey powders). The results of these experiments are presented in Chapter IV.

A second set of experiments consisted on the use of stainless steel foils (304 grade, 25 μm thick, Metall-Folien GmbH) for the synthesis of vertically aligned CNTs. The results of CVD using stainless steel as catalyst are presented in Chapter V.

A third set of experiments was designed for the synthesis of graphene and carbon thin films using copper foils as catalyst. For the synthesis of carbon thin films we used a 100-μm-thick copper foil, 99.8% purity (Sigma Aldrich). For the synthesis of graphene we used 100-μm-thick copper foil, 99.999% purity (Puratronic Alfa Aesar). The results of CVD using copper foils as catalyst are presented in Chapter VI.

Table 4 CVD conditions carried out during this thesis depending on the catalyst used.

Catalyst composition	**Catalyst morphology**	**Objective**	**Synthesis conditions**
Ni $Fe_{64}Ni_{36}$	Powders	Metal dusting analysis Synthesis of fibres and nanostructures	**Temperatures** 530-830ºC **Annealing step** Ar/H_2 = 100/400 sccm 5 min. **Synthesis step** $Ar/H_2/C_2H_4$ = 100/400/100 sccm 5-1440 min.
Stainless steel	Foils (Oxidized at 500ºC, 30 min)	Metal dusting analysis Synthesis of aligned CNT	**Temperatures** 700-830ºC **Annealing step** Ar/H_2 = 100/400 sccm 5 min. **Synthesis step** $Ar/H_2/C_2H_4$ = 100/400/100 sccm 5-20 min.
Cu	Foils	Synthesis of graphene and graphene-like films	**Temperatures** 550-950ºC **Annealing step** Ar/H_2 = 1000/20-200-400 sccm 5-10 min. **Synthesis step** $Ar/H_2/C_2H_4$ = 0-1000/20-270/0.5-270 sccm 5-10 min.

3.2. Characterization of carbon deposits by Raman spectroscopy

Raman spectroscopy has been used to carry out a comparative study of the crystallinity of the carbon deposits. Raman spectroscopy is a fast and non-destructive technique to characterize materials and is widely used both in the laboratory and industry. It is based on Raman scattering, which is the inelastic scattering of photons by a vibrating crystal lattice [166]. Incident photons of energy defined by the Planck-Einstein relation $E=h\omega_L$ (h is the Planck constant and ω_L is the photon frequency) creates an excited and unstable electronic state of energy $E_{GS}+h\omega_L$ in the material (E_{GS} is the ground state energy), which leaves the unstable situation by emitting back a new photon of energy $h\omega_{SC}$ (**Figure 18**). If this excited state coincides with a stationary state, the process is called resonant and takes place when incoming photon have energy enough to generate an electronic transition.

If the energy of the emitted photon remains the same as the incident one, it is called elastic or Rayleigh scattering. With a much lower probability, the incoming photon can lose or gain energy in the interaction process if the system relax back to a higher or lower energy state, either by creating (Stokes) or annihilating (anti-Stokes) a phonon of energy $h\Omega$. Thus, the energy of the emitted photon is $h\omega_{Sc} = h\omega_L \pm h\Omega$.

The identification of the structure of materials by Raman spectroscopy is based on their well-known phonons or vibration modes. Raman spectra is constructed by plotting the intensity of the scattered light as a function of the difference between incident and scattered photon energy, known as "Raman Shift" and plotted in cm^{-1}. Typical Raman experiments are conducted using incident lasers of 1064−229 nm range, which only excite the surface of the material and give rise to several bands. Depending upon the sample lattice, some bands would appear and some others would be prohibited (due to the impossibility of certain vibration modes to happen). The most important Raman bands of graphite and graphene are those corresponding to in-plane vibrations, which are D, G and 2D bands (**Figure 18**).

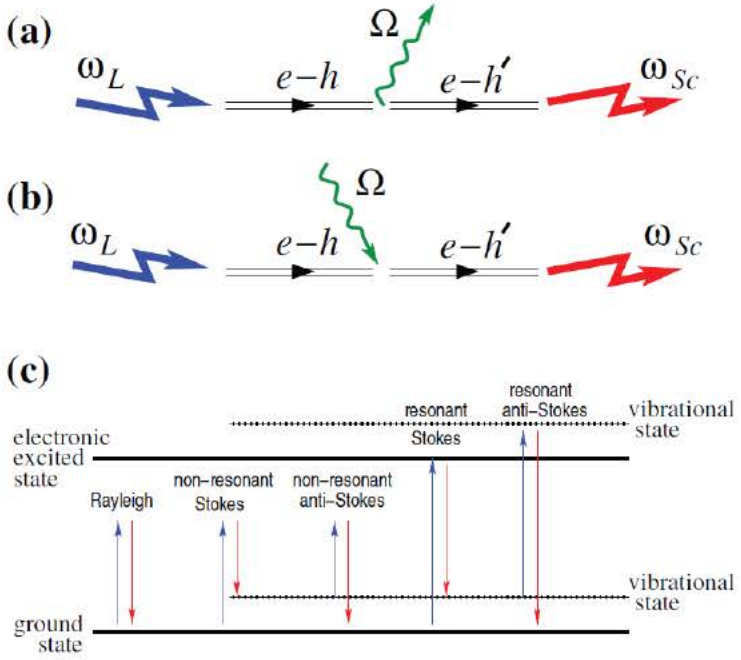

Figure 17 Raman scattering. An incoming photon ω_L excites an electron-hole pair e-h, which in a Stokes process (a) decays into a phonon Ω and another electron-hole pair e-h´, which recombines emitting a photon ω_{Sc}. In an anti-Stokes process (b), the phonon is absorbed by the e-h pair. c) Rayleigh/Raman scattering in resonant and non-resonant conditions [166].

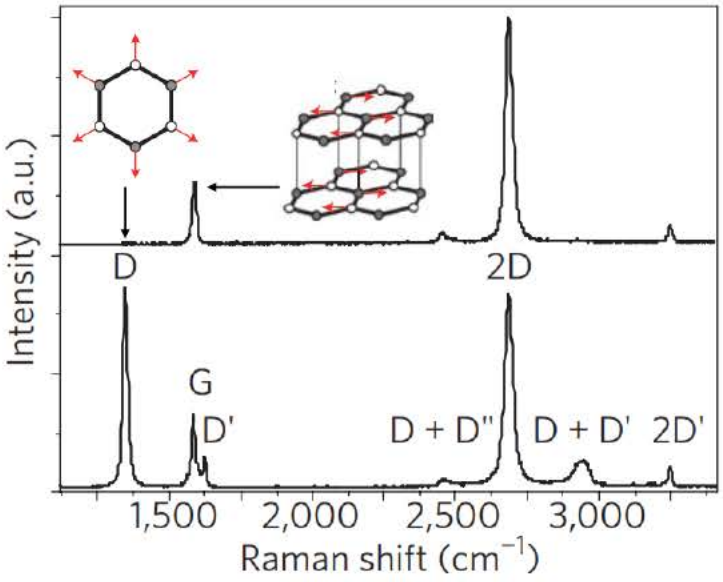

Figure 18 Raman spectra of two graphene samples, showing the effect of defects the activation of D, D´ band and their combinations (D+D´´, D, D´) and overtones (2D´) [166].

G band (~1580 cm^{-1}) is assigned to bond stretching of sp^2 pairs in both rings and chains, so it is always present in sp^2-bonded carbon materials. Contrary, D band (~1350 cm^{-1}) is only present when defects are present in the crystal lattice, and is

assigned to the breathing mode of carbon rings, which is a prohibited vibration mode on a perfect graphite lattice. Finally, D overtones generate the 2D band (~2700 cm^{-1}), but it does not need defects in the carbon material to be activated. Although being an in-plane mode, the 2D peak is sensitive to the number of graphene layers in graphite. When defect density in the carbon material increases, other defect-related bands appear like D´ (~1620 cm^{-1}) and D´´ (~1180 cm^{-1}). D, D´ and D´´ can also combine to produce D+D´´ and D+D´ bands, and D´ has its own overtone 2D´ at about (~3250 cm^{-1}) [166].

3.3. Characterization of metal catalysts by X-Ray diffraction

We have used X-ray diffraction to study the composition and microstructure of metal catalysts before and after the CVD process. This analysis provided us with useful information to understand the metal behaviour under CVD conditions. X-ray diffraction is a non-destructive technique based on the interaction of high energy photons (X-rays with wavelength **λ** comparable to the size of atoms) with the crystallographic planes of the solid. This interaction is the diffraction of the incoming X-ray beam with the crystallographic planes separated a distance **d** when the next condition is satisfied (Bragg´s law):

$$n\,\lambda = 2\,d\,\sin\theta \qquad (2.1)$$

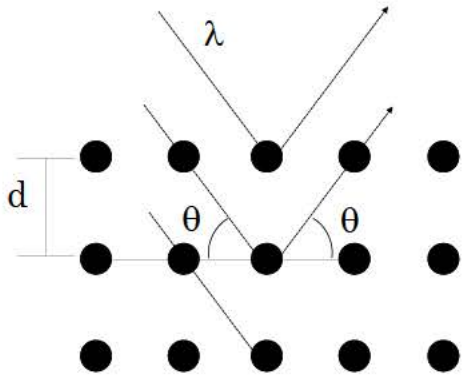

Figure 19 Conditions of diffraction relating the X-ray wavelength (λ), the incidence angle (θ) and the interatomic distance of the crystal (d).

The high energy of X-rays enable a deep penetration in the materials providing information of their bulk. Despite θ is the angle between the incident beam and the

plane that generates the diffraction, XRD results are normally plotted as a function of 2θ, which is the angle between the incident and diffracted beam.

3.4. Characterization of metal catalysts by X-Ray photoelectron spectroscopy

We have used X-ray photoelectron spectroscopy to study the composition and chemical state of the surface of stainless steel before and after the CVD process. X-ray photoelectron spectroscopy (XPS) involves the irradiation of the solid in vacuum with a monoenergetic X-ray beam of energy hω, which is "absorbed" by the electrons of the sample that are bound to the nucleus with a binding energy E_b. If the X-rays have enough energy (**Figure 20**a), those electrons may leave the atom with a kinetic energy E_c (equation 2.2). This process is known as photoelectric effect.

$$E_c = h\omega - E_b - \phi \qquad (2.2)$$

Being ϕ a work function dependent on both the spectrometer and the material. Each material has a unique elemental spectrum of E_b, and the spectral peaks from a mixture are approximately the sum of the elemental peaks from the individual constituents. Since the mean free path of the electrons is very small, the electrons which are detected originate from only the top few atomic layers. Quantitative data can be obtained from the peak heights or areas and identification of chemical states often can be made from the exact positions and separations of the peaks. XPS experiments were carried out in collaboration with Dr. Raquel Oro (Chalmers University of Technology).

Determination of the chemical state of each element is possible by performing narrow scans with high energy resolution in the characteristic binding energy ranges of the elements of interest. Surface composition is estimated by curve fitting the characteristics peaks and converting their intensity into apparent atomic concentration, using standard relative sensitivity factors [167]. Depth profiles can be carried out by sputtering the analysed surface with argon ions to etch the surface with controlled depths.

In the **Figure 20**b it is represented the spectra of iron compounds at different etching depths (1, 3, 5 and 10 nm). The contribution of each iron compound (at

elemental metallic state or oxidized cationic state) can be determined by fitting due to the well-known binding energies of each of them (706.7 eV for metallic Fe, 709.6 eV for Fe^{2+} and 710,8 eV for Fe^{3+}).

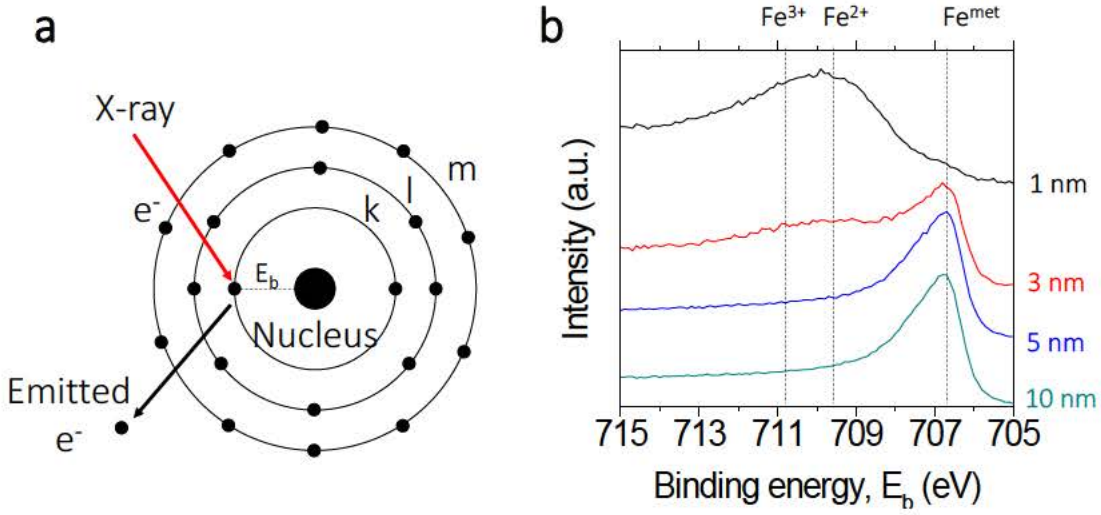

Figure 20 Photoelectric effect (a) and spectra obtained from different depth after etch at different depths (b), indicating the contribution of several chemical states of Fe.

3.5. Electron microscopy

Electron microscopy is an imaging technique based on the use of focused electron beams, which enables the characterization of morphology, microstructure and composition depending on the mode of use (**Figure 21**). Scanning mode makes use of electrons which are dispersed-back in angles lower than 90° with respect to the incident electron beam. Electrons can be backscattered due to elastic collisions with sample atoms, and their energy is dependent on the atomic number of the elements involved in the collision. These electrons are known as backscattered electrons and are used to generate images where compositional variations produces differences in intensity in the image. Incident electrons can also collide inelastically with the sample, which is ionized. Electrons emitted following this process are known as secondary electrons, and having less energy than backscattered electrons, are used to generate topography images. Incident electrons also generates the emission of characteristic x-rays from the sample, which corresponds to energy transitions in the atoms in the material. These x-ray can be collected to quantify the composition, giving rise to a technique called energy-dispersive X-ray spectroscopy (EDS).

When incident electrons have enough energy (up to 100 times higher than scanning mode), they can be transmitted through the sample, when it is thin enough. Electrons that are simply transmitted can be collected, which provide information about the morphology of the sample. Also, electrons can be diffracted and they are analysed for the structural determination of the sample.

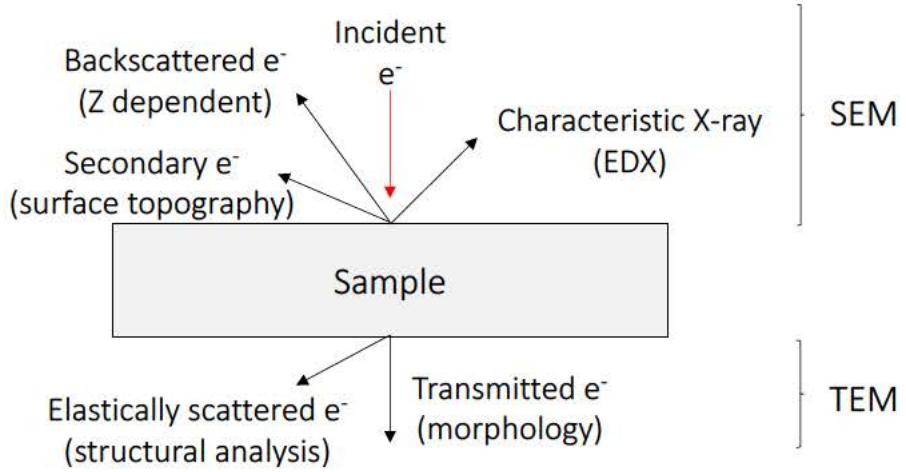

Figure 21 SEM and TEM modes used.

3.6. Atomic force microscopy

Atomic force microscopy (AFM) was used to measure carbon thin film thicknesses and surface roughness. AFM uses an oscillating and flexible cantilever with a very sharp tip which interacts with the surface of the sample, measuring local attractive or repulsive forces. A laser is reflected from the reverse side of the cantilever onto a position-sensitive photodetector, which transduces the reflected signal into cantilever position (**Figure 22**). The vertical deflection can be calculated by comparing signal from the "top" and "bottom" halves of the detector. The lateral twisting of the cantilever can also be calculated by comparing the "left" and "right" halves of the detector. AFM provides resolution on the order of fractions of a nanometer.

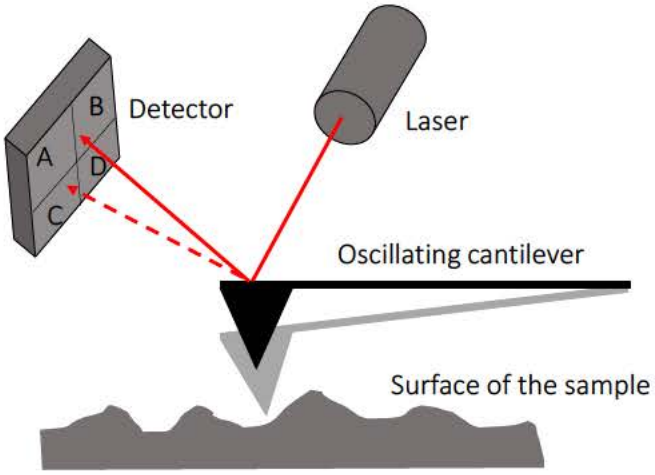

Figure 22 Schematics of AFM.

3.7. Other measurements and techniques

Electrical conductivity and optical transmittance measurements were carried to characterize the electrical and optical properties of carbon thin films, under collaborations with Dr. Pablo Aitor Postigo ("Instituto de Microelectrónica", Madrid), Estela Baquedano ("Instituto de Microelectrónica", Madrid), Dr. Javier Martínez (ISOM, Madrid), Dr. Alberto Boscá (ISOM, Madrid).

Surface wettability of carbon thin films were carried out under collaboration with Blanca Jalvo ("Universidad de Alcalá", Madrid), Dr. Javier Santiago-Morales ("Universidad de Alcalá", Madrid) and Dr. Roberto Rosal ("Universidad de Alcalá" and IMDEA Water Institute, Madrid).

4

Synthesis of carbon nanostructures on nickel and Invar powders

4.1. Introduction

In this chapter the experimental results on the use of commercial metal powders as catalyst for the direct synthesis of carbon nanostructures by cCVD are presented. The interest of using commercial metal powders as catalyst lies on its mass availability in a wide range of compositions, so they can be considered as metal catalysts for the mass production of carbon nanomaterials.

We have selected two metal powders with different composition and similar diameters, which are nickel and Invar ($Fe_{64}Ni_{36}$) powders. In this Chapter, we aim at demonstrating the scalability of the cCVD process by producing large amounts of carbon nanomaterials with different qualities and morphologies, and at understanding the interaction mechanism between pure nickel and Invar powders with the reactant atmosphere at high temperatures (argon, H_2, and C_2H_4 at 530ºC-830ºC). We provide explanations of metal-carbon interaction based on the literature regarding the synthesis of carbon nanofibers by cCVD as well in the framework of the carbon-based corrosion mechanism "metal dusting". We found the related bibliography especially instructive, despite the atmospheres considered there (CO, H_2 and H_2O) are different.

We show that, by controlling the temperature and metal composition during the CVD process, we selectively synthesize different shaped nanostructures with high yields, such as octopus-like carbon structures composed of several carbon fibres, a wide variety of carbon nanofibers, nanotubes and nanocoils from 50 to 200 nm in diameter and metal-graphite core-shell structures up to 500 nm. The results presented in this chapter have been summarized in two scientific papers currently under review.

4.2. Experimental procedure

4.2.1. Chemical vapor deposition

Commercial nickel (Alpha Aesar, 99.8%) and Invar powders (Sandvik Osprey, $Fe_{64}Ni_{36}$) were used as a catalyst for the direct synthesis of carbon structures by CVD. A controlled mass of 100 mg of the catalyst (one experiment per catalyst, time and temperature) was placed on a ceramic boat inside a custom-made moving tubular CVD reactor (Nabetherm, R50/250/12). Once the continuous reactor was sealed, all the lines connected to the system were flushed for 10 minutes, followed by 10 additional minutes of Ar to displace trapped air from the system. The furnace was ramped to the synthesis temperature with 100/400 sccm of Ar/H_2 flowing, keeping the sample outside the heating zone. Three synthesis temperatures were used (530, 680, 830ºC). Once the required temperature was reached and stabilized in the reaction zone of the furnace, the furnace was rapidly moved (*ca.* 3 s) until the sample was located in the middle of the heating zone. At this stage, the powder was annealed for 5 minutes under the same atmosphere, stepping from room temperature to the selected synthesis temperature. After the pretreatment, the reactant mixture of $Ar/H_2/C_2H_4$ (100/400/100 sccm) was introduced to proceed with the synthesis step, for different reaction times up to 24 h. After the synthesis step, the furnace was moved away from the sample to rapidly cool to room temperature (*ca.* 15ºC/s from 800 to 600ºC). During the cool down, Ar was flushed through to purge any reactive gases out of the system. The resulting mass was directly measured after the synthesis.

4.2.2. Characterization of carbon structures and metal catalysts

Carbon structures were analysed by using scanning electron microscopy (SEM, EVO MA15, Zeiss) and transmission electron microscopy (TEM, JEOL JEM 3000F and FEI Talos F200X). For TEM sample preparation, a solution of the powder and isopropanol was dispersed by bath sonication, and a drop of the solution placed over a TEM copper grid. The bath sonication most likely separated the carbon fibres from the catalyst, so most of the fibres detected by TEM were isolated from the metal particles.

The as-synthesized carbon products were analysed by Raman spectroscopy (Jasco, NRS-5100). All the spectra were recorded directly after synthesis. Three measurements for each sample were taken by using a Nd:YAG green laser (534 nm, aperture: 4000 μm). Spectra were obtained for 2 × 20 s exposure over a range of 1000–2750 cm^{-1}. The effective laser power was 6 mW.

The as-received and as-synthesized powder were also analysed by using an X-ray diffractometer. In the case of nickel powders, a 2θ-range from 20 – 100º, with step size of 0.02º and 0.75 seconds per step was used, and 40 kV and 40 mA. In the case of Invar powders, an Empyrean PANalytical instrument also equipped with a copper-Kα source (λ=0.154 nm) was used for a better resolution of small peaks corresponding to carbide nanoparticles. The diffractograms obtained were compared with patterns contained in the database PCPDFWIN and thereby the characteristic peaks of each phase were identified with Ni 03-065-2865, NiO 01-089-3080, Invar 00-047-1405, ferrite 01-087-0721 and Fe_3C 03-065-2411.

Microstructural characterization of the cross-section of the as-synthesized powder was carried out to study the fragmentation behaviour under CVD conditions. The samples were embedded in resin and mechanically polished to a surface mirror finish. A thin layer of gold (1 nm) was deposited by sputtering over the polished samples to be analysed by using SEM (FIB-FEGSEM dual-beam microscope, Helios Nano Lab 600i, FEI). Focused ion beam (EVO MA15, Zeiss) was used to analyse the fragmented surface of powders and manufacture lamellas for TEM observation of Invar powders.

Carbon filaments synthesized at 530ºC on nickel powders were heat-treated in argon at 2400ºC for 1 hour in a graphitization furnace (CEIT), and explored by using TEM, since crystallographic changes upon high-temperature treatments may reveal the structure of the untreated carbon nanostructured fibres [168].

4.2.3. Thermodynamic calculation

The temperature dependence of thermodynamic stability of cementite was analysed by using a CALPHAD (CALculation of PHAse Diagram) type thermodynamic calculation. The isothermal sections of ternary iron-nickel-carbon system were calculated by using Thermo-Calc software with an in-house developed thermodynamic database. The database was assessed by synchronously evaluating the available thermochemistry and phase-diagram data. This part of the work was carried out in collaboration with by Dr. Guanlong Xu and Dr. Yuwen Cui.

4.3. Results of the synthesis on nickel powders

Next we present the results corresponding to the use of nickel powders as catalyst for the direct synthesis of carbon materials as a function of temperature.

4.3.1. Mass yield

First of all, we measured the size of 150 nickel particles by SEM; they were almost spherical, with an average particle size of 3.4 ± 2.2 μm (**Figure 23a**). As we will demonstrate later, this broad distribution has important consequences in the final products. Next, we analysed the mass production, the morphology and quality of the carbon nanomaterials and the role of the nickel powder at each synthesis temperature (530ºC, 680ºC, 830ºC).

Carbon materials directly grew on pure nickel powder by means of CVD without the need of any previous pretreatment of the catalyst. The carbon yield as a function of synthesis time ([carbon mass produced + catalyst mass used] / catalyst mass used) is shown in **Figure 23**b and followed a linearly increasing trend. The carbon yield was lower and nearly negligible at the intermediate temperature (680ºC) compared to those obtained at 530ºC and 830ºC. Particularly, after 240 minutes of synthesis, the carbon yield reached values of 43 at 530ºC and 9 at 830ºC, meanwhile at 680ºC the yield barely reached 0.2, regardless of synthesis time. Thus we focused on CVD conditions at 530ºC and performed a longer synthesis for 24 hours to identify a possible decrease in the catalytic activity. At 530ºC, we obtained a very high yield superior to 400.

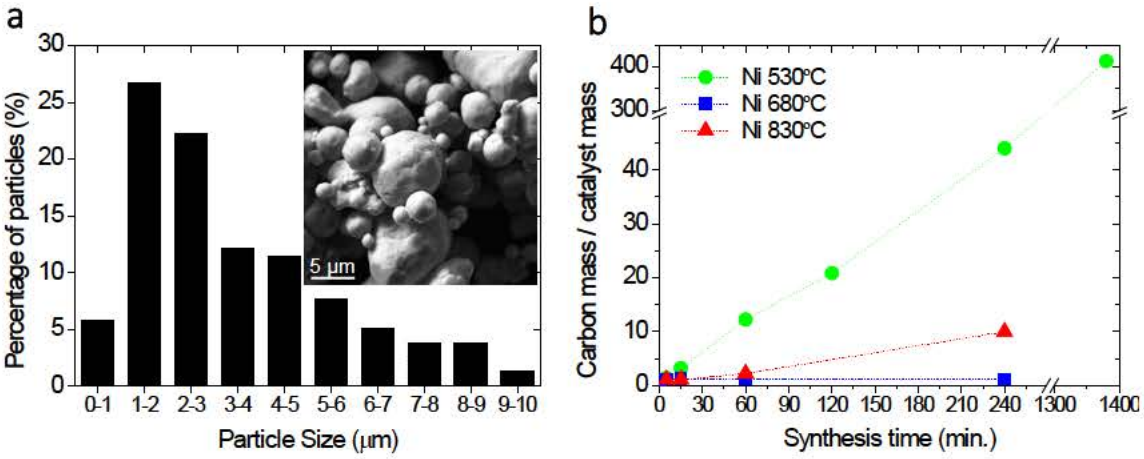

Figure 23 a) SEM image and diameter statistics of as-received nickel powder showing a particle size of 3.4 ± 2.2 μm; about 80% of the particles are smaller than 5 μm. b) Carbon-to-catalyst mass ratio after synthesis at 530°C, 680°C, and 830°C versus synthesis time on nickel powder. A carbon-to-catalyst mass ratio of about 43 was obtained after 240 minutes of synthesis at 530°C and 0.2 at 680°C regardless of the synthesis time. At 830°C, catalytic activity is partially recovered obtaining over 9 g of carbon per gram of catalyst after 240 minutes. After almost 1400 minutes at 530°C of synthesis, we obtained 165 mg of carbon deposits from 0.4 mg of nickel powder, which represent a mass ratio increase of about 400.

4.3.2. Characterization of carbon structures

A general SEM and TEM overview of the carbon nanostructures synthesized over 60 minutes at different temperatures is shown in **Figure 24**. Different microstructures were found depending on the CVD temperature used. At 530°C, several fibres grew from the same nickel particle, forming octopus-like structures, such as the 3-μm-sized and 20-μm long structure with six arms and a nickel micron-sized particle in the middle (**Figure 24**a).

As expected, the carbon arms had different diameters depending on the nickel particle from which they grew, and we found multi-armed structures having two to six arms. A similar growth mechanism was reported by Motojima *et al.* that used acetylene and nickel powder as catalyst but thinner and coiled fibres up to 1 μm in diameter were obtained [169], [170] in a yield of 1 at about 600°C. We further analysed these products by TEM (**Figure 24**d), where we only were able to observe the thin structures (<500 nm). Four different types of structures were identified: 1) broad fibres of *ca.* 400–500 nm with carbon discontinuities in the centre (as shown

in **Figure 24**a) smooth surface and solid nanofibers of *ca.* 100 nm, 3) curly nanofibers of *ca.* 25 nm, and 4) very thin nanofibers down to 10 nm.

When we increased the synthesis temperature to 680ºC, no carbon fibres were obtained (**Figure 24**b). On the contrary, CVD led to a graphitic covering of the nickel micron-sized powder instead, as depicted in TEM image (**Figure 24**e). This graphitic covering, which was about 100–200 nm thick after 60 minutes of synthesis, explains the low yield obtained under these conditions. However, when the synthesis took place at 830ºC, a large quantity of nickel–graphite core-shell nanoparticles of up to 1 μm diameter within a carbon matrix were formed (**Figure 24**c, f).

Given the high yield of carbon fibres obtained at 530ºC of synthesis temperature, we decided to go further in their characterization after heat treatment at 2400ºC [168]. This thermal treatment is known to develop graphitic structures related to the original structure of carbon fibres, so its analysis is useful to determine the nature of the carbon fibres produced at first instance. The thermal treatment revealed that "type 1" fibres (**Figure 25**b,c) were spiral-ribbon structures along the axis, "type 2" had a solid fishbone structure (**Figure 25**d,e), "type 3" had a clear platelet structure (**Figure 25**f,g), and "type 4" were small fishbone nanofibers that had been greatly transformed after the heat treatment (**Figure 25**h,i). This broad distribution on carbon nanofibers diameters are explained by the similar broad distribution on catalyst diameter, since they are correlated.

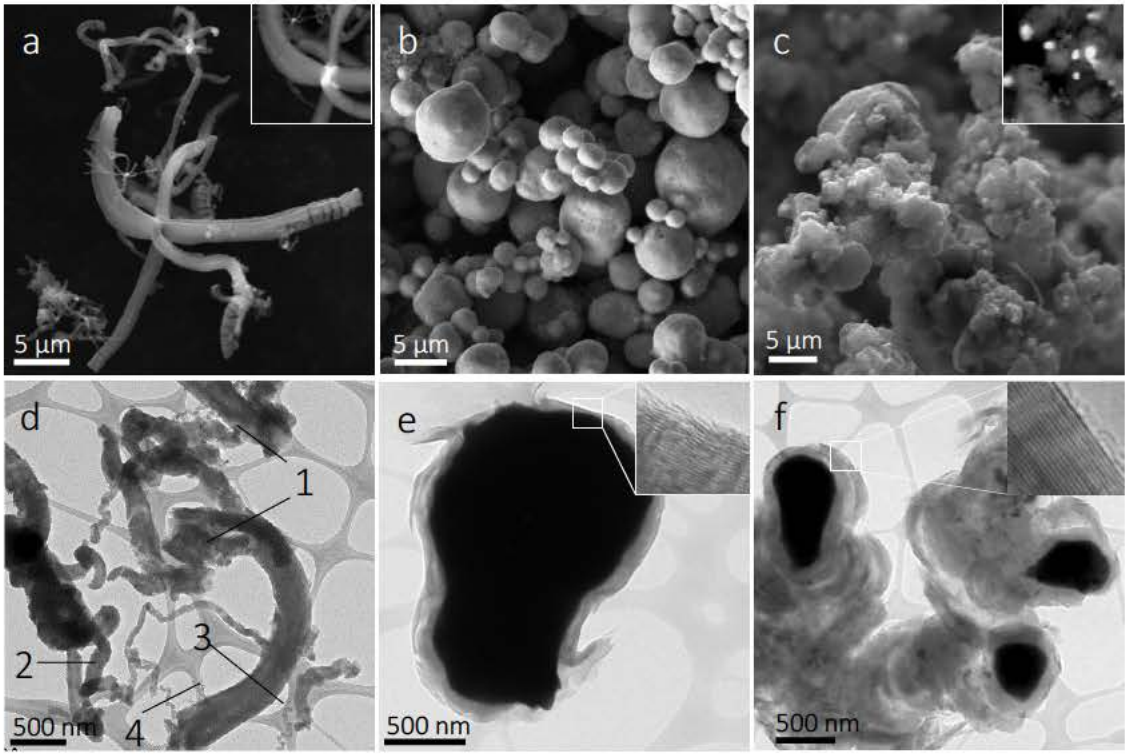

Figure 24 SEM / TEM images of the synthesized products at 530°C (a/d), 680°C (b/e), and 830°C (c/f) for 60 minutes. Insets in the SEM images (a-c) show backscattered electron signals, which highlight in lighter colour the nickel particles within the carbon. The synthesis at 530°C produced multi-armed structures of different diameters (d). The synthesis at 680°C did not produce an extensive formation of carbon nanostructures, but a graphitic covering instead (b, e). The synthesis at 830°C caused fragmentation of the powder into nanoparticles with a highly graphitic covering (c, f).

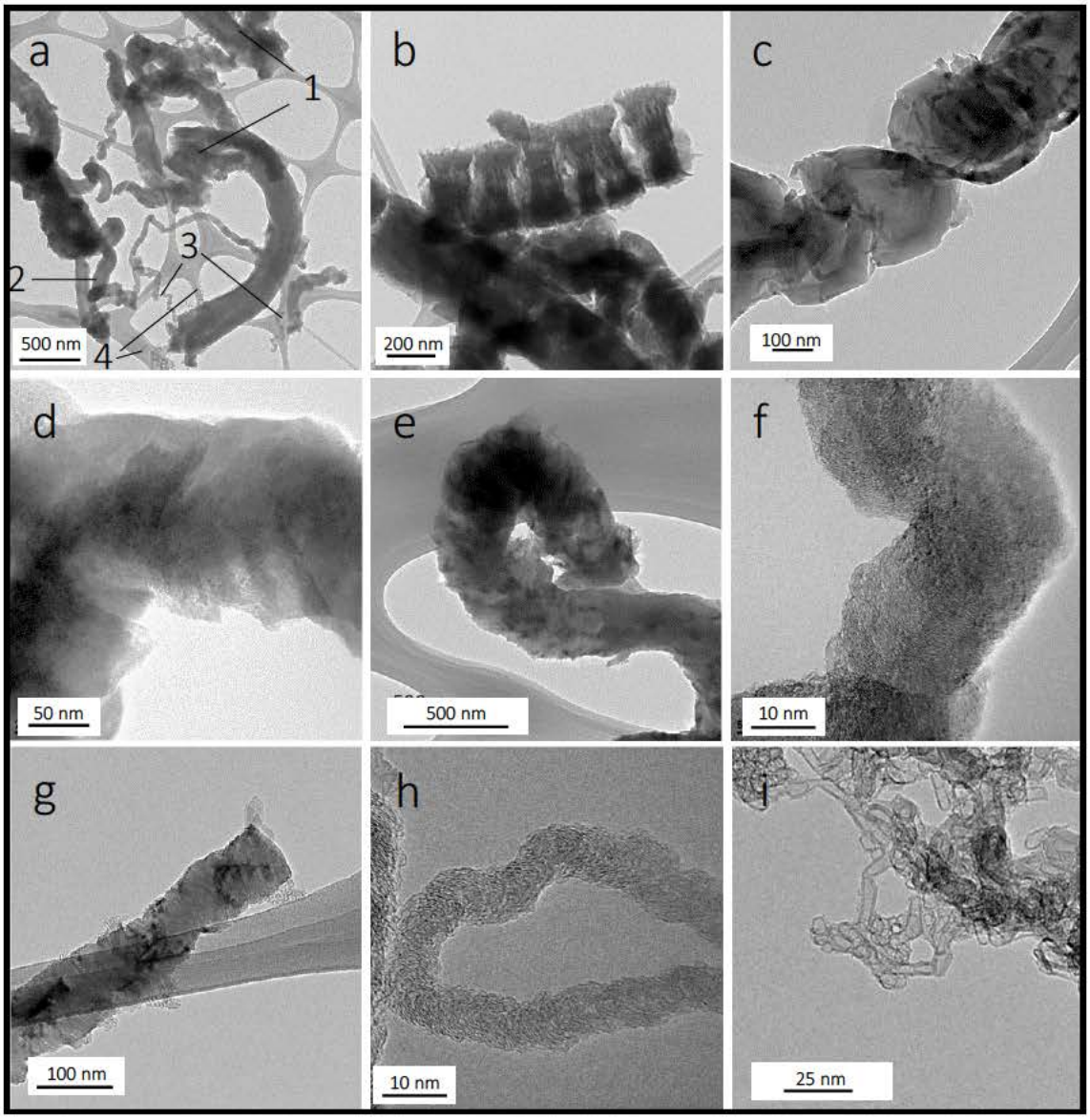

Figure 25 TEM details of thin carbon nanostructures (<500 nm) grown at 530°C, where a) shows a general overview of as-grown materials, with four main types according to diameter and structure, b) shows type 1 as-grown and c) heat-treated at 2400°C, indicating that discontinuities are due to the formation of the filament by helical carbon ribbons, d) type 2 CNFs consist of e) a fishbone structure when heat-treated at 2400°C, type 3 f) and g) curly filaments with a platelet structure, observed on both as-grown and heat-treated sample, respectively, and h) shows the type 4 nanofibers of very thin diameters that i) are converted into few-walled carbon structures after heat-treatment at 2400°C.

We performed a final characterization of the carbon structures by Raman spectroscopy and XRD analysis on as-grown powder, to compare the graphite crystal quality depending on the temperature of synthesis. As expected, an enhancement of the graphite quality was observed when the synthesis temperature was increased from 530°C to 830°C. Both D band (related to defects in graphite, *ca.* 1350 cm^{-1}) and G band (related to crystal order in graphite, *ca.* 1580 cm^{-1}) were present for all the CVD conditions (**Figure 26**a) [166]. Also, all spectra showed the presence of the D′ peak (shown as an asymmetric G peak in 530°C sample) that is indicative of a high concentration of graphite edges.

The reduction of the intensity of the D band compared to the G band and their full width half maximum, as well as the emergence of the 2D band at about 2680 cm^{-1}, are all signatures of the increase of graphite quality. The 2D sharp peak is related to the highly crystalline few-layer graphene structure, and that at about ~2450 cm^{-1} is originated by the combination of D (~1340 cm^{-1}) and D″ (~1100 cm^{-1}) defect-related bands.

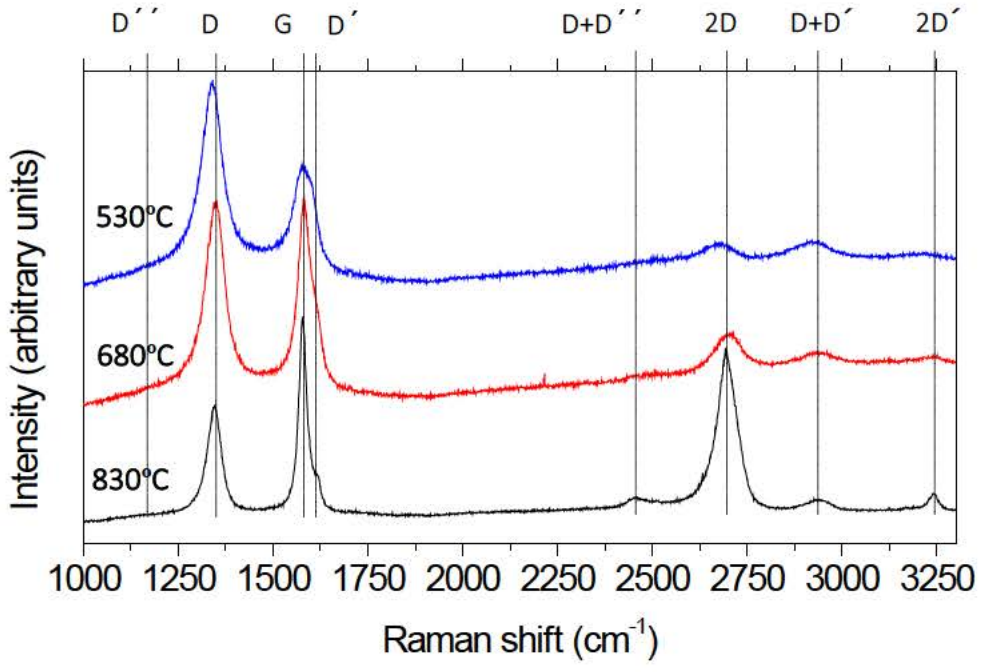

Figure 26 Raman spectra of the as-synthesized samples for different temperatures. The reduction of the intensity of the D band (1350 cm^{-1}) compared to the G band (1580 cm^{-1}), D and G full width half maximum, and the emergence of the 2D band (2680 cm^{-1}), indicated the increase of graphite quality.

The XRD analysis confirmed the increase of graphite quality by the reduction of the full width half maximum of the (002) peak of graphite, at about 26.5° (**Figure 27**). A very small peak is detected at 680°C, in agreement with the very low carbon deposition at these conditions. On the other hand, no new phases (nickel carbides) were formed during CVD, in agreement with recent reports [95].

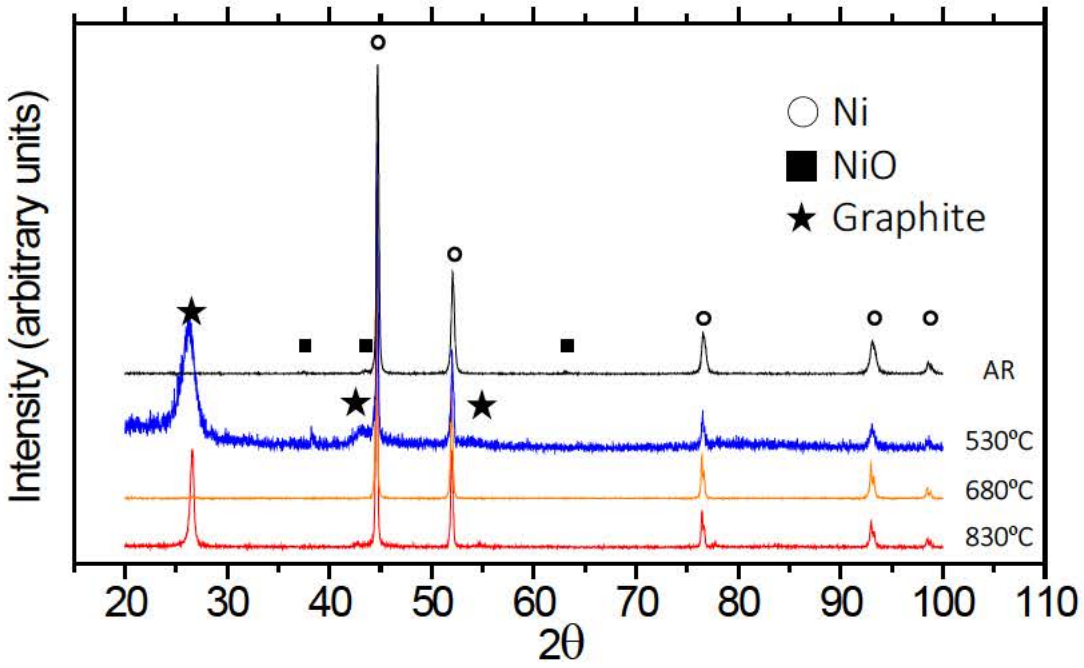

Figure 27 XRD analysis confirmed an increase in graphite quality by the reduction in full width half maximum of the (002) peak of graphite, at about 26.5°. The very low signal at 680°C is in agreement with the very low level of carbon deposited under these conditions.

4.3.3. Characterization of metal particles

Cross sectional analysis of nickel particles give important information about the growth mechanism of carbon structures at different temperatures. We have detected that at 530°C, nickel particles adopted polyhedral morphologies (**Figure 28**a), which is associated with the multi-armed growth mechanism shown in **Figure 24**a. When the synthesis temperature was increased up to 680°C, nickel powders revealed a spherical shape, as expected from the SEM results (**Figure 24**b and e), meanwhile the nickel surface suffered fragmentation at 830°C (**Figure 28**c) which explains the production of nickel–graphite core-shell nanoparticles at this temperature (**Figure 24**c and f).

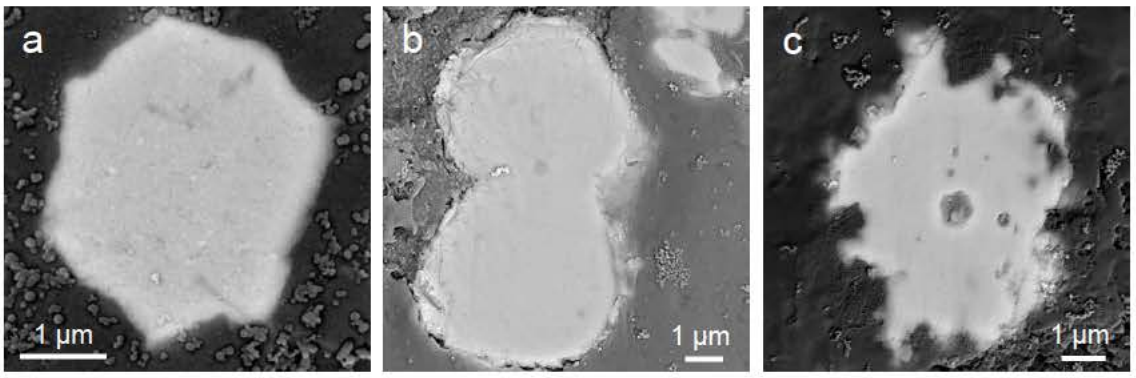

Figure 28 SEM of nickel powder cross-sections when heated to different temperatures for 60 minutes. a) Nickel particles showed polyhedral morphologies at 530°C on top of which the octopus-like structure grew. b) At 680°C, the nickel powder showed a spherical shape. c) At 830°C, the nickel surface suffered fragmentation.

4.3.4. Discussion on multidirectional growth mechanism

A deeper study was carried out on the growth mechanism at 530°C, which is of great interest from an industrial point of view due to its very high yield and low temperature of the process. Over the longer term growth (24 h), structures grew following the multi-armed mechanism up to 100 µm in length (**Figure 29**a), which explains the very high yield obtained. The nickel catalyst can easily be identified in the images as a bright particle in the middle of the fibres of several sizes (**Figure 29**c-f), showing a clear polyhedral morphology (**Figure 29**d). Very interestingly, the morphology of the facets of the polyhedral nickel particles were reproduced on the growing carbon fibres, as shown in the inset (**Figure 29**b).

In the last decades, intense attention has been paid to the role of nickel surfaces during carbon adsorption/deposition, either in studies focused on the microscopic fragmentation [153]–[161] and surface reconstruction [171], [172] of metal surfaces, or on the growth of monolayer graphene [68]–[70]. Here, we found three different morphologies of nickel catalyst depending on the temperature of synthesis, which were i) polyhedral/faceted at 530°C, ii) spherical at 680°C, and iii) fragmented at 830°C, which can be explained by the nickel reconstruction and fragmentation processes described below.

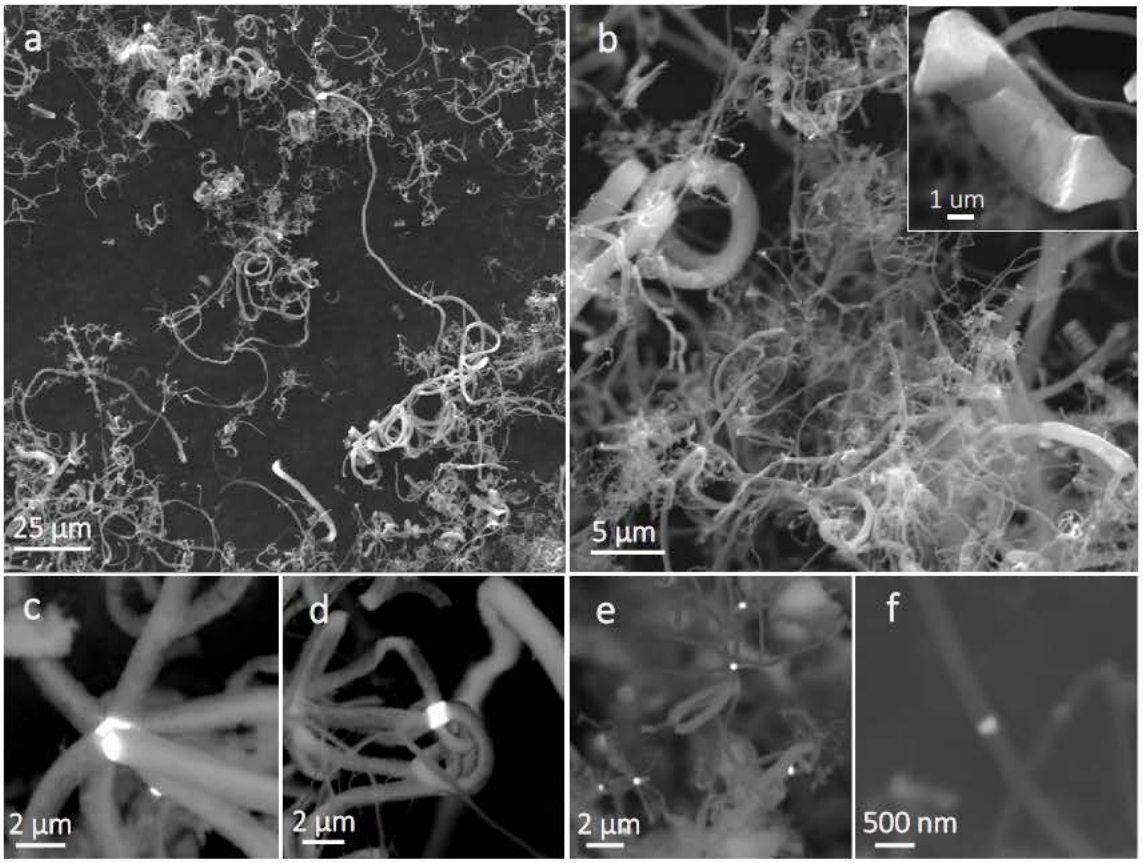

Figure 29 Carbon structures synthesized on nickel powder at 530°C after 1400 minutes, showing that the arms of the multi-armed structures grew up to 100 µm long (a), which explains the high yield obtained. The nickel catalyst can be identified in the images as a bright particle in the middle of the fibres (c-f), and its polyhedral morphology can be clearly seen (d). The morphology of the facets of the nickel catalyst were reproduced on the growing carbon fibres, as shown in the inset (b).

On one hand, polyhedral morphologies of nickel powder at 530°C (**Figure 28**a), on which the directional growth of carbon fibres has occurred, may be produced by the continuous extraction of nickel atoms from the facets from which the carbon filaments grow. This nickel ejection from the surface is believed to be produced by surface stress induced by carbon dissolution [70], [173]. To confirm the possible extraction of nickel atoms, we performed TEM energy-dispersive spectroscopy analysis on an arm from a multi-armed structure (**Figure 30**). Our result indicated the presence of nickel in the analysed fibre, despite we could not detected it in the image. Thus, the ejection of nickel atoms from the surface of the powder can explain, at least partially, the final polyhedral morphology.

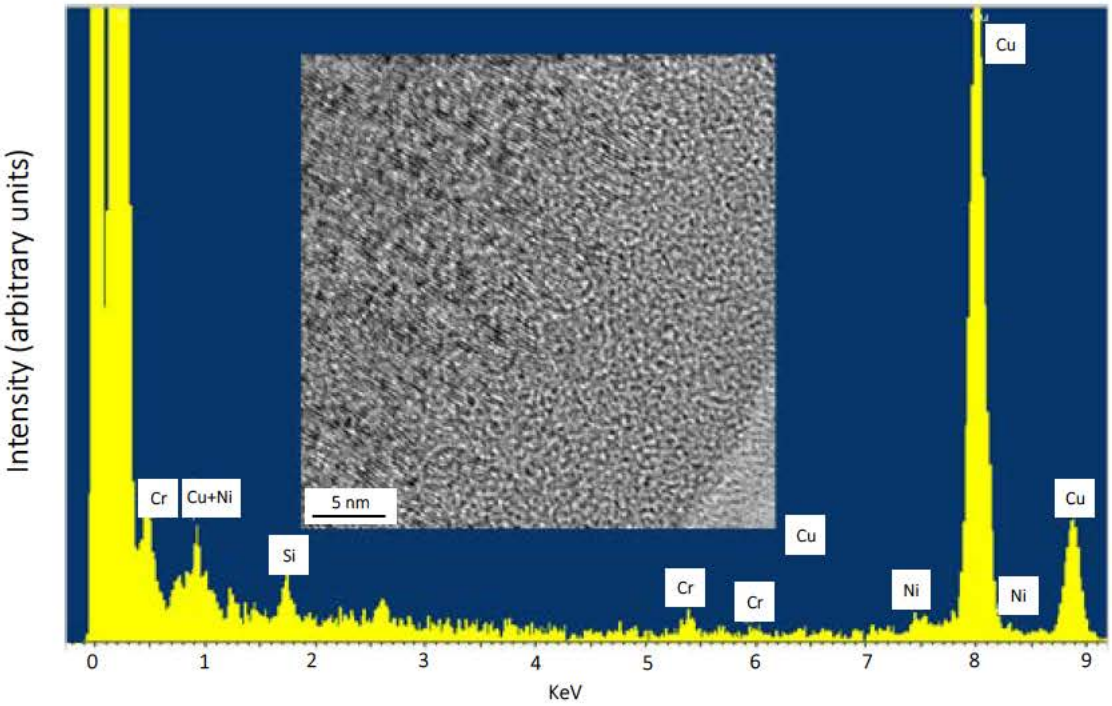

Figure 30 Nickel atoms may be present within the carbon fibres, most likely caused by the continuous extraction from the facets where carbon arms grow. Chromium signal corresponds to the TEM sample holder and silicon from the glass from which powder sonication took place for the sample preparation.

On the other hand, at temperatures close to the melting point, metal nanoparticles can adopt polyhedral shapes composed by surface facets that correspond to their minimum surface energy, known as equilibrium crystal shapes or Wulff shapes [174]. It is also known that the kinetics which lead to the development of these polyhedral and faceted shapes are accelerated when carbon is in solid solution in the nickel lattice, because dissolved carbon creates surface stress which facilitates surface diffusion of nickel atoms [175].

Since the Wulff reconstruction effect can take place at lower temperatures by the effect of carbon adsorbates, polyhedral and faceted nanoparticles are usually found inside CVD-grown carbon nanofibers synthesized at temperatures far from the melting point [16], [94], [125], [145]. In this regard, our nickel particles may not have energy enough to develop spherical surfaces at 530°C due to their relatively large micrometre size [174], but may still have enough to develop large facets, most likely due to the presence of dissolved carbon. As a consequence, the carbon fibres can grow by carbon surface diffusion [176]–[178] following the direction which requires the

lowest energy (**Figure 31**b), which at the same time leaves a free path for the hydrocarbon to reach the nickel surface and keep the growth for longer times. As expected, different polyhedral shapes would develop on the nickel particles depending on their diameter [174] and, due to the variation of activation energy for carbon diffusion on each facet [179], multi-armed structures with several arms and of varied sizes may grow. With all this, it is reasonable to think that the ejection of nickel atoms from the surface of the nickel particle may only happen on those facets where the fibres grow, so our hypothesis is that polyhedral shapes may be created by a synergistic effect between nickel atoms ejection and Wulff reconstruction processes during the CVD process.

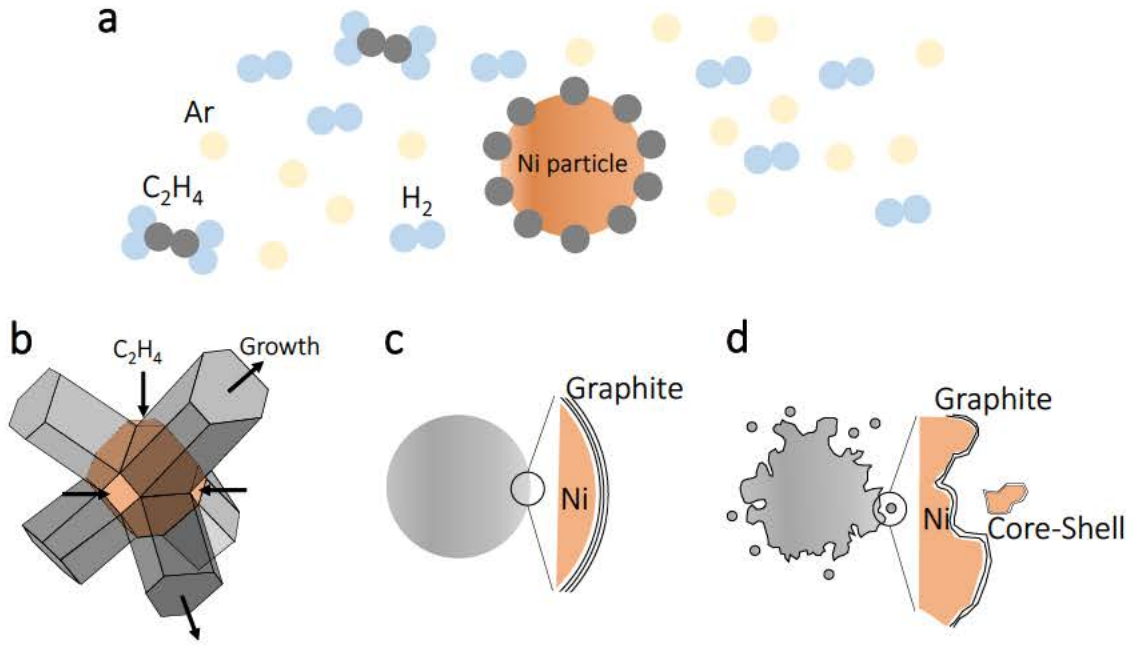

Figure 31 Idealized scheme of the CVD process of carbon structures on nickel powder using C_2H_4 as carbon source, H_2 and argon. Multi-armed carbon structures grew from polyhedral/faceted nickel particles at 530°C (b), a graphitic covering was deposited on spherical particles at 680°C (c), and nickel–graphite core-shell nanoparticles were produced by nickel fragmentation at 830°C.

Following a similar argument, higher energy is available at 680°C, so the surface reconstruction of nickel particles may be facilitated under the carburizing atmospheres [175]. At this temperature we found spherical nickel particles covered by few-layer graphene. This scenario, together with the faster carbon deposition from ethylene source and faster diffusion kinetics due to the higher temperature, would

explain the spherical shapes of nickel at this temperature (**Figure 28**a), on top of which the carbon deposited as a graphitic covering (**Figure 31**c). It is believed that carbon surface diffusion may control the carbon deposition in our 530–680ºC experiments [177], [178]. However, carbon bulk diffusion and solubility increases at 830ºC [67], [180], which generates the growth of graphitic planes inward the nickel powder and its further fragmentation (**Figure 31**d), as explained in the metal dusting phenomena [162], [163].

4.4. Results of the synthesis on Invar powders

Next, the results corresponding to the use of Invar powders ($Fe_{64}Ni_{36}$) as catalyst for the direct synthesis of carbon nanomaterials as a function of temperature are presented. The effect of alloying the metal catalyst with iron in comparison to the use of pure nickel has important implications in the fragmentation of Invar powders and the production of carbon nanofibres.

4.4.1. Mass yield

Following the similar procedure presented in the section 4.3, the mass production of carbon deposits, the morphology and quality of the carbon materials was analysed, as well as the role of the Invar powder at each synthesis temperature. First of all, we measured the size of 150 Invar particles by SEM; they were almost spherical, with an average particle size of 1.69 ± 0.91 μm (**Figure 32**a).

The carbon yield (carbon mass/catalyst mass) was found to increase linearly with the synthesis time (**Figure 32**b), and the lowest yield was obtained when synthesizing at 680ºC, as happened with the nickel powders. Particularly after synthesis during 240 minutes, the carbon yield reached values of 30 at 530ºC (43 using nickel), 12 at 680ºC (0.2 using nickel) and 22 at 830ºC (9 using nickel), which are in the order of other studies [159], [181]. The value obtained at 680ºC and 830ºC are larger than those obtained with nickel powders.

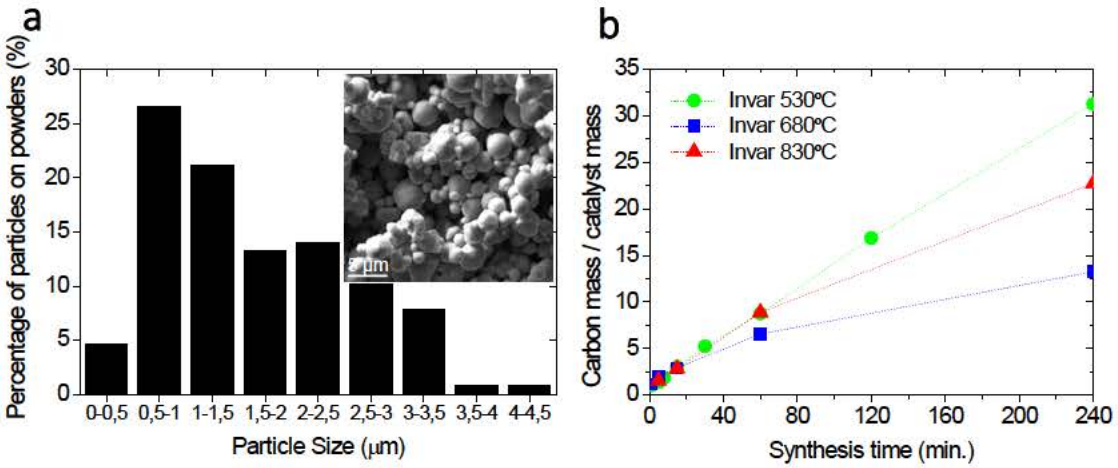

Figure 32 a) SEM image and diameter statistics of as-received Invar powder showing a particle size of 1.69 ± 0.91 μm; about 90% of the particles are smaller than 3 μm. b) Carbon-to-catalyst mass ratio synthesized on invar powders at 530°C, 680°C and 830°C as a function of synthesis time. After synthesis for 240 minutes at 530°C, the carbon yield reached values of 30. At 680°C, the Invar moderately kept its catalytic activity yielding 12. Interestingly, the carbon yield partially recovered at 830°C, yielding 22.

4.4.2. Characterization of carbon structures

Carbon nanostructures synthesized on Invar powders for 60 minutes were analysed by SEM (**Figure 33**). Synthesis at 530°C resulted in an extensive formation of carbon nanofibers (**Figure 33**a). Fragmentation of Invar powders was visible using the backscattered detector in SEM (insets in **Figure 33**), which showed bright dots that corresponded to metal nanoparticles from which nanofibers and nanotubes grow. A high quantity of big nanoparticles within a carbon matrix were produced at 680°C. In this case the carbon nanofibers were hardly visible by SEM. Finally, no formation of nanofibers but a high quantity of nanoparticles and carbon was obtained at 830°C (**Figure 33**c).

As an example, we show the carbon deposited on Invar particle after synthesis for 1 minute at 530°C in a transmission electron microscopy image (**Figure 34**). As it can be clearly observed, heterogeneous and discontinuous structures are formed on the surface of an Invar particle, like a graphitic covering, nanofibers and nanoparticles. This heterogeneous deposit on Invar particles was accompanied by the fragmentation of its surface. This fragmentation created new catalytic nanoparticles that enabled the growth of the carbon nanofibers on **Figure 33**a.

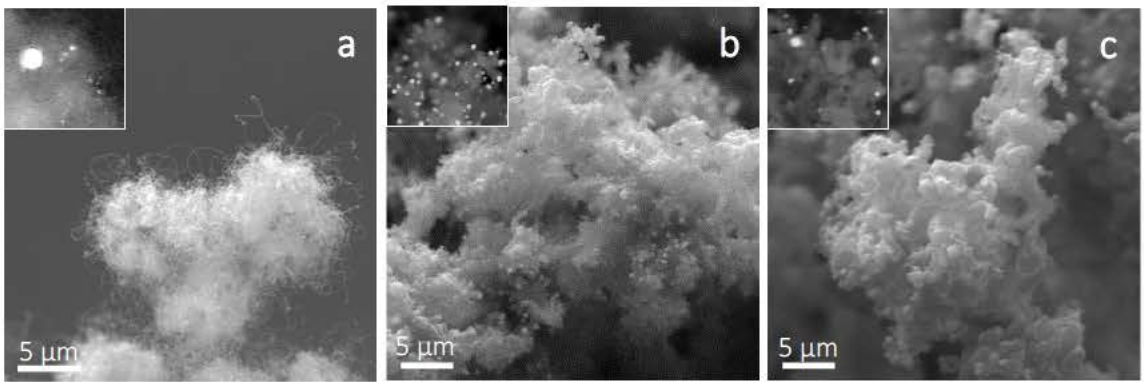

Figure 33 SEM images of the synthesized products at 530°C, 680°C and 830°C (a-b-c) during 60 minutes. Insets in the images are backscattered electron signal, whose contrast depend on the atomic number of the analyzed elements and are used to detect the metallic particles. Synthesis at 530°C on Invar powders resulted in an extensive formation of carbon filaments. Some carbon filaments were also produced on Invar at 680°C, as well as a higher quantity of nanoparticles within a carbon deposit. Finally, no extensive formation of fibres but a high quantity of nanoparticles within a carbon matrix were produced at 830°C.

As CVD progressed for 60 minutes at 530°C, the nanoparticles produced by surface fragmentation led to the growth of a wide variety of nanostructures like nanofibers, nanotubes and nanocoils from 50 nm to 200 nm in length (**Figure 35**a). Similarly, at 680°C most of the nanofilaments produced were fishbone-like carbon nanofibers and multiwall carbon nanotubes (10-20 nm of external diameter with about 10-20 walls), however metal-graphite core-shell nanoparticles up to 100 nm were detected as the main product at these conditions (**Figure 35**b). Finally, at 830°C the powders fragmentation produced an extensive formation of metal-graphite core-shell nanoparticles up to 500 nm (**Figure 35**c) and no carbon nanofibers were detected at these conditions.

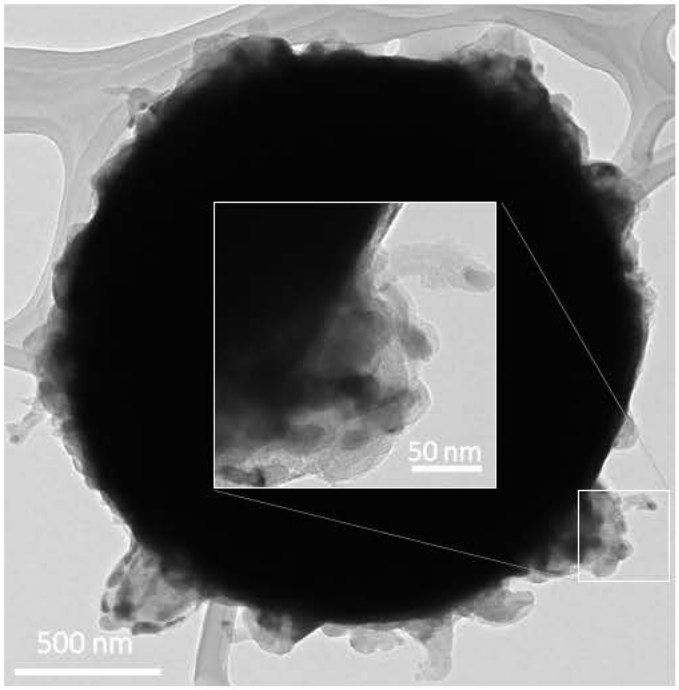

Figure 34 TEM image of an Invar particle after synthesis at 530°C for 1 minute. Carbon deposition on Invar was heterogeneous along its surface.

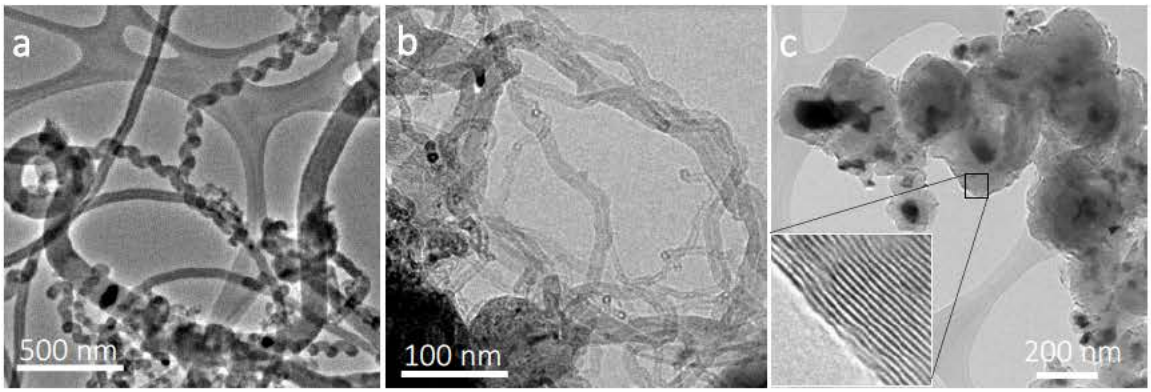

Figure 35 TEM images of the synthesized products at 530°C, 680°C and 830°C (a-b-c) during 60 minutes. A wide range of carbon nanofibers were obtained at 530°C (nanocoils, fishbone-like nanofibers and multiwall CNTs). At 680°C, several carbon nanofibers and tubes were also detected as well as metal-graphite core-shell nanoparticles, and only metal-graphite core-shell nanoparticles up to 500 nm at 830°C.

Similarly to those results obtained with nickel particles, we confirmed the enhancement of graphite quality with the synthesis temperature by means of Raman spectroscopy (**Figure 36**), as indicated by the reduction of the D band (1340 cm^{-1}), the G band width (1570 cm^{-1}) and the increase of 2D band intensity (2680 cm^{-1}). The band at about 2450 cm^{-1} is originated by the combination of D (1340 cm^{-1}) and D″

(1100 cm^{-1}) bands. The band at about 2950 cm^{-1} is originated by the combination of D (~1340 cm^{-1}) and D′ (~1620 cm^{-1}) bands.

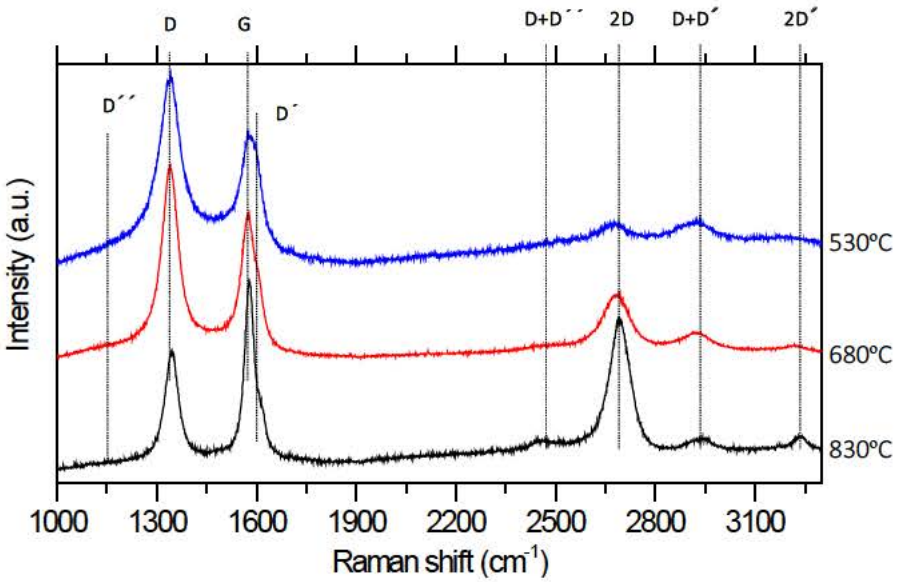

Figure 36 Raman spectra of the as-synthesized samples at different temperatures. It was confirmed the enhancement of graphite quality with the synthesis temperature, as indicated by the reduction of the D band (1340 cm^{-1}), the G band width (1570 cm^{-1}) and the appearance of the 2D band (2680 cm^{-1}). The band at about 2450 cm^{-1} is originated by the combination of D and a weak D″ (1100 cm^{-1}) bands. The band at about 2950 cm^{-1} is originated by the combination of D and D′ (1620 cm^{-1}) bands.

4.4.3. Characterization of metal particles

Next, we focus on the analysis of the Invar powders and the nanoparticles produced during CVD. As explained in the introduction section, fragmentation of iron-nickel alloys under CVD conditions is likely to be produced through the formation of carbides due to the presence of iron. In this regard, we performed XRD analysis on bulk powders on as-received and as-synthesized states in order to detect any phase transition (**Figure 37**). XRD spectra on as-received powders confirmed the presence of Invar (austenite γ-phase), as well as a slight amount of iron (ferrite α-phase). For the synthesis conditions of 530ºC, new peaks slightly raised at about 37.7º, 39.8º, 40.6º, 45.0º, 45.9º, 48.6º and 49.1º that fitted well with cementite (Fe_3C orthorrombic Pnma, space group 62). However, no cementite signal were obtained for 680ºC and 830ºC.

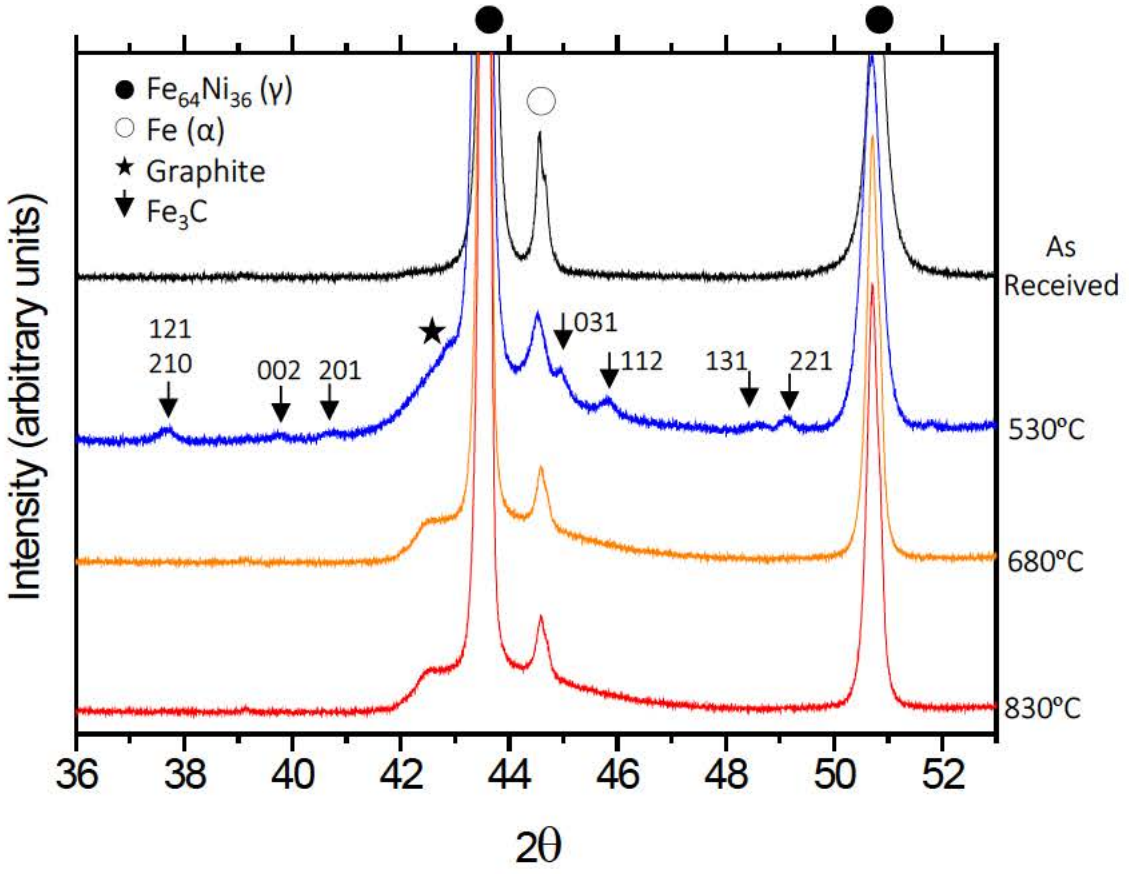

Figure 37 XRD spectra of invar powders for different conditions. The presence of Invar (austenite γ-phase) as well as a slight amount of iron (ferrite α-phase) is confirmed on as-received powder. For the synthesis conditions of 530°C, new peaks at about 37.7°, 39.8°, 40.6°, 45.0°, 45.9°, 48.6° and 49.1° fit well with cementite (Fe_3C orthorhombic Pnma, space group 62). No cementite signals were obtained for 680°C and 830°C. Ferrite α-phase is identified at all conditions.

Cementite identification at 530°C by XRD was complemented by chemical and microstructural analysis on a cross section of an Invar microparticle manufactured by focused ion beam (**Figure 38**a) as well as on the extracted nanoparticles inside the carbon nanofibres (**Figure 38**b). Interestingly, we found by chemical analysis of a line scan along an Invar particle at 530°C an iron-depleted zone in its surface, whose composition changed from the bulk Fe/Ni=64/36 to Fe/Ni=50/50 in the surface. Contrary, the nanoparticles inside the helical nanofibers showed an iron-enrichment with compositions of about Fe/Ni=(88.4±1.9) (11.4±1.9), whose electron diffraction pattern fitted well with the same Fe_3C orthorrombic phase identified by XRD on these samples, in agreement with other studies on the catalytic growth of carbon nanocoils [89].

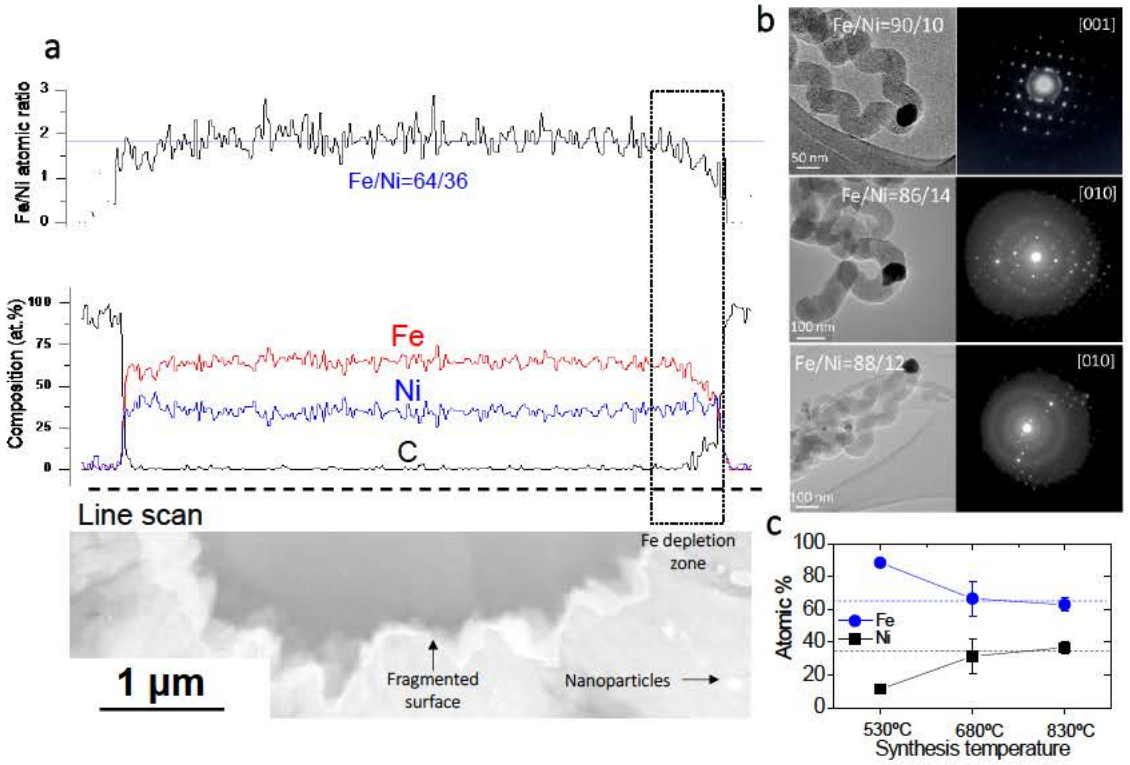

Figure 38 a) Cross section of invar particle after CVD at 530°C manufactured by focused ion beam and observed in a TEM microscope. Line scan chemical analysis by energy dispersive spectroscopy (EDS) showed an iron-depleted zone in the surface of the Invar particle, whose composition changed from the bulk Fe/Ni=64/36 to Fe/Ni=50/50 in the surface. b) TEM images, chemical composition and selected area diffraction patterns of nanoparticles inside the carblon nanocoils synthesized at 530°C on Invar powders, showing an iron-enrichment from Fe/Ni=64/36 up to Fe/Ni=90/10, and Fe_3C orthorhombic microstructure, in agreement with XRD studies. c) Evolution of the composition of the nanoparticles produced during synthesis a different temperatures.

Interestingly, the nanoparticles extracted from the powders during synthesis at higher temperatures showed compositions closer to the Invar, Fe/Ni = (66.6 ± 10.3)/(31.4 ± 10.3) at 680°C and Fe/Ni = (62. 9 ± 3.9)/(36.8 ± 3.9) at 830°C (**Figure 38**c), presenting always the same Invar austenite structure, in agreement with the XRD results. Despite the composition of the metal nanoparticles pulled-out from Invar powders during the CVD depends on the synthesis temperature, Invar powders cross sections showed very similar fragmented morphologies at all temperatures, as shown on cross-section SEM images in **Figure 39**. However, fragmentation at 530°C takes places by the metal dusting carbide route, meanwhile fragmentation at 680°C and 830°C take place by graphite inward growth [153]–[163]. We discuss this difference in the next section.

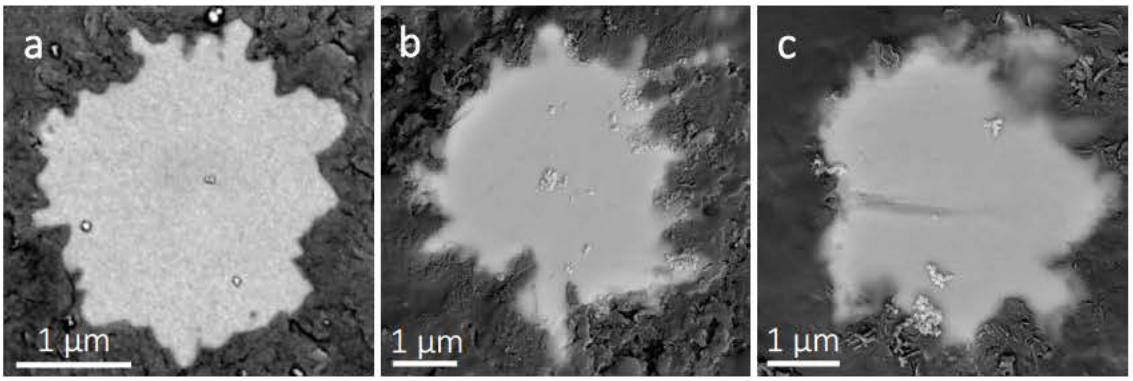

Figure 39 Cross-sectional SEM of powders after synthesis at 530°C, 680°C and 830°C (a-b-c) during 60 minutes. At all conditions, Invar powders showed a regularly broken surface produced by the carbon deposition during CVD.

4.4.4. Discussion on Invar fragmentation

The fragmentation of the Invar powders may be associated with i) the fast carbon diffusion along the phase boundaries between austenite and ferrite phases (which were revealed by XRD) and activated at high temperatures, and ii) the formation of carbides as explained in the metal dusting mechanism on iron alloys [153]–[163].

Despite our Invar alloy ($Fe_{64}Ni_{36}$) is above the critical nickel content to extensively form carbides (<30% nickel [153] and <5 nickel [160] in CO-H_2-H_20 atmospheres), they can be locally formed [160]. The authors explained that a selective corrosion of iron in Invar alloys caused by the lower chemical interaction of carbon and nickel, creates an iron-depleted zone through iron outward diffusion in the near surface, as we precisely observed in our FIB-lamella (**Figure 38**a). This selective outward diffusion kinetics enable the necessary stoichiometric shift for carbide formation, at least locally, in the surface. The further carbon deposition isolate the carbided surface from the atmosphere and they become unstable, producing its rupture [157]. Fortunately, this carbide fragmentation creates the necessary nanoparticles for the growth of nanofibers, explaining why they are only extensively produced at 530°C.

We confirmed the presence of carbides by selected area electron diffraction and XRD analysis after synthesis at 530°C, however no cementite was detected at higher temperatures (**Figure 37**a). This cementite absence at 680°C and 830°C is supported by our calculated isothermal sections of iron-nickel-carbon (**Figure 40**), where the

carbon-dissolved Invar alloy situates in an extended austenite single-phase region as the temperature is increased. In the case of CVD at 680°C and 830°C, Invar powders may break most likely due to phase boundary carbon diffusion, producing nanoparticles whose composition are much closer to the original Invar powders that, together with the higher level of ethylene dissociation at these high temperatures, resulted in carbon-metal core-shell structures instead.

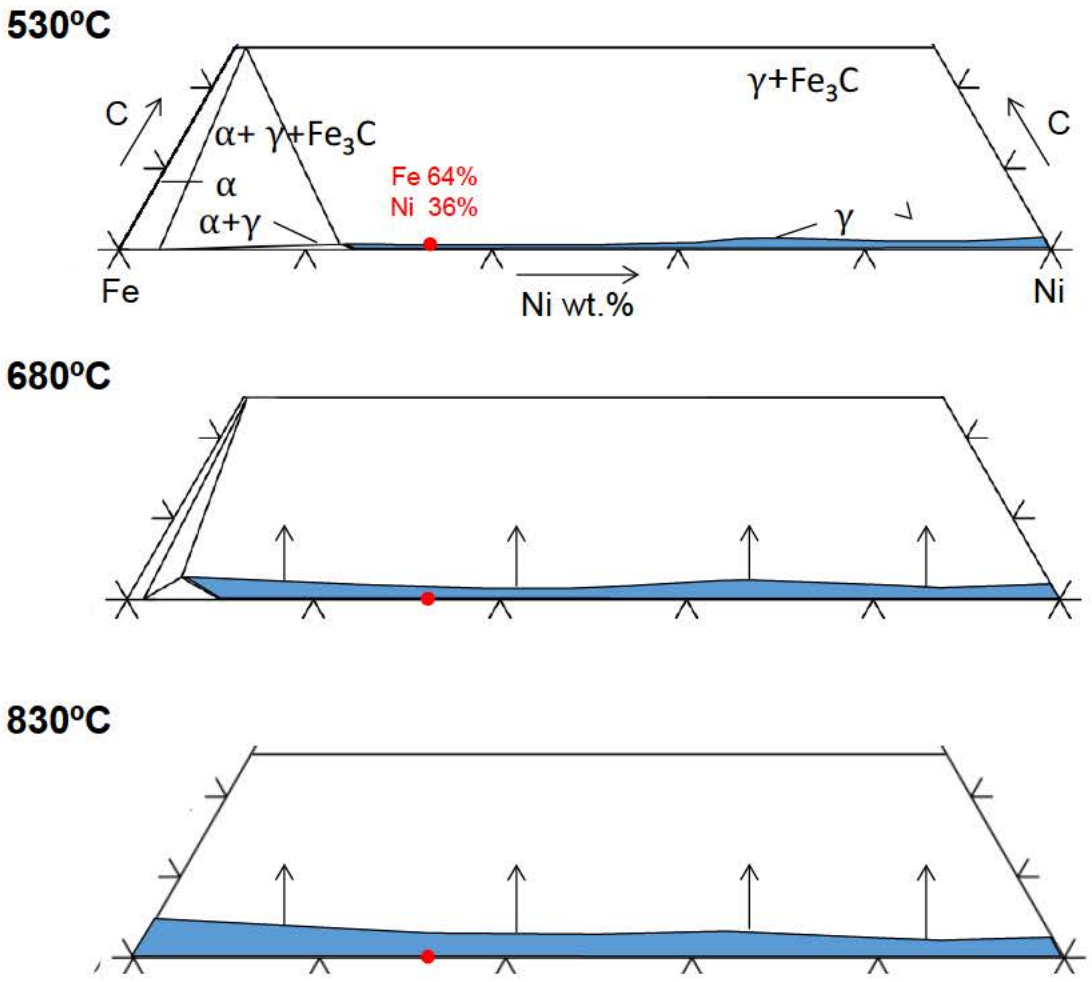

Figure 40 Calculated isothermal sections of iron-nickel-carbon at 530°C, 680°C and 830°C, that indicates the increasing extension of austenite single-phase region to the detriment of cementite (Fe_3C), as the temperature is increased from 530°C to 830°C. Red point indicates the Invar starting composition.

Further work needs to be done to identify whether the cementite is created before or after the fragmentation of the Invar powder at 530°C, and why carbon nanofibers do not extensively grow from metal nanoparticles created at higher temperatures,

which may be explained by the overwhelming ethylene dissociation at these high temperatures that completely covers the metal catalyst.

4.5. Summary

It is well known that nickel and iron are both used to catalytically synthesize carbon nanofibers and nanotubes by CVD. Usually they grow from floating or pre-deposited catalyst nanoparticles of about 1-100 nm in diameter. However, when bulk metals like micrometre-sized powders are used as catalyst to directly synthesize carbon nanostructures, a different behaviour is found since the catalyst surface is continuously affected by bulk evolution.

As we have described in the introduction section, the evolution of these metals depends mainly on carbon solubility, diffusivity and phase transition at CVD conditions. The selection of nickel and Invar ($Fe_{64}Ni_{36}$) highlight the effect of element alloying and carbide transition in $Fe_{64}Ni_{36}$ compared to pure nickel powder, since carbon solubility in both elements are similar in the temperature range [67], [71], and no carbide formation takes place in nickel above 500ºC [68]–[70]. Consequently, pure nickel surfaces are demonstrated to be more stable at CVD conditions (especially at 530ºC and 680ºC) and better withstand the effect of carbon dissolution on its lattice. Contrary, Invar powders suffer fragmentation.

Regarding the results obtained using nickel powders, it is highlighted the very long synthesis times and very high yields obtained at 530ºC, which we explained as following; firstly, the nickel particles evolve under CVD conditions to achieve a polyhedral morphology that allows the multi-armed growth mechanism. This growth mechanism leads to some regions of the nickel surface exposed to gas, which can continuously reach the surface of the nickel particle. Secondly, as the nickel acts as a single-element catalyst, unwanted processes like carbon diffusion through grain boundaries and subsequent fragmentation of catalyst are diminished, so the catalyst life is extended. As a consequence, we obtained a very high ratio of carbon fibres mass over catalyst mass, of 43 after 240 minutes and 400 after minutes. Regarding the results obtained using Invar powders, we obtained a wide variety of carbon nanofibers, nanotubes and nanocoils at 530ºC resulting in a high yield of 30 after 240 minutes. We have shown that the production of carbon nanofibres takes place

after Invar surface fragmentation, which is an advantageous process by which nanometric particles are created, in comparison to nickel powders.

Interestingly, the behaviour of nickel and Invar powders is very similar at 830ºC, where surface fragmentation and production of metal-graphite core-shell nanoparticles up to 1 μm are extensively created in both cases. The convergence on both mechanisms is most likely based on an enhancement of carbon solubility and bulk diffusivity on both metals, which give rise to carbon inward growth and break-up following the metal dusting mechanisms.

Further studies involving the use of other pure or alloyed metal powder as a catalyst for the synthesis of carbon nanostructures by CVD can be carried out. As a parallel research line, the impressive high yield of octopus-like structures make them an interesting low-cost filler for the mechanical reinforcement of composite materials, as currently investigated with nanotubes or carbon nanofibers. Other interesting application would be the exploitation of the magnetic nature of graphite-metal nanoparticles obtained at high temperature, whose biocompatibility is increased by the graphite shell isolation.

5

Synthesis of CNT arrays and carbon thin films on stainless steel foils

5.1. Introduction

The comparison between pure nickel and Invar ($Fe_{64}Ni_{36}$) powders as catalyst presented in the previous chapter represents a good example of how metal alloying affects the interaction mechanism with carburizing atmospheres at CVD conditions. Here, the results obtained when using a highly alloyed and commercially available stainless steel foil as catalyst for the direct synthesis of CNTs arrays and carbon thin films are presented.

As reviewed in the introduction section, there are several studies demonstrating the direct synthesis of CNTs on stainless steel foils [128]–[142]. However, these studies focused on the characterization of the grown CNTs or on the demonstration of proof-of-concepts for different applications, and there is a lack of understanding the surface mechanism interaction between the highly alloyed catalyst and CVD atmospheres.

This chapter shows the evolution of stainless steel foils during the whole CVD process in terms of surface composition and microstructure, which played a critical role in the growth of CNTs. Interestingly, a carbon thin film of about 100 nm thick is simultaneously growing below and connected to the CNTs array. This structure can be isolated from the stainless steel after growth, which represents an interesting building block for energy related applications. The results presented in this chapter have been published in a scientific article [141] and presented in two International Conference talks [182], [183].

5.2. Experimental procedure

5.2.1. Chemical vapor deposition

A stainless steel foil type 304 (25-µm thick, Metall-Folien GmbH) was used as catalyst for the direct synthesis of vertically aligned CNTs synthesis by chemical vapor deposition. The composition of the foil was obtained by using energy-dispersive X-ray spectroscopy (**Table 5**). The pristine stainless steel foil was cut into pieces approximately 20 × 10 mm. To clean the foil, it was dipped in ethanol and dried in air. The stainless steel foil was oxidized at 500ºC for 30 minutes in a muffle furnace before the CVD process.

Table 5. Stainless steel 304 foil composition measured by energy-dispersive X-ray spectroscopy (% atomic).

Fe	Cr	Ni	Mn	Si
69,104 ± 0.61	20.434 ± 0.25	7.896 ± 0.18	0.728 ± 0.11	1.112 ± 0.07

The oxidized stainless steel foil was placed in the middle of a quartz tube (22-mm diameter), positioned in a horizontal tube furnace (Nabetherm, R50/250/12). Once the continuous reactor was sealed, all the lines connected to the system were flushed for 10 minutes followed by 10 additional minutes of argon to displace trapped air from the system. The furnace was ramped to synthesis temperature with 100/400 sccm Ar/H_2 flowing, keeping the sample outside the heating zone. Several synthesis temperatures (from 716ºC to 830ºC) were analysed. Once the required temperature was reached and stabilized, the furnace was rapidly moved (*ca.* 3 seconds) until the sample was located in the middle of the heating zone. The stainless steel annealing step under reducing atmosphere (100/400 sccm Ar/H_2) took place for 10 minutes, starting at room temperature. During this "fast heating", the heating rate started at about 500ºC/minute, as measured by a thermocouple placed outside the quartz reactor, below the sample. After the stainless steel annealing step, the reactant mixture of $Ar/H_2/C_2H_4$ (100/400/100 sccm) was introduced to allow the synthesis to proceed over 10 minutes. After ten minutes, the furnace was moved back away from the sample to allow a rapidly cool down to room temperature. During the cool-down, Ar was flushed to purge any reactive gases of the system.

5.2.2. Characterization of carbon deposits and stainless steel surface

Vertically aligned CNTs and graphite thin films were analysed by using scanning electron microscopy (SEM, EVO MA15, Zeiss) and transmission electron microscopy (TEM, JEOL JEM 3000F). CNTs were removed from the stainless steel surface by cleaning a piece in an ultrasonic bath with isopropanol. CNTs/isopropanol solution was analysed afterwards by TEM. Amorphous carbon thin films were gently removed by acid etching these free-of-CNT foils (copper etchant, Sigma-Aldrich). For the high temperature synthesis conditions (780–830ºC), the substrates were not easily dissolved in the acid, thus tip sonication was applied on these samples to remove the amorphous carbon thin films. A drop of both solutions was carefully deposited on TEM copper mesh (Ted Pella, inc). EDS analysis was also performed to obtain the composition of the different samples.

The as-synthesized samples were analysed by using Raman spectrometry (Jasco, NRS-5100). The spectra were recorded directly on the stainless steel foil after synthesis and from free-of-CNTs substrates, as well as from all the residues from CNTs removal and acid attack. Three measurements for each sample were recorded using a Nd:YAG green laser (534 nm, d=4000 μm). Spectra were obtained for 2 × 20 s exposure over a range of 1000–2750 cm^{-1}. The effective laser power was 6 mW.

Surface chemical analyses were carried out by means of X-ray photoelectron spectroscopy (XPS) by using a PHI 5500 instrument (PERKIN ELMER, Eden Prairie, Minnesota, USA) with a monochromatic aluminium Kα (1486.6 eV) X-ray source. Chemical species present on the surface were identified by using survey scans over a wide range of binding energies (1–1100 eV). Determination of the chemical state of each element is possible by performing narrow scans with high energy resolution in the characteristic binding energy ranges of the elements of interest - in this case iron, chromium, carbon, oxygen, silicon, manganese and nickel. Surface composition was estimated by curve fitting the characteristics peaks and converting their intensity into apparent atomic concentration, using standard relative sensitivity factors [20]. Depth profiles were obtained by sputtering the analysed surface with Ar^+ ions to controlled depths and analysing the etched surface. The etching rate was calibrated by using flat oxidized tantalum foil with the known

oxide thickness. Etch depth is presented in tantalum oxide units that are close to the etching behaviour of metallic oxides of interest [184]. XPS analysis were carried out in collaboration with Dr. Raquel Oro (Chalmers University).

Surface phases were also analysed by using an X-ray diffractometer (XRD, PANalytical model X'Pert PRO MRD) equipped with a copper Ka source (λ = 0.154 nm). Grazing incident (at $\theta = 1^{o}$) experiments were carried out in a 2θ-range from 10 – 100º, with step size of 0.04º and 3 seconds per step was used, and 45kV and 40 mA. XRD analysis were carried out in collaboration with Dr. Ignacion Carabias (CAI de Difracción de Rayos X, Universidad Complutense de Madrid). The diffractograms obtained were compared with patterns contained in the database PCPDFWIN and thereby the characteristic peaks of each phase were identified with: martensite 00-044-1293, austenite 00-031-0619, ferrite 00-037-0474 and CrC 03-05-0082.

Finally, microstructural characterization of the substrate cross-section was carried out at the different steps of the process. For these characterizations, the samples were embedded in resin and mechanically polished to surface mirror finish, cleaned in an ultrasonic bath, and chemically etched (30 seconds in 3 HCl/1 HNO_3 vol.). A thin layer of gold (1 nm) was deposited by sputtering to analyse the sample by SEM (EVO MA15, Zeiss).

5.3. Results

5.3.1. Synthesis of CNT arrays and carbon thin films

CNTs arrays were obtained after synthesis on oxidized stainless steel at a low temperature range between 716ºC–780ºC (SEM image on **Figure 41**a), whose length remained stable at about 4 ± 2 μm, regardless the stainless steel annealing time (10 and 20 minutes). Contrary, no CNTs were detected by SEM at a high temperature range between 780-830ºC. Transmission electron microscopy studies showed that the CNTs arrays were formed by multiwalled CNTs of 20 ± 10 walls (**Figure 41**b), showing several defects in the continuity along the graphite layers. Metal seeds with composition of about Fe/Ni = 95/5 inside the CNTs were also detected by TEM, both on their tips and along their length.

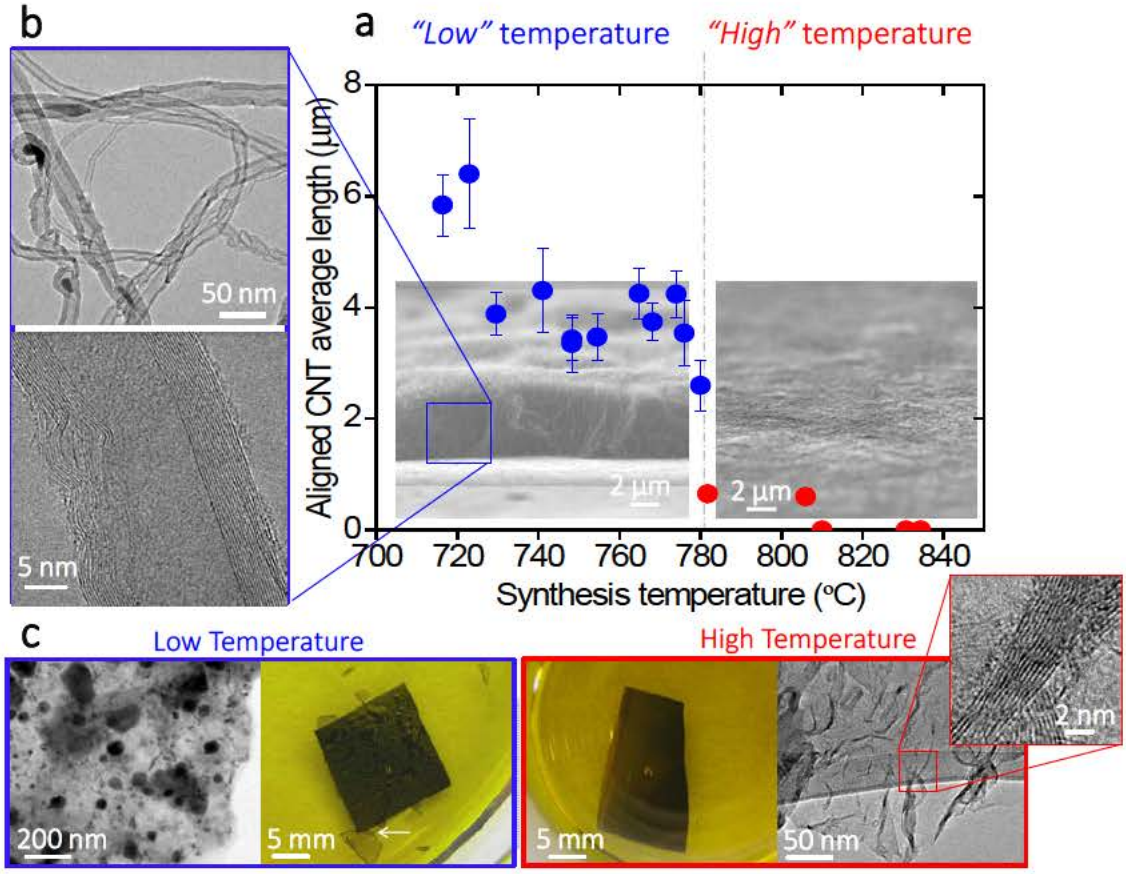

Figure 41. Carbon nanostructures synthesized on stainless steel. Multiwall CNTs arrays were only obtained at low temperatures (716–780°C) (a,b). Acid etching of the low temperature samples easily removed an amorphous carbon thin films (white arrow on c), which were filled with iron-chromium-manganese nanoparticles as detected by EDS-TEM. Contrary, the amorphous carbon thin film on the high-temperature samples was a free of nanoparticles.

Very interestingly, a simultaneous deposition of a carbon thin film below the CNT array was also detected. We identified and isolated it by firstly removing the CNTs arrays (sonication bath) and dissolving the stainless steel in an acid etching bath (**Figure 41**c). This amorphous carbon thin film is a graphene-like thin film formed by graphite nanocrystals, amorphous carbon, and chromium-iron-manganese nanoparticles. During synthesis at a higher temperature range (780-830°C), a similar amorphous carbon film was obtained, however in this case it was free of carbides or metallic nanoparticles (**Figure 41**c). We also found some residual short CNTs up to 1 µm in these samples. The Raman spectra obtained for all the samples were similar in terms of peaks position and intensity, even for the substrates treated

at higher temperature which did not produce vertically aligned CNTs forests (**Figure 42**).

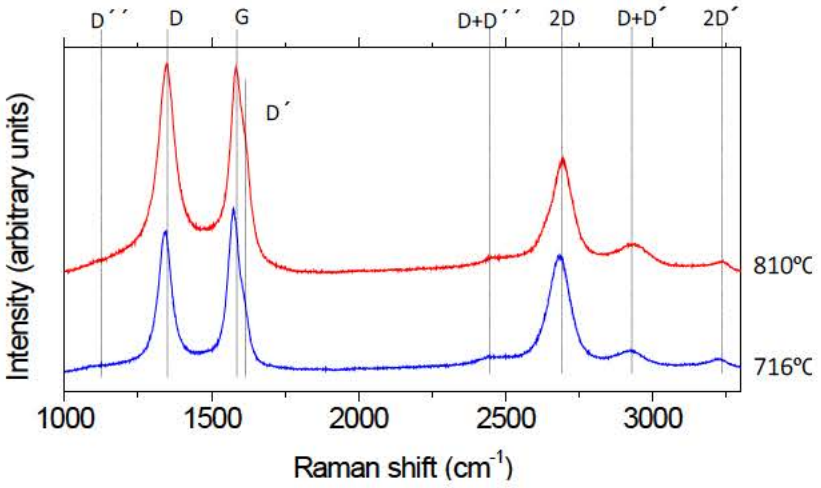

Figure 42. Raman spectra of the as-synthesized samples at different temperatures. Vertically aligned CNTs synthesized at 716°C and carbon deposit synthesized at 810°C.

5.3.2. Temperature effect on stainless steel

A similar study as that carried out with the nickel-iron powder catalysts is presented here, consisting on the identification of possible phase transitions and surface composition of the stainless steel catalyst during the whole process.

Surface phase transitions analysis by XRD. Compared to powders, where XRD analysis is carried out in the whole micrometre-sized particle (bulk and surface), the use of stainless steel in a foil shape enabled to perform surface analysis, which is more adequate to study the surface reactions involved in the synthesis of CNTs. Thus, we have used a grazing incidence X-Ray configuration, with angles of 1° which results in penetration depth of about 0.164 μm in the stainless steel foil.

XRD analysis (**Figure 43**) demonstrates that the as-received stainless steel (AR) is mainly composed of martensite, austenite and an iron-nickel rich phase, and that the as-oxidized stainless steel (AO) presents an enriched austenitic microstructure. This is an expected result, since the fabrication process of stainless steel foils produces a severe plastic deformation at room temperature that produced the martensitic microstructure [185], and due to the thermal treatments, the austenitic microstructure can be partially recovered as it happened after oxidation, and to a

greater extent after synthesis at 716°C. The synthesis at 830°C led to formation of carbides in the surface, most likely chromium carbides [186], as shown in the corresponding spectra.

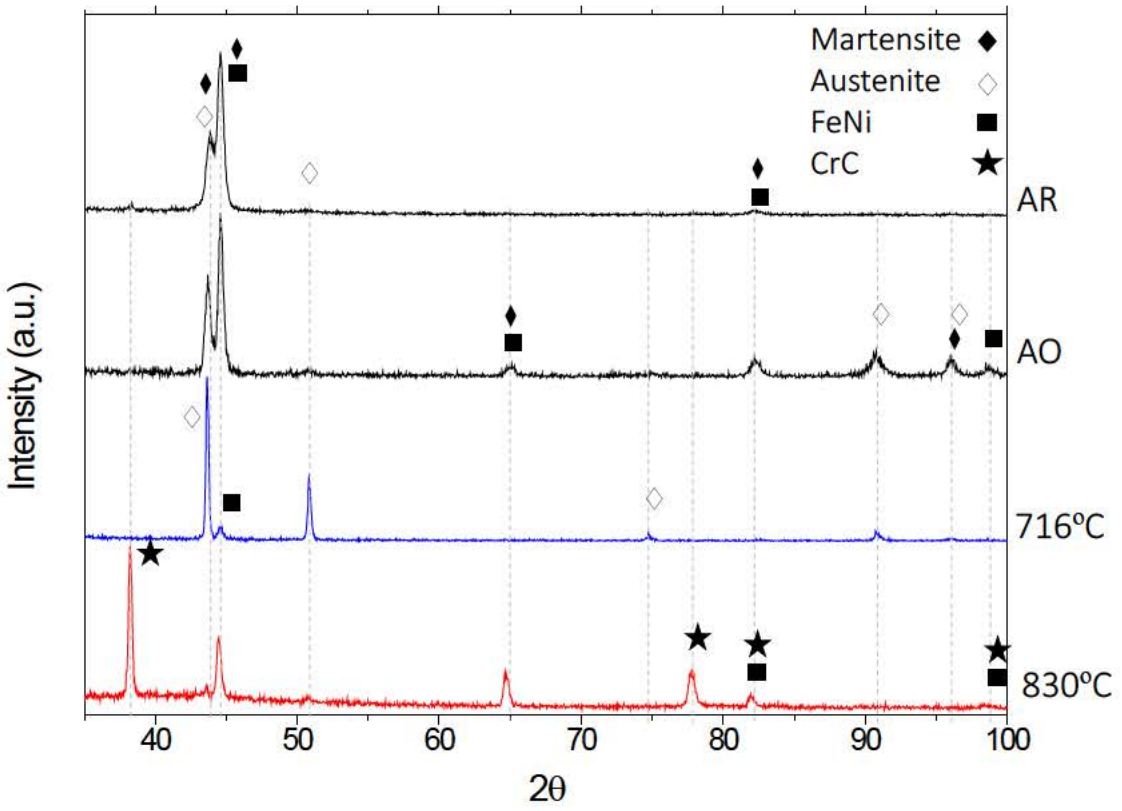

Figure 43. X-ray diffraction spectra of the stainless steel foil at different conditions. The as-received stainless steel (AR) showed a martensitic microstructure, likely produced by deformation by cold working in the fabrication process. Partial martensitic to austenitic transformation took place after oxidation, annealing and synthesis at "low" temperature (716°C), while other phases like chromium carbides were formed at "high" temperature (830°C). In this sample, other manganese-oxygen-chromium-silicon compounds were proposed by the identification software.

During the XRD identification of as-synthesized sample at 830°C, other carbides containing manganese and/or silicon where proposed by the identification software. In this regard, a variety of manganese-oxygen-chromium-silicon compounds (restricted by the stainless steel initial composition) like carbides, oxides and spinels are likely to be produced during the CVD, however the very low counts acquired in the analysis due to the grazing incidence configuration did not allow to an unequivocally identification.

Surface composition by XPS. The limitations of XRD analysis and the identification of surface compounds candidates motivated a deeper compositional analysis using XPS. With this technique the chemical composition of the first 50 nm of the surface of the stainless steel is quantified. We analysed all the states along the process as in the XRD section, but we included the as-annealed state before synthesis (716ºC and 830ºC), thus we analysed i) as-received state, ii) as-oxidized (500ºC), iii and iv) as-annealed (716ºC and 830ºC) and v and vi) as-synthesized (716ºC and 830ºC).

The analysis focuses on iron and chromium, both in oxidized state (cationic species) and metallic state, because both are the more abundant elements in the stainless steel, and iron the needed one to catalyse the growth of CNTs.

i) As-received stainless steel. As expected, the as-received stainless steel surface present a thin native oxide layer that is mainly composed of iron and chromium oxides as extracted from cationic iron and chromium and from that of oxygen signals ($Fe_{cations}/Cr_{cations} \approx 0.35$ at 3 nm, **Figure 44**). Iron in the metallic state within this native oxide layer reached 15 at.% at 3 nm. Also, total nickel signal is about 2 at.%, and manganese and silicon up to 3 at.% and 4 at.% respectively. Manganese and silicon accumulates in the surface, most likely during fabrication, since their nominal composition are 0.72 at.% and 1.11 at.%. In summary, the surface of the stainless steel at as-received state is mainly composed by iron and chromium oxides.

ii) As-oxidized stainless steel. When oxidation treatment was performed, the oxide layer became thicker (oxygen signal) due to oxidation of metallic iron and chromium, thus metallic iron signals decreased down to 5 at.%. Similar behaviour is found on chromium, and a strong increment of iron cations up to $Fe_{cations}/Cr_{cations} \approx 6$ is quantified. In summary, the oxide layer became thicker and enriched with iron cations upon oxidation treatment.

iii) As-annealed (716ºC). The annealing treatment at low temperature (716ºC) resulted in the reduction of iron cations to metallic state with a slight increase up to 6 at.% at 3 nm. Contrary, chromium cations did not reduced but increased in the surface, since chromium oxides are stable under these conditions [187], resulting in a $Fe_{cations}/Cr_{cations} \approx 0.3$.

iv) As-annealed (830°C). High temperature annealing (830°C) led to a significant decrease of metallic iron at 3 nm to 0.6 at.% and a very low ratio $Fe_{cations}/Cr_{cations} \approx 0.12$. Also at this condition the surface is enriched with Mn. In summary, iron, which is the element needed to catalyse the growth of CNTs, is buried below a very stable layer of chromium oxide and other elements like manganese. This very low content of iron in the surface explains the absence of CNT at high temperature.

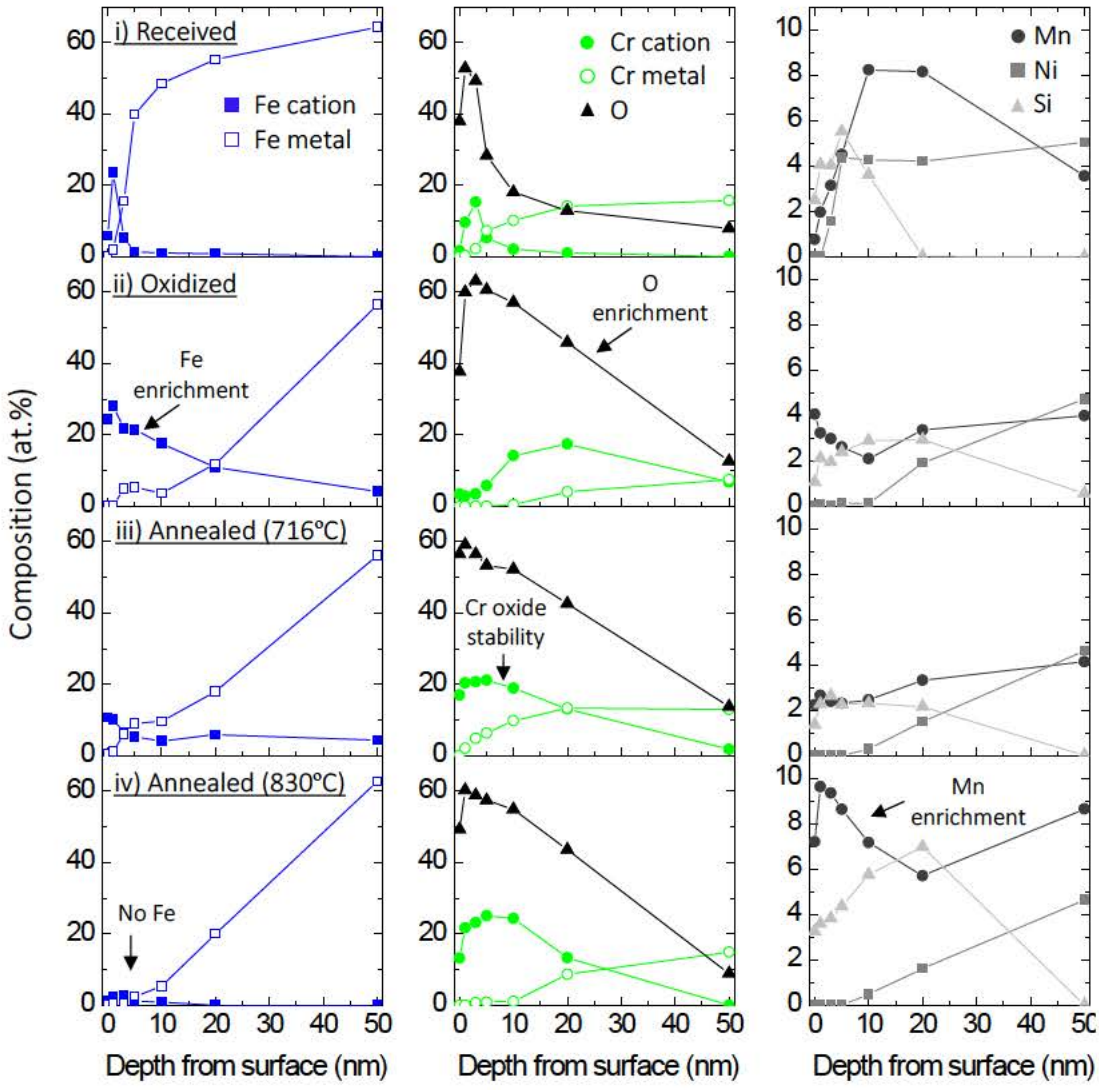

Figure 44. Surface composition profile of stainless steel analysed by XPS before synthesis. i) As-received stainless steel surface is mainly composed by iron and chromium oxides, and showed 15 at.% metallic iron at 3 nm from its surface. ii) Oxidation produced a thicker iron-enriched oxide layer (cations signals) so metallic iron decreased to 5 at.% 3 nm from the surface. iii) Annealing step at 716°C affected the iron cations more intensely than chromium cations, so we found about 6 at.% of metallic iron at 3 nm. iv) Annealing step at 830°C significantly decreased the amount of metallic iron at 3 nm to 0.6 at.%, due to an enhancement of chromium oxides and Mn.

v) As-synthesized (716ºC and 830ºC). After the annealing steps at different temperatures (**Figure 45**), the synthesis process takes place with a stabilized temperature, so synthesis at 716ºC starts after annealing at 716ºC, and the same with other temperatures. Regarding the composition of the surface after the synthesis step at 716ºC (**Figure 45**) and once the CNT array were removed, it is found a 0.4 at.% of metallic iron and a ratio of $Fe_{cations}/Cr_{cations} \approx 0.16$ at 3 nm. In other words, the chromium oxide layer remains stable with a very similar profile as before synthesis (annealing at 716ºC in **Figure 44**). In terms of carbon incorporation into the substrate after the synthesis step, a small accumulation was detected at low temperature (26 at.% at 716ºC). When the synthesis was conducted at higher temperatures (830ºC), a significant increase of carbon up to 75 at.% was detected. As shown, carbon penetrated into the bulk, reaching values of about 26 at.% at a depth of 50 nm (**Figure 45**). Due to the increase of an external element (carbon), the concentration of other elements decreased, however both chromium in oxidized and metallic state remains in the surface as well as manganese and silicon. These results reveal again the greater stability of chromium oxides and manganese and silicon compounds, and also is in agreement with the XRD identification software where these candidates were proposed.

Comments on stability of elements and the "internal-getter" effect. In this chapter the reactivity of an oxidized stainless steel under CVD conditions is analysed. Despite we focus on iron due to its well-known ability to catalyse the growth of CNTs, oxidized stainless steel at CVD conditions includes up to 7 elements (iron, chromium, nickel, manganese, silicon, oxygen and carbon), all of them that might be interacting with each other. Thus, this is a more complex situation compared to the use of pure nickel and $Fe_{64}Ni_{36}$ powders as catalyst without any oxidation.

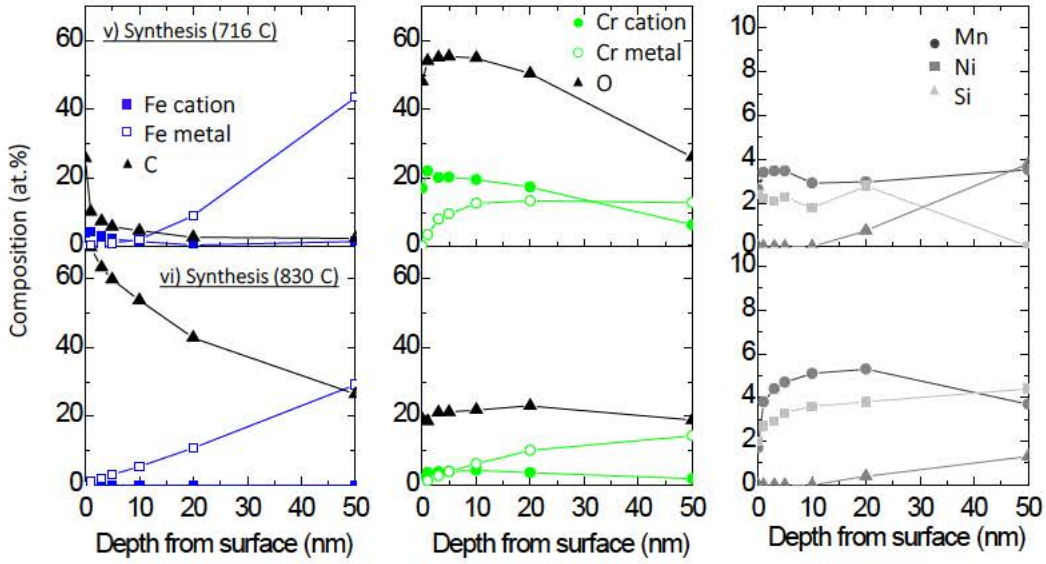

Figure 45. Surface composition profile of stainless steel analysed by XPS after synthesis at 716°C (v), which indicates the predominance of chromium cations on the surface. A short accumulation of carbon occurred after synthesis at 716°C, however a significant increase of carbon incorporation into the substrate occurred at 830°C (vi). At this temperature, both chromium in oxidized and metallic state remains in the surface as well as manganese and Si. This results reveal again the greater stability of chromium oxides and manganese and silicon compounds, at the expense of the needed iron catalyst.

XPS studies showed a very low concentration of iron in the surface, especially after annealing at high temperatures (830°C), which is explained by the higher stability of chromium oxides as well as other minor elements that accumulates in the surface with much higher concentrations than the nominal. The higher stability of some elements used in metallurgy is explained with the Ellingham diagram in **Figure 46**a, which situates the stability of some possible oxides as a function of Gibbs free energy (ΔG) and temperature, being the lower ΔG the more stable. In agreement with our XPS results, chromium oxides as well as manganese-silicon-oxygen compounds are more stable that iron at a given conditions.

In this regard, the different reactions taking place depends on temperature and partial pressures of gases involved. The **Figure 46**b represents a comparison of the oxidation and reduction reactions of different elements taking into account their relative stability. As it can be clearly observed, there is always a range of temperature and partial pressure of gases (grey area) where the conditions can be reducing for iron and oxidizing for chromium, manganese and silicon. With these conditions, a selective oxidation of chromium, manganese and silicon can take place

simultaneously to the reduction of iron [188]–[190]. This phenomena is known as **internal-getter effect**, by which the reduction of the less stable oxides leads to oxidation of the elements with higher affinity to oxygen (any of the lines that are below the iron oxide in the Ellingham diagram in **Figure 46**b). This phenomena explains the accumulation of chromium oxide and manganese after annealing (**Figure 44**), especially at 830°C.

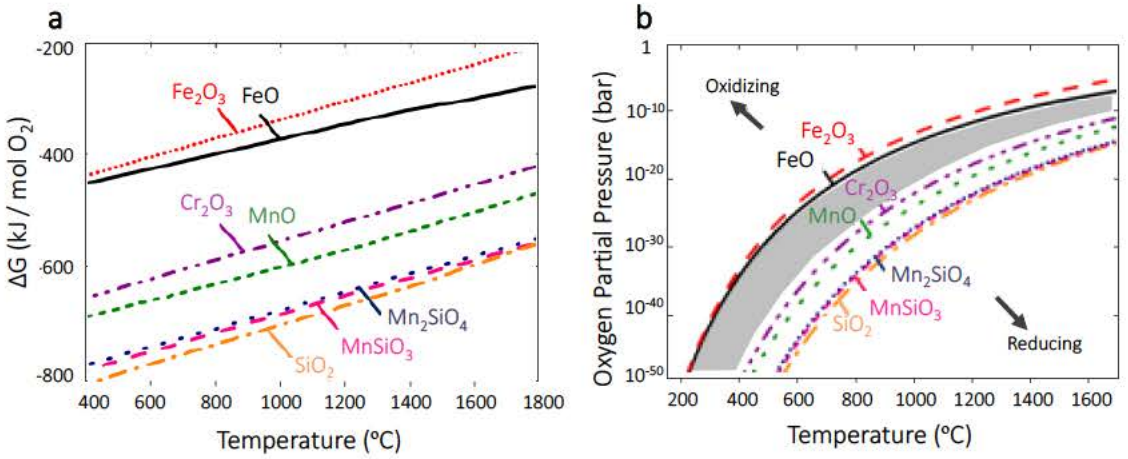

Figure 46 Ellingham diagram for some of the possible oxides present in the stainless steel studied, calculated with HSC Chemistry HSC 4.1 as extracted from reference [188]. As shown in the grey area of figure b, there is always a range of temperature and partial pressure of gases where the conditions can be reducing for iron and oxidizing for chromium, manganese and silicon.

Cross-sectional microstructural analysis. Finally, an analysis of the substrate cross-section was conducted to identify the depth of the stainless steel evolution (**Figure 47**). The pristine stainless steel shows the typical deformed and acicular grain morphology of martensite, in agreement with the X-ray diffraction results. The black cavities corresponded to the porosity created by manganese-chromium-oxygen inclusions (56.7 at.% of O, 17.4 at.% of chromium and 11.62 at.% of manganese). We also observed that this martensitic microstructure remained after the oxidation step. Nevertheless, a recrystallization process took place at about 750°C and the grain size increased with the synthesis temperature. As expected from the X-ray diffraction results, a microstructure with chromium carbides spread throughout the cross-section is observed at about 810°C.

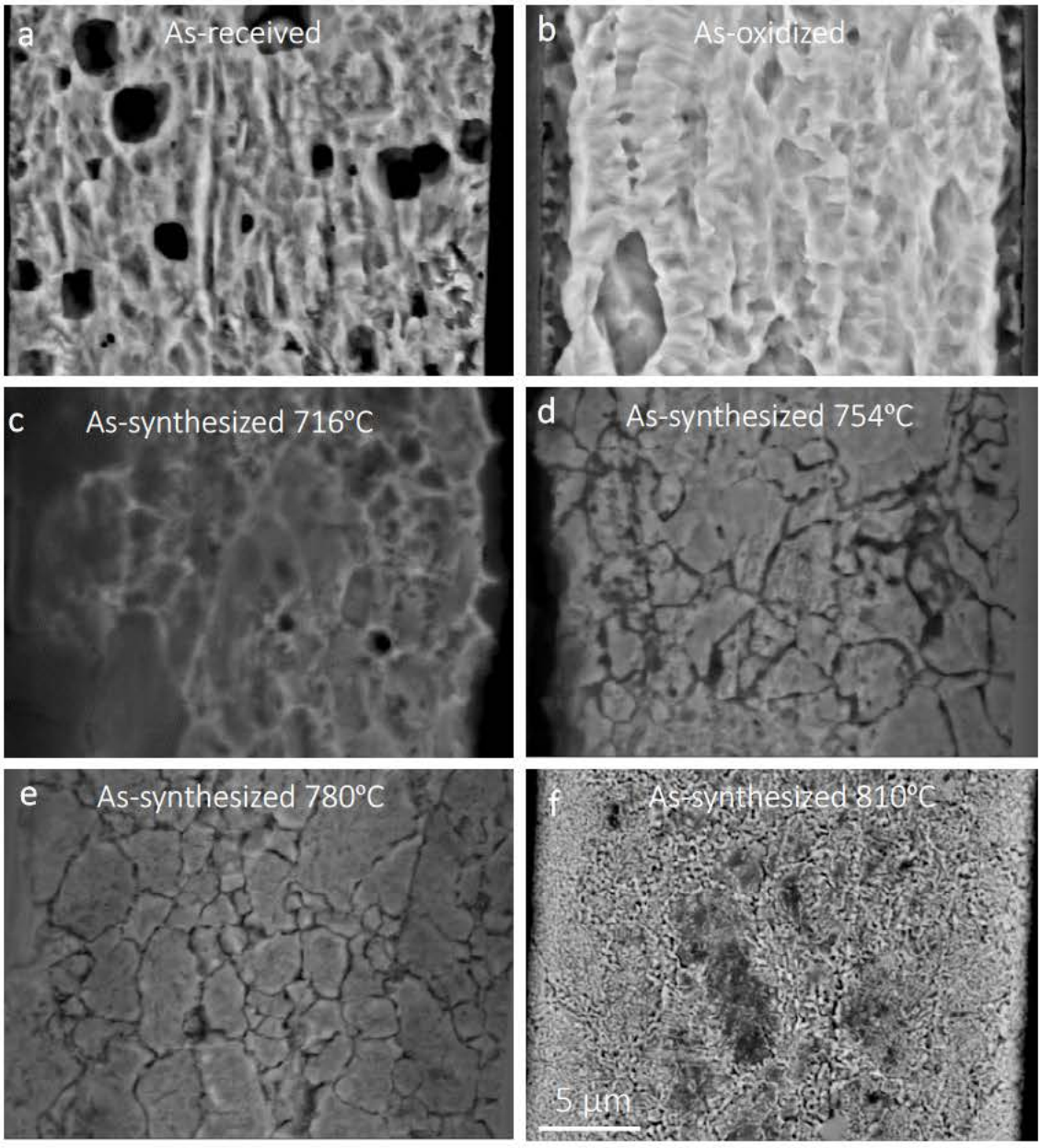

Figure 47. Microstructure evolution of a stainless steel. Stainless steel cross-section from as-received to as-synthesized at 810°C. Acicular grains corresponding to martensite microstructure were observed in as-received (a) and as-oxidized (b) samples. An increase of the grain size was detected after synthesis at 754°C and 780°C (d, e). Synthesis at 810°C led to big grains with a pronounced chromium carbide formation across the whole cross-section (f).

5.4. Discussion

The stainless steel foils evolves during the different steps (oxidation, annealing and synthesis), which will affect the CNT growth process. The stainless steel oxidation treatment creates an iron-richer and thicker oxide layer than the thin native oxide of the as-received steel (**Figure 48**a), as demonstrated by XPS. Here the difference between the low and high temperature cycles is highlighted, as it has been done along this chapter.

During the low temperature annealing cycle (**Figure 48**b), metallic iron is partially recovered from the oxide layer, giving rise to CNT arrays during the synthesis step. Without this oxidation pretreatment, we obtained fuzzy and short CNTs instead or highly ordered arrays. What is believed is that the oxidation//low temperature reduction treatment create finely dispersed metallic iron nanoparticles on the stainless steel surface [131]. Although iron at metallic state seems not to be strictly needed for the synthesis of CNTs [191], the production of vertically aligned CNTs from oxidized/low temperature annealed samples may be enabled by the high density of catalytic particles present in the surface, which enables a collaborative growth mode perpendicular to the surface [192].

On the other hand, the amount of iron in the surface (both in metallic and cationic state) is significantly lower for the samples annealed at high temperatures (**Figure 48**c). In this regard, chromium and other elements like manganese and silicon remain very stable during annealing and are accumulated in the surface at the expense of iron. Probably, because of this low density of iron, CNTs arrays did not grow during synthesis, but a wide variety of carbides, oxides and spinels are produced from the reaction of carbon and the stable elements (chromium, manganese, and silicon). Also, a recrystallization process at high temperature which creates grain boundaries was detected that, together with the enhancement of carbon solubility in pure bulk iron (*ca.* 0.1 at.% to 4 at.% from 700ºC to 800ºC) [62], resulted in a carbon diffusion into the stainless steel as detected by XPS [193].

A simultaneous growth of CNT arrays and a carbon thin film at low temperatures was detected, which interestingly are physically connected and can be isolated as shown in **Figure 48**d. This image and the finding that the carbon thin film is filled

with nanoparticles (inset in **Figure 48**d) reinforces the hypothesis of a first deposition of a carbon film, which breaks the surface creating nanoparticles as described in the metal dusting phenomena [135], [153], [154], [194]. As a result, metal nanoparticles are exposed to gas, on top of which the CNT array can grow. Further work would be needed to confirm this hypothesis.

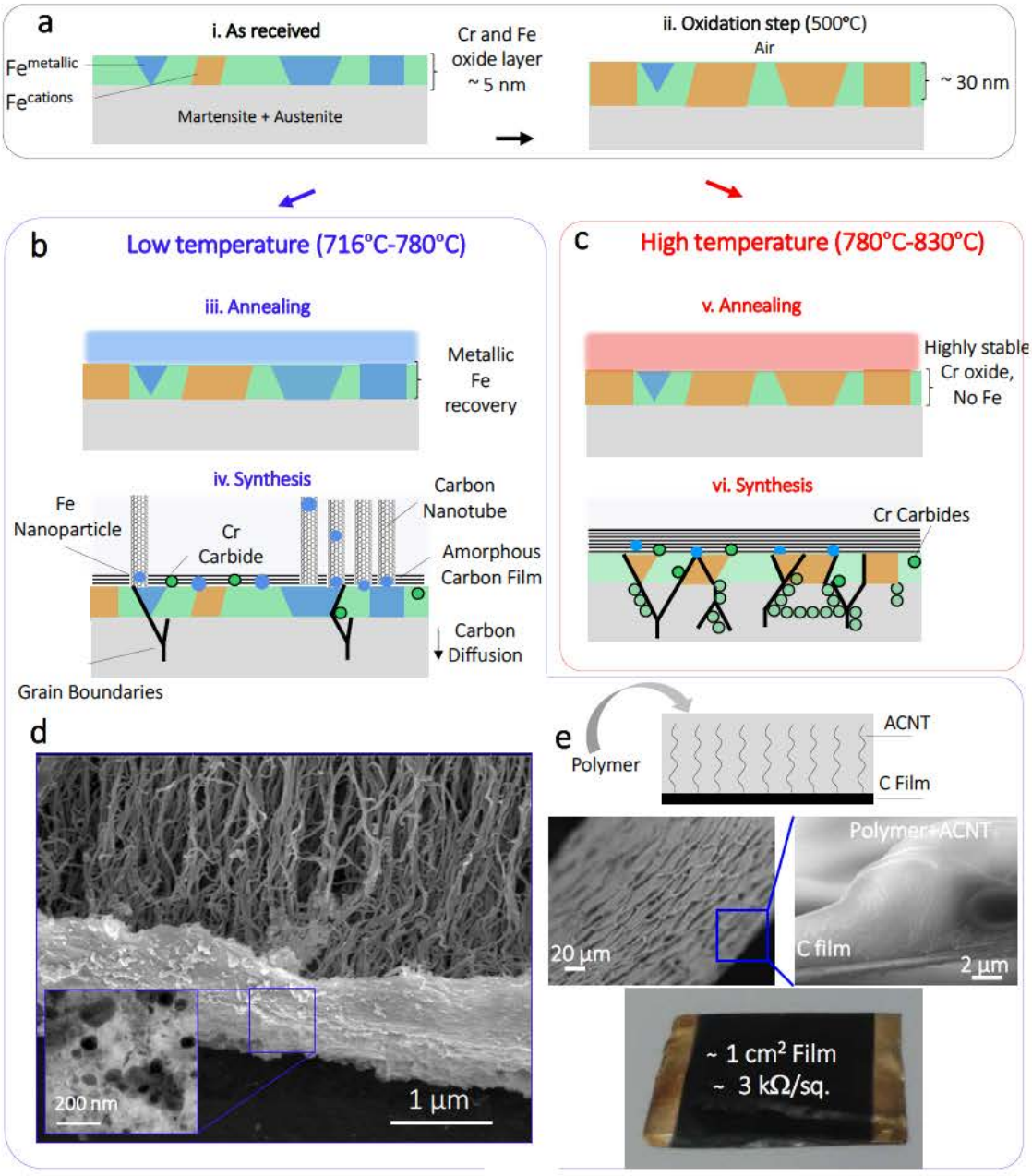

Figure 48. Overview of simultaneous synthesis of CNT array and carbon films on stainless steel catalyst.

Finally, the application of this 3D structure consisting on CNT arrays connected to a carbon thin film is proposed. This physical connection is very advantageous for the effective availability of the CNTs properties, and could be exploited in energy harvesting or catalysis. As a proof-of-concept, we have manufactured a composite material formed by this 3D structure and a polymer, which showed a sheet resistance of about 3 kΩ/□.

5.5. Summary

In summary, vertically aligned carbon nanotubes and amorphous carbon thin films were simultaneously synthesized directly on oxidized stainless steel foils by chemical vapor deposition without adding an external catalyst. A low temperature reduction treatment (716°C–780°C) of the oxidized stainless steel is a convenient pretreatment before chemical vapor deposition to synthesize vertically aligned carbon nanotubes in the oxidized stainless steel. Regardless the temperature used for the chemical vapor deposition synthesis step, an amorphous carbon thin film on the stainless steel surface have been found that can be detached by means of acid etching. However, vertically aligned carbon nanotubes forests were only obtained in the low synthesis temperature range (716°C–780°C), meanwhile no vertically aligned CNTs forests were obtained from synthesis at above approximately 800°C.

Stainless steel evolved during all stages of the process and opens a discussion of the growth mechanism in these low cost and highly alloyed catalysts. In terms of composition, the oxidation step enriches the stainless steel surface with Fe_2O_3 that, in the next low temperature annealing step, partially turns back into metallic iron. As a result a thicker Cr_2O_3 layer is also obtained that is believed to act as a carbon diffusion barrier. It is believed that after this low temperature reduction pretreatment, catalytic active sites on the stainless steel surface are produced [131], that may be responsible of the production of vertically aligned carbon nanotube forests. In this regard, it was found that this is achieved only after low temperature annealing (716-780°C), and nearly no metallic iron is detected in the surface after high temperature reduction. Two important aspects highlight the use of low cost stainless steel foils, which are the absence of a catalyst preparation step for the growth of the nanotube arrays (which generally needs hard-to-scale routes), and the

simultaneous and physically connected growth of the nanotube arrays to the carbon film. The approach presented here may be scalable using continuous systems as recently published in reference [117].

6

Synthesis of carbon thin films on copper foils

6.1. Introduction

In the previous chapters, the influence of alloying in the growth mechanism of carbon structures using pure nickel and Invar ($Fe_{64}Ni_{36}$) powders was studied. Next, the number of elements were increased in a highly alloyed catalyst, a stainless steel foil, which under cCVD conditions resulted in the simultaneous synthesis of CNTs arrays and carbon thin films. In this chapter, which is the last about synthesis by cCVD on metals, the results when using copper foils as catalyst are presented. As explained in the Chapter I, copper shows a very low interaction with carbon compared to iron and nickel, and is widely selected as the catalyst to produce cCVD monolayer graphene.

Despite the potential of graphene films for a wide variety of applications, the large-scale production of atomically thin, continuous and monocrystalline graphene film has not yet been achieved [72], [195]–[198]. Alongside the ongoing work on graphene, the synthesis and use of other carbon nanometer-thick films with lower degrees of crystallinity might relax the requirements of production and manipulation processes such as the highly controlled atmospheres, substrate preconditioning, sample transfer, etc. Such carbon nanometer-thick films have great potential and applicability because its transparency and electrical conductivity, among other interesting properties. In this part of the work, the controlled synthesis of transparent carbon thin films of different thickness in the range of several nanometres, including monolayer graphene, are presented. Some results presented in this chapter have been published in a peer-reviewed publication [199].

6.2. Experimental procedure

6.2.1. Chemical vapor deposition

Commercial copper foils were used as catalyst for the chemical vapor deposition of carbon thin films (100-µm-thick copper foil, 99.8% purity, Sigma Aldrich). The copper foil was cut into rectangles of 22×50 mm^2, dipped in pure ethanol and cleaned by ultrasonication for 10 minutes. For the synthesis of graphene, a high purity copper foil (99,999% Puratronic Alfa Aesar) was used. In this case, copper foils were cleaned using a 2% HNO_3 solution in pure ethanol during 30 seconds and thoroughly cleaned with pure ethanol afterwards [103].

Synthesis of carbon thin films. All the gas lines (argon, H_2, and C_2H_4) connected to the 22-mm diameter quartz tube of the CVD reactor were flushed for 10 minutes, followed by an additional 10 minutes of argon to displace trapped air and other gases from the system. The furnace was then ramped to the synthesis temperature (850ºC) with 1000/20 sccm of Ar/H_2 flowing, while keeping the catalyst outside the heating zone. Once the temperature stabilized, the furnace was rapidly moved (*ca.* 3 seconds) to locate the centre of the heating zone of the furnace around the copper foil. Prior to the last synthesis step, 10 minutes of annealing with different concentrations of Ar/H_2 flow were used (see **Table 6**).

Several synthesis conditions were tested to study the effect of the total gas flow (Q = $Ar + H_2 + C_2H_4$) and the ethylene concentration [C_2H_4] = C_2H_4 / ($Ar + H_2 + C_2H_4$) in the final carbon film thickness. The total flow varied from 140 to 540 sccm and the ethylene concentration from 0.04 to 0.5. The synthesis time was fixed at 5 minutes.

Synthesis of graphene films. The synthesis of monolayer graphene required more diluted ethylene and higher temperature (950ºC). The annealing time was increased up to 20 minutes and different H_2 concentrations were explored during this step (1000/20, 1000/200 and 1000/400 sccm of Ar/H_2.). Synthesis conditions to obtain monolayer graphene are summarized in **Table 7**.

Table 6. Chemical vapor deposition conditions in the synthesis of the carbon thin films. The synthesis step was kept for 5 minutes at 850ºC after 10 minutes of annealing under 1000/20 sccm of Ar/H_2. No more CVD conditions were carried out for total gas flow (Q) of 40 sccm due to technical limitations of our flow controllers.

Q=40sccm		**Q=140sccm**		**Q=340sccm**		**Q=540sccm**	
Ar-H_2-C_2H_4	**C_2H_4**	**Ar-H_2-C_2H_4**	**C_2H_4**	**Ar-H_2-C_2H_4**	**C_2H_4**	**Ar-H_2-C_2H_4**	**C_2H_4**
–	–	120-10-10	0.07	300-20-20	0.06	500-20-20	0.04
–	–	100-20-20	0.14	190-75-75	0.22	420-60-60	0.11
–	–	80-30-30	0.21	140-100-100	0.29	300-120-120	0.22
0-20-20	0.5	0-70-70	0.5	0-170-170	0.5	0-270-270	0.5

Table 7. Chemical vapor deposition conditions in the synthesis of graphene films. A new gas flow controller was installed to control more diluted C_2H_4 concentrations needed for the synthesis of monolayer graphene. The temperature was increased up to 950ºC and synthesis step kept for 5 and 10 minutes for different batches, after 20 minutes of annealing under 1000/20-200-400 sccm of Ar/H_2.

Ar-H_2-C_2H_4 (sccm)	**Time**	**Ar-H_2-C_2H_4 (sccm)**	**Time**
1000-20-0,5	5 and 10 minutes	1000-20-1	5 minutes
1000-200-0,5	5 and 10 minutes	1000-200-1	5 minutes
1000-400-0,5	5 and 10 minutes	1000-400-1	5 minutes

6.2.2. Carbon film thickness and microstructure

As-synthesized samples (carbon film on top of copper foil) were dipped in $FeCl_3$ – HCl copper etching solution (Sigma Aldrich, 667528) to dissolve the copper foil. Once the carbon film was detached in the form of flakes, they were cleaned by replacing the etchant with deionized water and washing several times. The carbon flakes were transferred into a thermal oxide wafer (300 nm SiO_2 on Si), as shown in **Figure 49**. Atomic force microscopy characterization (non-contact mode, Park XE150) was carried out. The images were acquired by non-contact mode using a non-contact cantilever (PPP-NCHR, Park System), with a tip set point of about ~30-40 nm and amplitudes between ~25-45 nm with a scan rate of 0.50 Hz.

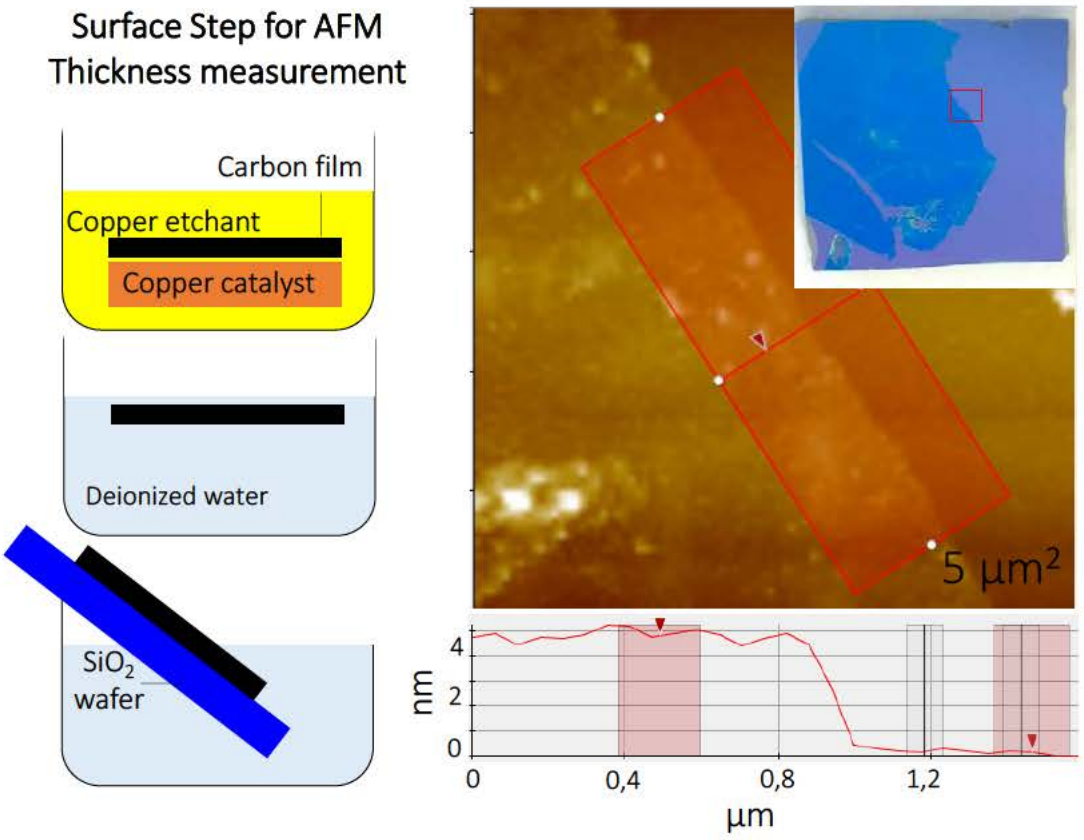

Figure 49 Process followed to measure the thickness of the carbon films. The carbon film/copper foil was dipped in copper etchant. Once the copper foil was completely etched, the carbon film was cleaned with deionized water several times and then "fished" with a SiO_2 wafer. Finally, the thickness of the film was measured by AFM from a stepped surface.

Carbon flakes from three thin carbon films (thickness <15 nm) were transferred onto a copper grid for analysis under a transmission electron microscope (JEOL JEM 3000F). Raman spectra of all the carbon films were collected from silicon wafers (Jasco, NRS-5100). At least three measurements per synthesis condition were taken, using a Nd:YAG green laser (532 nm, aperture: 4000 µm, grating: 1800 l/mm, slit: 200×1000 µm, resolution: 7.42 cm^{-1}), with two accumulations of 20 s exposure over a range of 1000–3250 cm^{-1}. The effective laser power was about 5.3 mW. We compared the Raman spectra of our carbon films with those of a glass-like carbon rod (Gomensoro, N°61248040) and graphene sheet on a silicon wafer (Graphenea). We also analysed the spectra of all the carbon films synthesized within this work. The analysis of the Raman spectra of the carbon films was carried out by fitting the corresponding band of highly disordered carbons as proposed in several articles [200]–[202].

Additional Raman experiment were carried out to ascertain if the layer that is in contact with the copper foil, ("bottom carbon"), has a different Raman spectra than that of the carbon on the top ("top carbon"). The analysis of the top and bottom carbon was carried out as explained in the **Figure 50**. For top carbon analysis, the copper was submerged with the carbon film facing up, so after copper removal and cleaning with deionized water, the remaining carbon film was "fished" with a SiO_2 wafer, with the top carbon facing up. For bottom carbon analysis, the copper was submerged with the carbon film facing down, so following the same procedure, we will have the bottom carbon facing up.

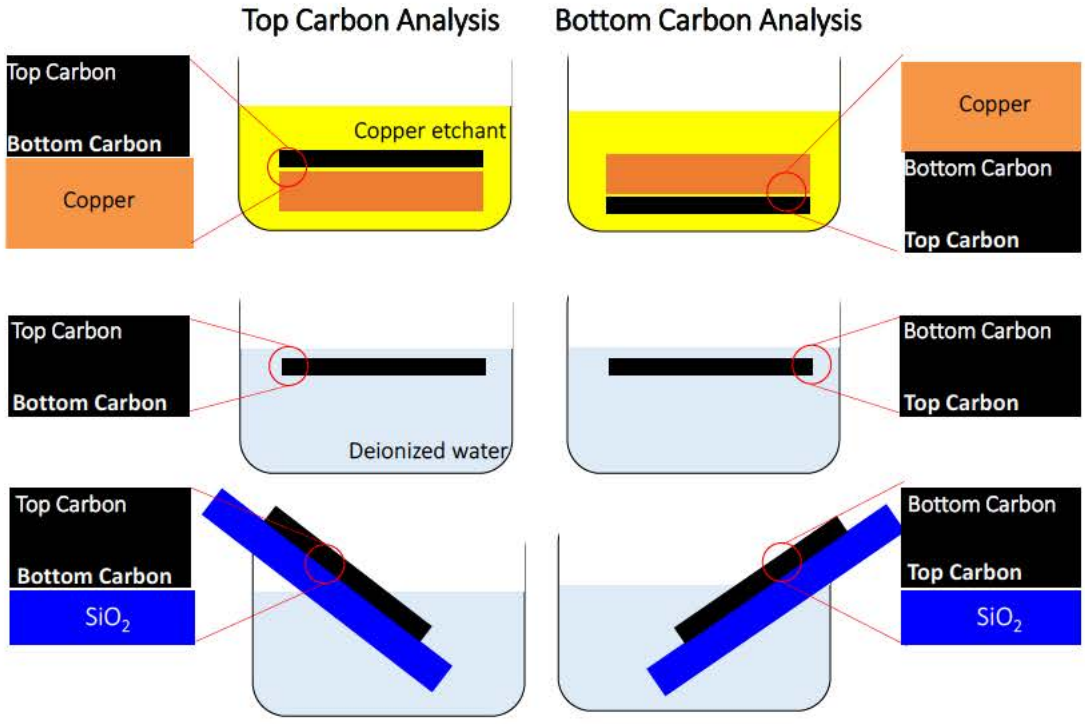

Figure 50 Process followed to prepare samples for Raman analysis. For top carbon analysis, the copper was submerged in a copper etching solution with the carbon film facing up, and for bottom carbon analysis, the copper was submerged with the carbon film facing down.

6.3. Synthesis of glass-like carbon thin films

6.3.1. Thickness control

The thickness of carbon thin films were controlled by carefully selecting the total gas flow rate ($Q=Ar+H_2+C_2H_4$) and ethylene concentration ($[C_2H_4]$) used in CVD. Carbon films from 5–237 nm thick were synthesized on top of the copper foil (**Figure 51**). As expected, the ethylene concentration had a positive effect on the carbon film thickness, which can be clearly observed at a total flow of 140 sccm. However, this dependence on total flow was not so evident at higher total flows (340 and 540 sccm). On the other hand, thinner carbon films can also be obtained by increasing the total flow and keeping a constant ethylene concentration. This effect was clear only ethylene concentration of $[C_2H_4]=0.5$ [203]. Thus, thin films of 5–10 nm were obtained by using highly diluted ethylene and high total flows, meanwhile thick films of about 80 nm were obtained by using highly concentrated ethylene and low total flows.

The resulting carbon film thickness can be explained taking into account the total carbon mass that is supplied during synthesis, which is related to the ethylene concentration $[C_2H_4]$, and the average speed of the gas, which is related to total flow Q. In this regard, the lower the time the hydrocarbon molecules of the decomposed ethylene are in contact with the substrate and the fewer molecules, the thinner the carbon film synthesized on the copper foil. Fitting well with this interpretation, the thin films are obtained at the higher total flows and the lower ethylene concentrations. A simple model was developed that captures the effect of both the $[C_2H_4]$ and Q on the film thickness. A simple relation was found that can be adjusted to our experimental results. The film thickness is proportional to $[C_2H_4]$ and inversely proportional to the average speed <V> of the gas through Q and the area of the CVD tube (A), as follows:

$$\textbf{Carbon film thickness}\ (\text{nm}) = C\ t\ [C_2H_4]\ \langle V\rangle^{-1} = C\ t\ [C_2H_4]\ A\ Q^{-1} \qquad (6.1)$$

where carbon is a proportionality constant, t the synthesis time (5 min), <V>, the average speed of the gas at the entrance of the CVD (at standard conditions), and A the area of the quartz tube (2,2 cm of inner diameter). By adjusting this equation

($C=1{,}020 \cdot 10^{-4}$ cm^2/min^2), it can be observed that the model fits well with our experimental data (**Figure 51**).

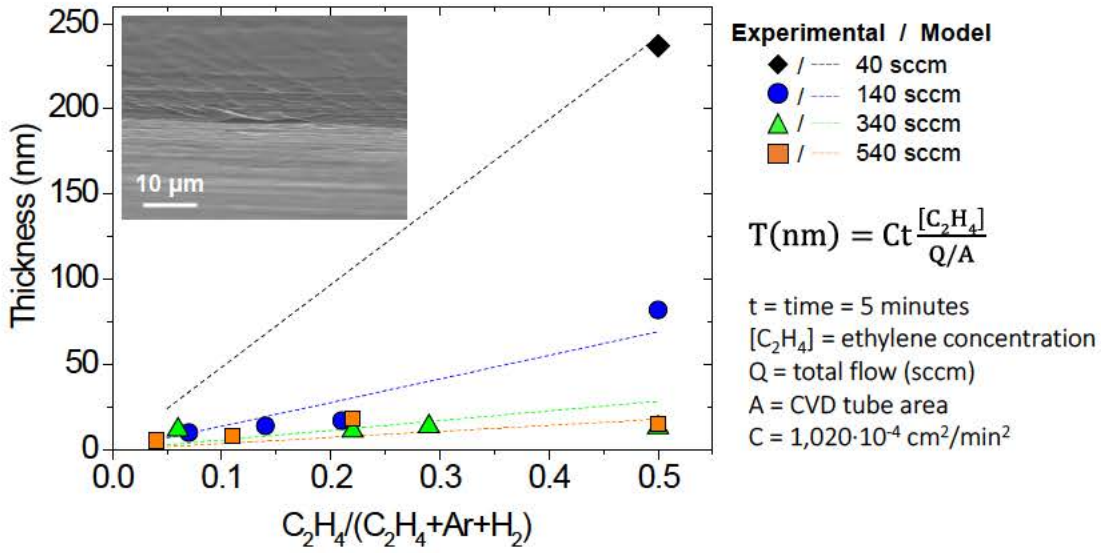

Figure 51 Thickness of carbon films (SEM inset) as a function of CVD parameters (total flow from 40–540 sccm and ethylene concentration from 0.04–0.5). The ethylene concentration had a clear proportional effect on the carbon film thickness at total flows of 140 sccm, but no evident linearity was found at 340 and 540 sccm. The higher the total flow, the thinner the carbon films produced; this effect is especially significant at higher ethylene concentrations. A simple model for the carbon film thickness (T) as a function of the ethylene concentration and the total flow is proposed, which is in agreement with our experimental data.

During CVD experiments of high [C_2H_4], it was found that the carbon deposition process is not only taking place on the copper catalyst placed in the CVD reactor, but also deposits on top of quartz support and on the quartz tube (**Figure 52**).

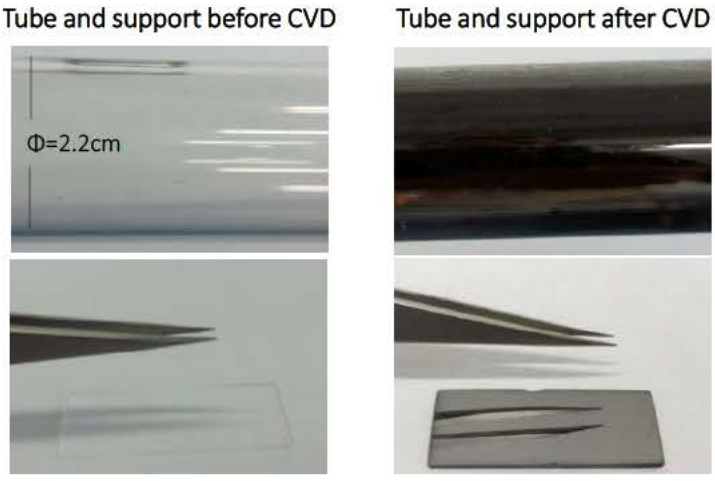

Figure 52 Deposition of carbon on support and tube when using Ar=0 H_2=C_2H_4=20 sccm.

6.3.2. Microstructure determination

The microstructure of the carbon thin films were analysed under a transmission electron microscope **Figure 53**a. Very high magnifications reveals randomly oriented and curved graphitic crystallites within an amorphous carbon matrix (**Figure 53**b, c), as well as semicontinuous graphitic planes up to 5–10 layers similar to those seen in few-layer graphene (Figure 53d). These curved graphene layer fragments resemble the fullerene-like fragments that form glass-like carbons, which are a well-known class of amorphous carbon that shows short range order [31], [32], [204]–[206]. In our case, the curved graphene layer fragments have a maximum size of about 3 nm.

Glass-like forms of carbon can be obtained at different temperatures [31], [206], which results in different crystal lengths. As proposed in reference [32], type-I glass-like carbon are produced below 2000ºC, which consist of randomly distributed curved graphene-layer fragments with open pores, while type-II glass-like carbon are fabricated at higher temperatures and contain longer range and self-assembled fullerene-like spheroids with closed pores. Here, type-I glass-like carbon was obtained, since our film has randomly distributed and open curved graphene-layer fragments within an amorphous matrix.

Raman spectroscopy. Raman spectroscopy was performed to study the crystal structure of our all carbon thin films. The Raman spectra of our 5-nm-thick carbon film was compared to that of a glass-like carbon rod, and that of a graphene sheet (Figure 54a).

The Raman spectra of highly crystalline carbons have two prominent feature, which are the G peak at about 1580 cm^{-1} that corresponds to the bond stretching of sp^2 carbon pairs in both rings and chains, and 2D peak at about 2700 cm^{-1}. This is exemplified in the Raman spectra of graphene in **Figure 54**a. The disorder in the microstructure of graphitic materials is mostly evidenced by the appearance of the D peak at around 1350 cm^{-1}, which corresponds to the breathing modes of sp^2 carbon rings, but also by the G band broadening (due to the emergence of a D´ peak at about 1620 cm^{-1}) and the presence of a D´´ peak at about 1100 cm^{-1}. These first-order phonons may combine, giving rise to second-order peaks at D+D´´ *ca.* 2450 cm^{-1} and

D+D′ *ca.* 2.950 cm^{-1}. D and D′ overtones give rise to 2D and 2D′ peaks (2700 cm^{-1} and 3250 cm^{-1}), which broadens and disappears respectively in disordered graphites [166], [200], [207]–[209].

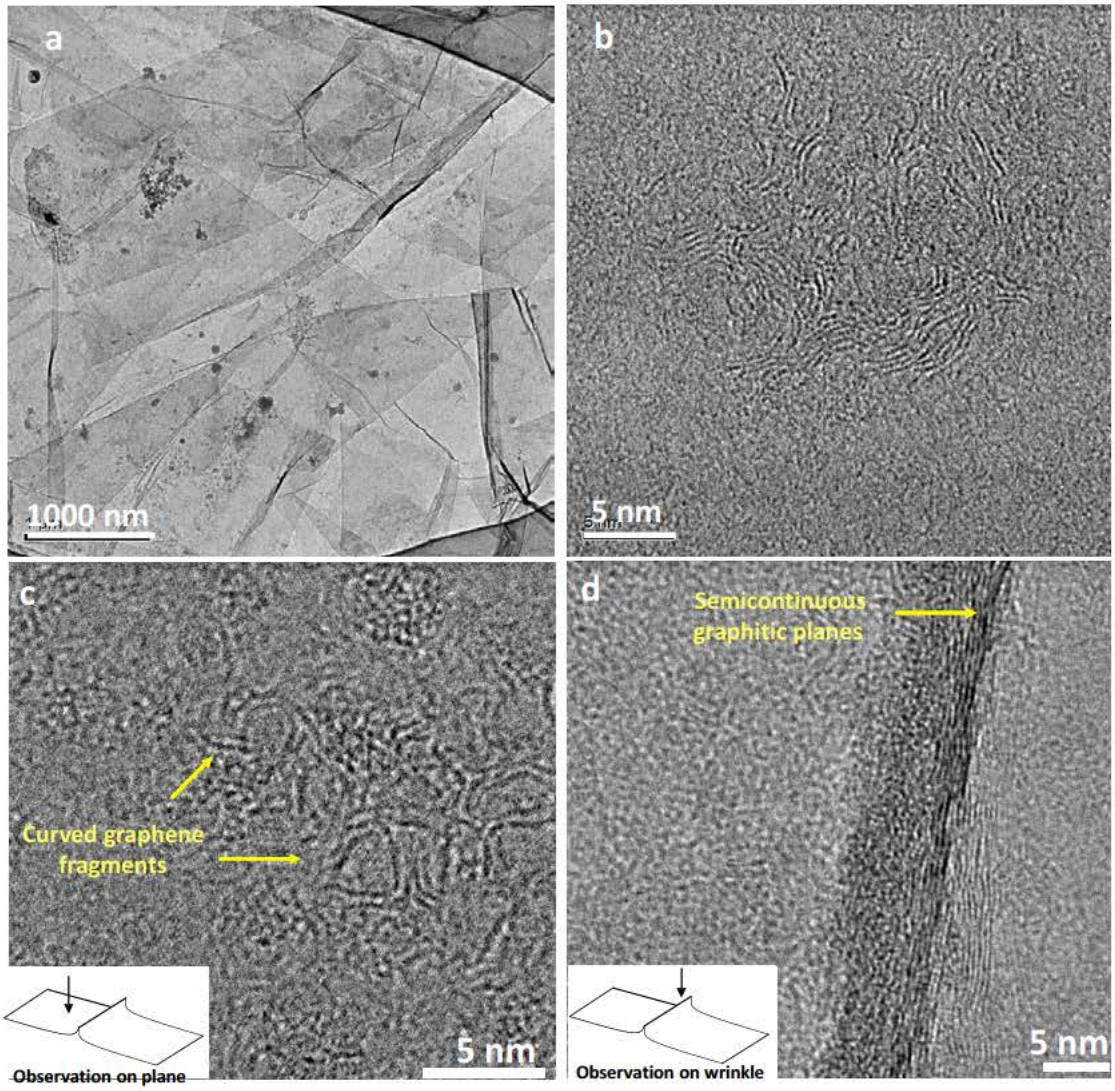

Figure 53. Transmission electron microscopy image of a 5-nm-thick carbon film (a,c,d). The carbon films are composed of randomly oriented and curved crystallites with sizes of up to 3 nm within an amorphous carbon matrix, which resembles the microstructure of glass-like carbons (c). A wrinkle was found on the film, in which some semicontinuous graphitic planes can be seen, similar to those in few-layered graphene (up to 5–10 layers) (d). The same fullerene-like fragments were detected in samples of different thickness like the 8-nm-thick film synthesized by using 420-60-60 sccm of Ar-H_2-C_2H_4 (b).

All these disorder-related effects in the Raman scattering of graphites are easily visible in the commercial glass-like carbon rod and our 5-nm-thick carbon film,

although are not in the more crystalline graphene (**Figure 54a**). In fact, additional peaks related to disordered carbon at about 1240 and 1480 cm^{-1} were also present in the Raman spectra of the 5-nm-thick carbon films (**Figure 54b**) [210], [211]. All this shows that our glass-like carbon samples are highly disordered, in agreement with TEM observations.

Then, the Raman spectra of all the carbon films were measured to compare their degree of disorder. The full width half maximum of D and G peaks ($FWHM_D$, $FWHM_G$) and the ratio between both intensities (I_D/I_G) after fitting are analysed. As can be clearly observed in **Figure 55a, b and c**, as the films become thinner the D peak narrows and I_D/I_G increases. Here, some interesting conclusions about the catalytic effect of copper can be extracted.

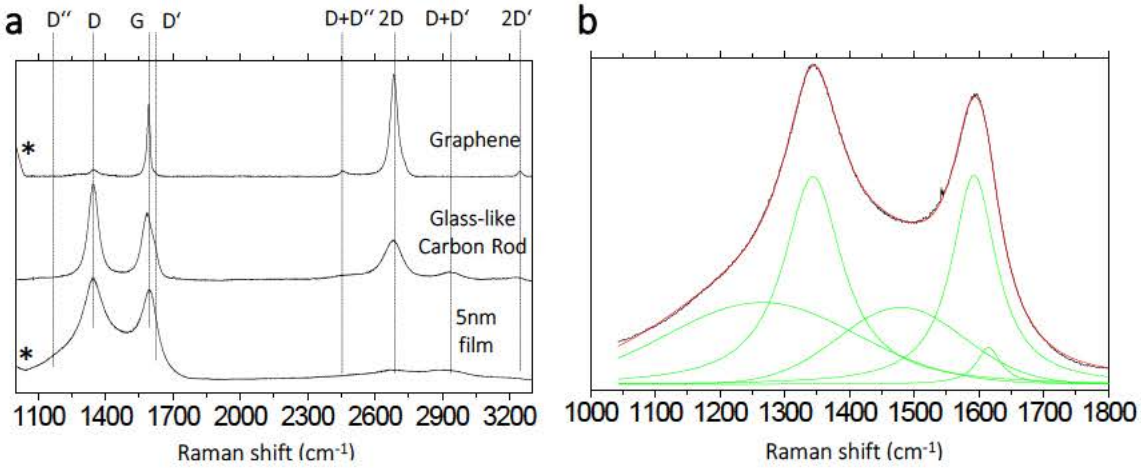

Figure 54 Raman spectroscopy studies of a) 5-nm-thick carbon thin films, commercial graphene, and a glass-like carbon rod. The disorder in the microstructure of glass-like carbon rod and our carbon film is evidenced by the appearance of the D peak at ca. 1350 cm^{-1}, the G band broadening (D′ peak ca. 1620 cm^{-1}), and the D″ band (ca. 1200 cm^{-1}). The peaks at ca. 2450 cm^{-1} and ca. 2950 cm^{-1} are the combination of D, D′, and D″ bands. Peaks at ca. 2700 cm^{-1} and 3250 cm^{-1} are the D and D′ overtones respectively. b) An additional peak related to disordered carbon at about 1480 cm^{-1} was also present in the Raman spectra of the 5-nm-thick carbon films. (*Raman signal of Si wafer support on graphene and thin carbon film).

The I_D/I_G ratio is widely used as a measure of the degree of disorder of the in-plane crystal size (L_a) of carbon materials, since the D peak arises from defects that decrease the crystal size. When in-plane crystal size is above *ca.* 3 nm, I_D/I_G and L_a are inversely related by the Tuinstra and Koenig relation, $L_a \propto (I_D/I_G)^{-1}$, which is the general behaviour observed for graphene-related materials (**Figure 56a**). However, when the in-plane crystal size is below *ca.* 3 nm many of the sp^2-hybridized carbon

rings open up and the vibration modes that produce the D peak cannot take place. In this scenario, the increment in the D peak is related to larger crystal size, following the relation $L_a^2 \propto (I_D/I_G)$ [200].

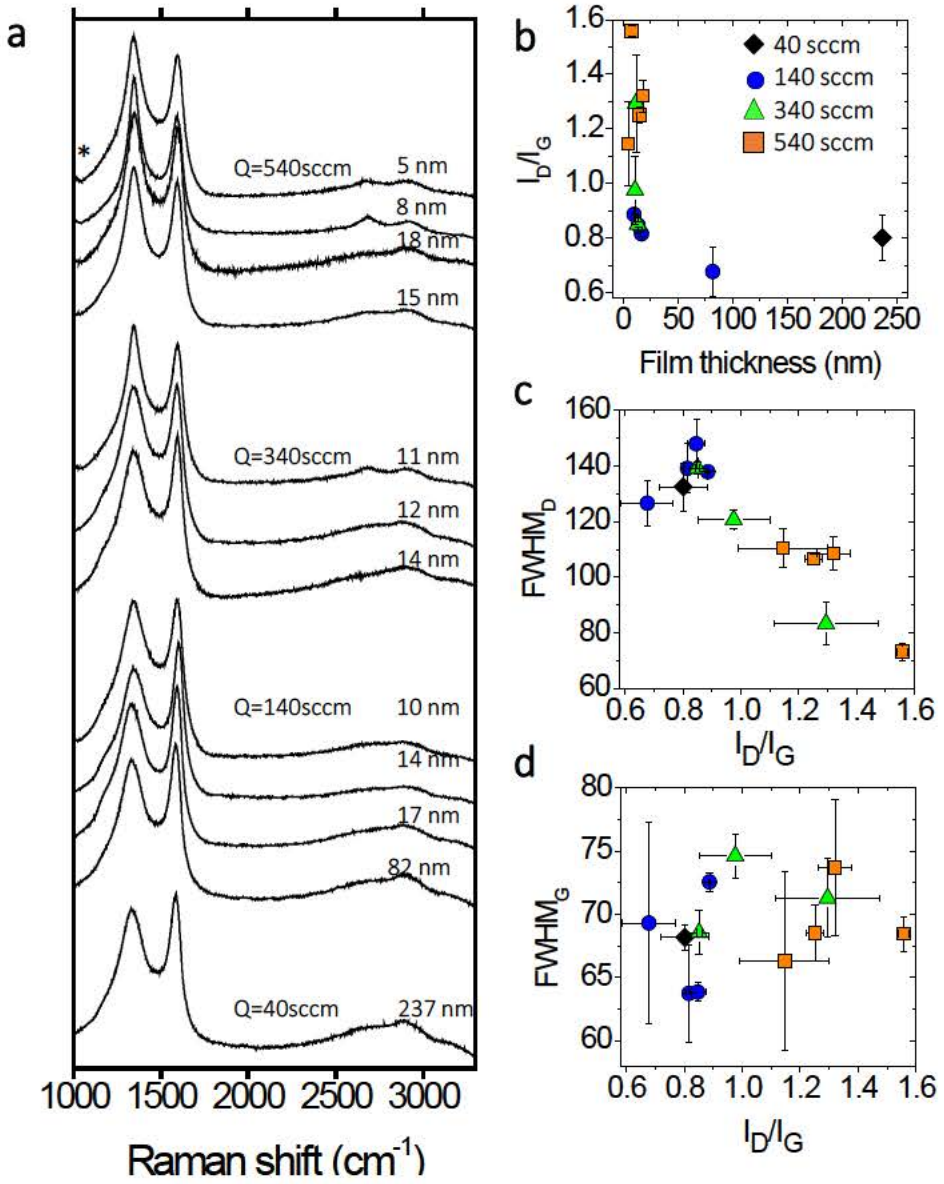

Figure 55. Raman spectra of carbon films synthesized on the copper foil. a) As the films gets thinner, the D peak narrows and increases compared to the G peak. The Raman contribution of the Si wafer substrate is detected for films up to 20 nm-thick*. b) Given the size of the crystals detected by TEM (La < 3 nm), I_D/I_G follows the direct relation $La^2 \propto (I_D/I_G)$ [200], which means that thinner films are more crystalline. c) The $FWHM_D$ confirms that thinner films are more crystalline than the thick ones. d) In-plane crystal size La can be deduced by analysis of the $FWHM_G$ [27]; we have an average crystal size of ca. 3 nm for the more crystalline sample. This value coincides with results from the TEM observation ($FWHM_G \approx 60$). The average crystal size is below 1 nm for the more disordered ($FWHM_G \approx 75$) areas.

In-plane crystal size, L_a, can be deduced by analysis of the $FWHM_G$ (**Figure 55d**), as both correlate directly (**Figure 56b**) as proposed in reference [27]. From these works we believe to have an average crystal size of around 3 nm for the more crystalline sample, which is in agreement with the TEM observation ($FWHM_G \approx 60$ cm^{-1}), and below 1 nm for the more disordered ($FWHM_G \approx 75$ cm^{-1}).

Since I_D/I_G clearly increases for thinner films (**Figure 55b**) and since we are below the Tuinstra and Koenig limit, our films follow the direct relation $L_a^2 \propto (I_D/I_G)$, which means that thinner films have a higher degree of order. This result can also be extracted by the analysis of the $FWHM_D$ (Figure 55c), which is known to be narrow in highly crystalline graphites and broader in disordered forms of carbon.

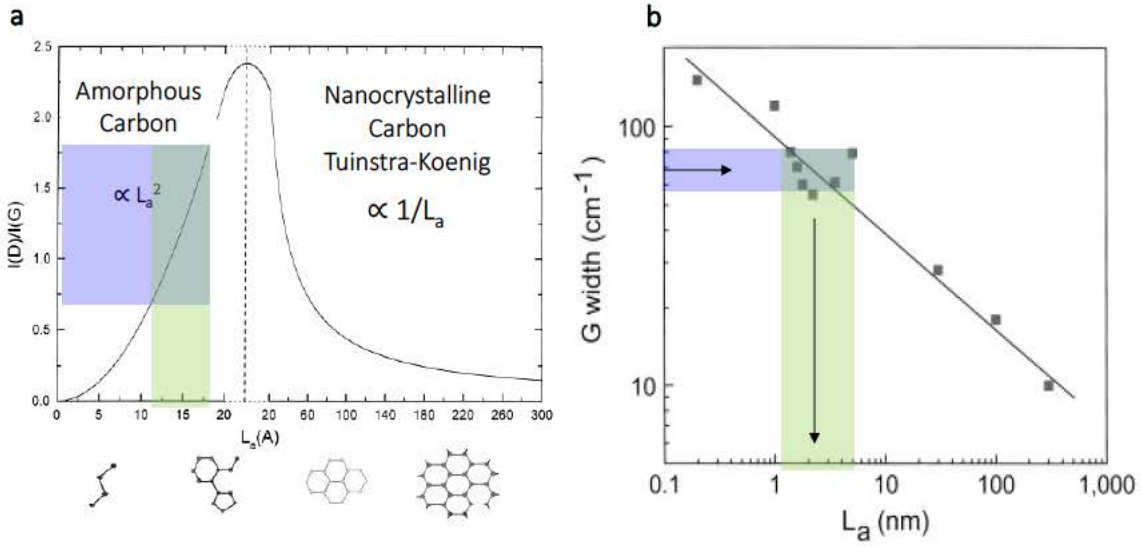

Figure 56 The I_D/I_G ratio is widely used as a measure of the degree of disorder of the in-plane crystal size (L_a) of carbon materials (a). When in-plane crystal size is above *ca.* 3 nm, I_D/I_G and L_a are inversely related by the Tuinstra and Koenig relation, $L_a \propto (I_D/I_G)^{-1}$ [200]. When the in-plane crystal size is below *ca.* 3 nm many of the sp^2-hybridized carbon rings open up and the vibration modes that produce the D peak cannot take place. In-plane crystal size, L_a, can be deduced by analysis of the $FWHM_G$, as reviewed in reference [27].

6.3.3. Carbon film anisotropy

The carbon film thickness was controlled by modifying the total gas flow and the ethylene concentration. As the temperature, annealing and synthesis time are constant for all the samples, the difference in their Raman spectra might be due to

the catalytic effect of the copper which only affects the crystallinity of the carbon film closer to the foil [96].

In this regard, it was identified by the analysis of I_D/I_G ratio and the $FWHM_{D,G}$ that the "bottom carbon film", which was in contact with the copper foil during CVD, has a higher degree of order than the carbon deposited as the CVD progresses ("top carbon film") (**Figure 57**a). It should be noted here that the Raman laser used (532 nm) has a probing depth of about 100 nm in amorphous carbon [212]–[214], so the more crystalline "bottom carbon film" is not fully reached by the Raman laser in thick films (**Figure 57**c) as compared to thin films (**Figure 57**b). This anisotropy through the thickness of the film [215], explains why thick carbon films showed less-ordered Raman spectra than the thin ones, as all the samples were analysed on the top surface of the film. This amorphous structure can be also seen by TEM in **Figure 53**b. These results highlight the importance of examining the film in its entirety rather than relying on Raman analysis.

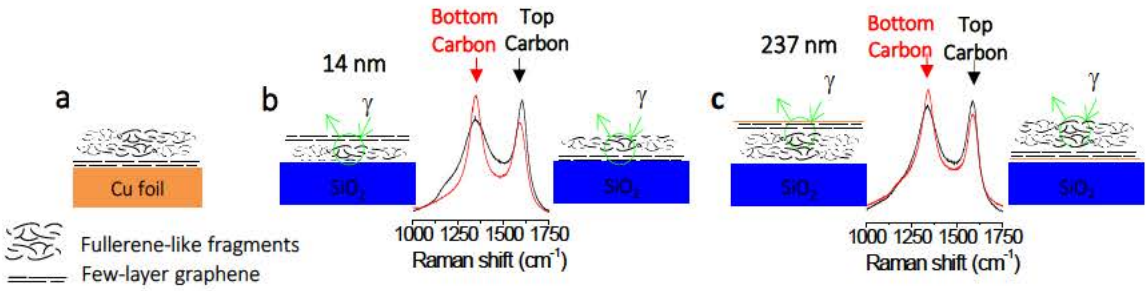

Figure 57 A proposed growth mechanism of the carbon films, which are composed of a few-layer graphene region underneath a region formed by fullerene-like fragments (a). The "bottom carbon" which was in contact with the copper foil during CVD, has a higher degree of order than the "top carbon", as detected in a 14-nm-thick carbon film (b) and a 237-nm-thick carbon film (c).

Despite it was found that carbon films are deposited even in quartz substrates for the 0-20-20 condition, copper substrates provide a higher graphitic deposition through catalytic processes. Among the variety of catalyst that can be used for the synthesis of carbon films, copper combines a very low carbon solubility and catalytic activity as well as high flexibility that makes it a unique catalyst for scalable roll-to-roll CVD systems [72]. Since it would be advantageous to have a process to produce films with high levels of crystallinity and easy to scale-up, thermal CVD using copper

foils is a convenient approach, despite other processes like plasma enhanced CVD can also be used for lowering the synthesis temperature.

6.4. Synthesis of graphene films

Most of CVD graphene recipes from the literature use a highly diluted carbon source coupled with the convenient synthesis time that results in an one-atom-thick film [72]. In the synthesis of glass-like carbon films presented in this Chapter, a highly concentrated carbon source was used along 5 minutes of synthesis, which exceeds by far the minimum carbon feedstock needed to generate a monolayer graphene [216]. The high ethylene concentration generates a high deposition rate on the surface of copper, faster than the graphene crystal nucleation and growth rate during the CVD process [96], [217], which after 5 minutes of synthesis results in films above 5 nm thickness (about 14 times monolayer graphene thickness [42]).

In this regard, the synthesis of graphene on a copper foil with purity of 99,8% (Sigma Aldrich) was compared to a copper foil with purity of 99.999% (Puretronics). Compared to the conditions to synthesize glass-like carbon films, (5 minutes and Ar-H_2-C_2H_4 = 500-20-20 and 850ºC), synthesis of graphene in our CVD reactor requires 5-10 minutes and a more diluted atmosphere with Ar-C_2H_4-H_2= 1000-20/200/400-0.5/1 and 950ºC.

The increase of the temperature is explained by an enhancement of ethylene decomposition, the catalytic activity of the copper catalyst and the diffusion kinetics of carbon atoms along the copper surface [72]. A more diluted ethylene atmosphere helps to slow down the carbon deposition rate and to be adjusted to the growing graphene crystals kinetics [216]. On the other hand, H_2 plays an important role in reducing oxides in the copper surface, so its increase helps to maintain a “cleaner” and more homogeneous surface. Also, the 99,999% pure copper catalyst has a smoother surface, on top of which diffusion of carbon radicals favoured the formation of a graphitic sp^2 bonded network. Contrary, radicals trapped in “valleys” on rough metal surfaces (Sigma Aldrich 99,8%) have slower surface mobility, leading to the formation of defected sp^3 bonded networks [216].

A growing defected and not continuous graphene crystals can be observed in **Figure 58**a (3 minutes with Ar-C_2H_4-H_2=1000-20-0.5), which highlight the need of a higher

carbon feedstock, which can be supplied either by increasing the synthesis time or the ethylene concentration. Contrary, exceeding the minimum carbon feedstock (10 minutes with Ar-C_2H_4-H_2 = 1000-20-1) results in evident second and third graphene layers (horizontal white arrow in **Figure 58**b). A wrinkle on monolayer graphene produced during cool down and due to thermal coefficient mismatch between copper and graphene (vertical white arrow) can be observed in this figure. Few-layer graphene crystal sizes are about 2 µm.

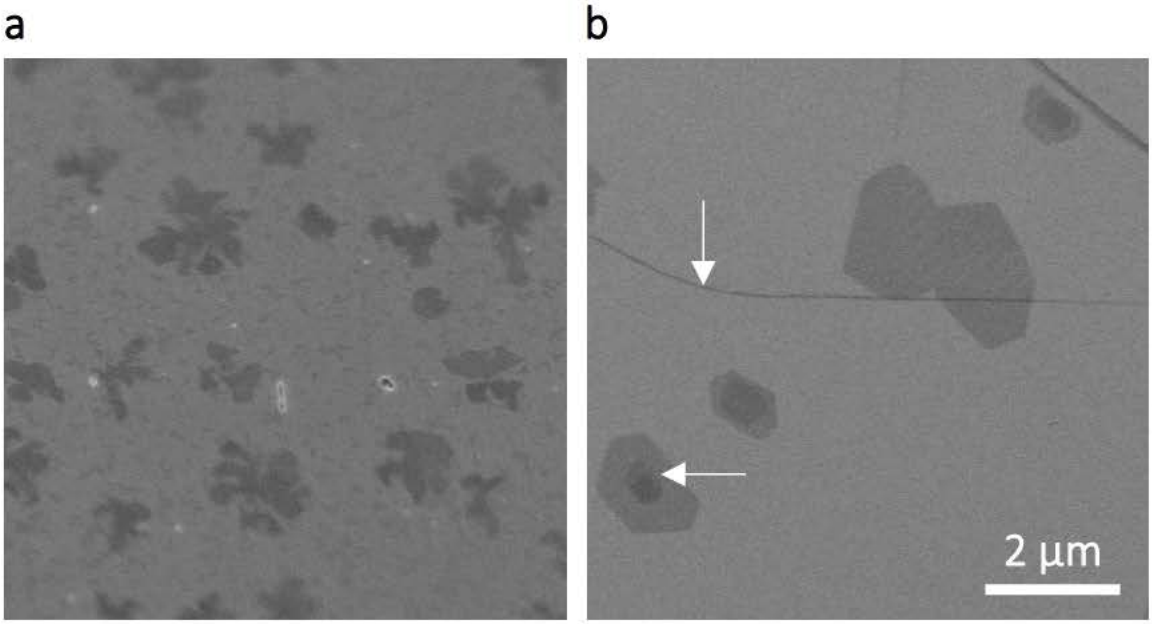

Figure 58 a) Graphene crystals growing on copper surface by CVD (3 minutes with Ar-C_2H_4-H_2 = 1000-20-0.5) and b) few-layer graphene after a longer growth time (10 minutes with Ar-C_2H_4-H_2 = 1000-20-1) showing evident second and third layers (horizontal white arrow) and a wrinkle (vertical white arrow).

Figure 59 and **Figure 60** show the SEM images and Raman spectra obtained during the optimization of the synthesis conditions of graphene by CVD on 99.8% and 99,999% copper foils respectively. Synthesis step using 0.5 sccm of C_2H_4 was carried out during 5 and 10 minutes and 20-200-400 sccm of H_2. Synthesis step using 1 sccm of C_2H_4 was carried out only during 5 minutes and 20-200-400 sccm of H_2. In both figures, it is indicated the two Raman parameters that identifies monolayer graphene; the full width half maximum of the G band (cm^{-1}) and the intensity ratio between the 2D and G band. The values corresponding to monolayer graphene are highlighted in red ($FWHM_G$ ~25-40 cm^{-1} and $I_{2D}/I_G \geq 2$ [218]), which are mostly achieved when using the 99.999% purity copper.

Copper purity effect on the synthesis of graphene. When the 99,8% purity copper foil is used (**Figure 59**), deposition of carbon films takes place at all synthesis conditions (from Raman and SEM information), in contrast to the 99,999% purity catalyst (**Figure 60**), where no graphene signal is detected at 0.5 sccm C_2H_4 and 200/400 sccm H_2. This result can be explained by the effect of impurities of copper, which are known to act as nucleation points of graphene seeds [219]. Thus at these synthesis conditions, the decrease of the concentration of impurities on the surface of copper disable the nucleation of graphene.

H_2 concentration effect on the synthesis of graphene. Impurities may also be diminished by using a highly reducing atmosphere by incrementing the H_2 concentration. It is known that H_2 is a necessary activator for monolayer growth that also controls the growth rate, size and morphology of the graphene domains [220]. In the present experiments, the effect of H_2 concentration is evident when using the 99.999% purity copper during synthesis for 10 minutes (0.5 sccm C_2H_4) and 5 minutes (1 sccm C_2H_4), decreasing the density of second and third graphene layers.

Despite Raman spectroscopy is the ultimate technique to determine the presence of monolayer graphene, we would like to highlight the potential of SEM to identify the presence of few-layer graphene regions. Given these results, we identified the CVD conditions of 5 minutes, 1 sccm of C_2H_4 and 200-400 sccm of H_2, using a copper foil of 99,999% purity as the optimum conditions of this experimental batch to synthesize graphene in our custom-made CVD reactor, despite further experiments might be carried out to supress the nucleation of additional layers.

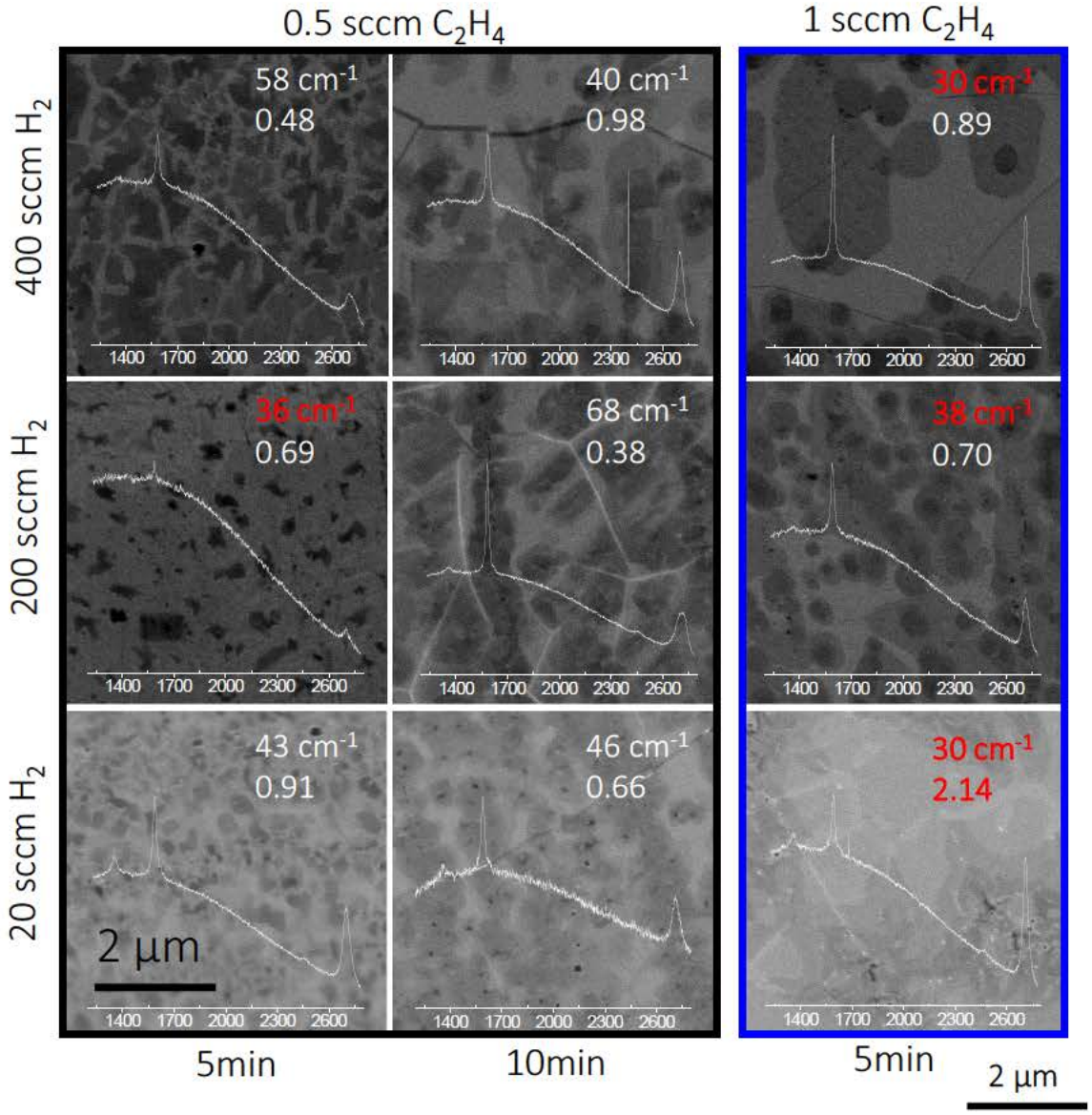

Figure 59 Optimization of the synthesis conditions of graphene by CVD on a copper foil of 99.8% purity. Synthesis step using 0.5 sccm of C_2H_4 was carried out during 5 and 10 minutes and 20-200-400 sccm of H_2. Synthesis step using 1 sccm of C_2H_4 was carried out only during 5 minutes and 20-200-400 sccm of H_2 The 5 minutes/0.5 sccm C_2H_4 serie do not produce continuous graphene films, and the synthesis of few-layer graphene can be observed in the 10 minutes/0.5 sccm C_2H_4 serie. The experimental conditions for 5 minutes/1 sccm C_2H_4 and 400 H_2 is found to be the optimum among the experiments, producing monolayer graphene with large second/third layer areas. Raman signal of graphene are highlighted in red ($FWHM_G$ ~25-40 cm^{-1} and $I_{2D}/I_G \geq 2$ [218]).

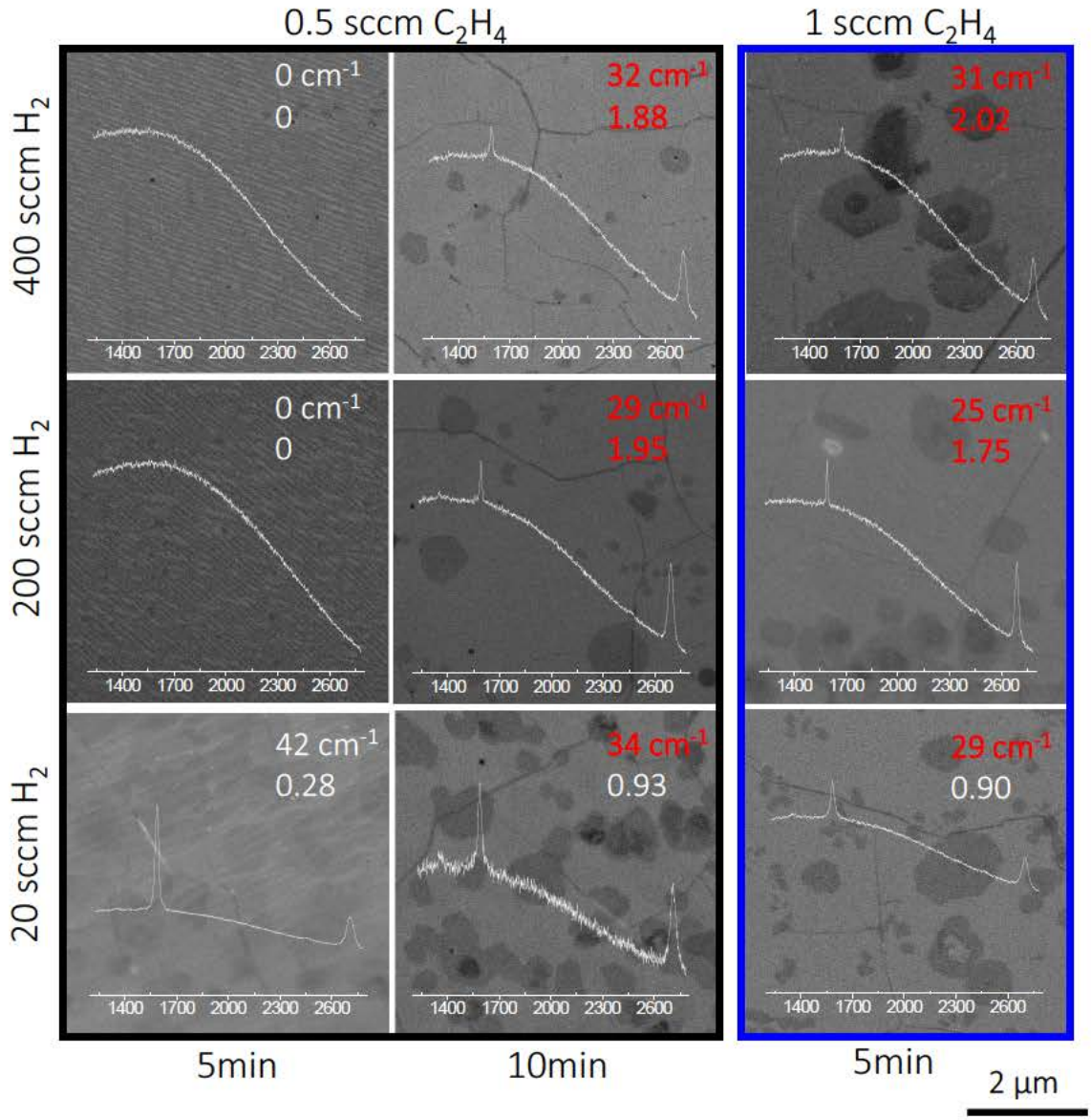

Figure 60 Optimization of the synthesis conditions of graphene by CVD on a copper foil of 99.999% purity. Synthesis step using 0.5 sccm of C_2H_4 was carried out during 5 and 10 minutes and 20-200-400 sccm of H_2. Synthesis step using 1 sccm of C_2H_4 was carried out only during 5 minutes and 20-200-400 sccm of H_2 The 5 minutes/0.5 sccm C_2H_4 serie do not produce continuous graphene films, and the increasing H_2 clearly suppressed the graphene growth. Few-layer graphene regions can be observed in the 10 minutes/0.5 sccm C_2H_4 serie, where increasing H_2 suppresses the growth of additional graphene layers. The experimental conditions for 5 minutes/1 sccm C_2H_4 and 200-400 H_2 are found to be the optimum, producing monolayer graphene with few second/third layer areas. Raman signal of graphene are highlighted in red ($FWHM_G$ ~25-40 cm^{-1} and $I_{2D}/I_G \geq 2$ [218]).

Raman mapping experiments were performed on samples synthesized during 5 minutes, 1 sccm of C_2H_4 and 400 sccm of H_2 using the 99.999% purity copper, in order to confirm and determine the regions of monolayer and few-layer graphene (**Figure 61**). As it was expected, the few-layer graphene crystals of about 1-2 μm detected by SEM (right inset) correlate with the orange and red regions in the Raman maps (both full with half maximum of 2D band and 2D/G ratio).

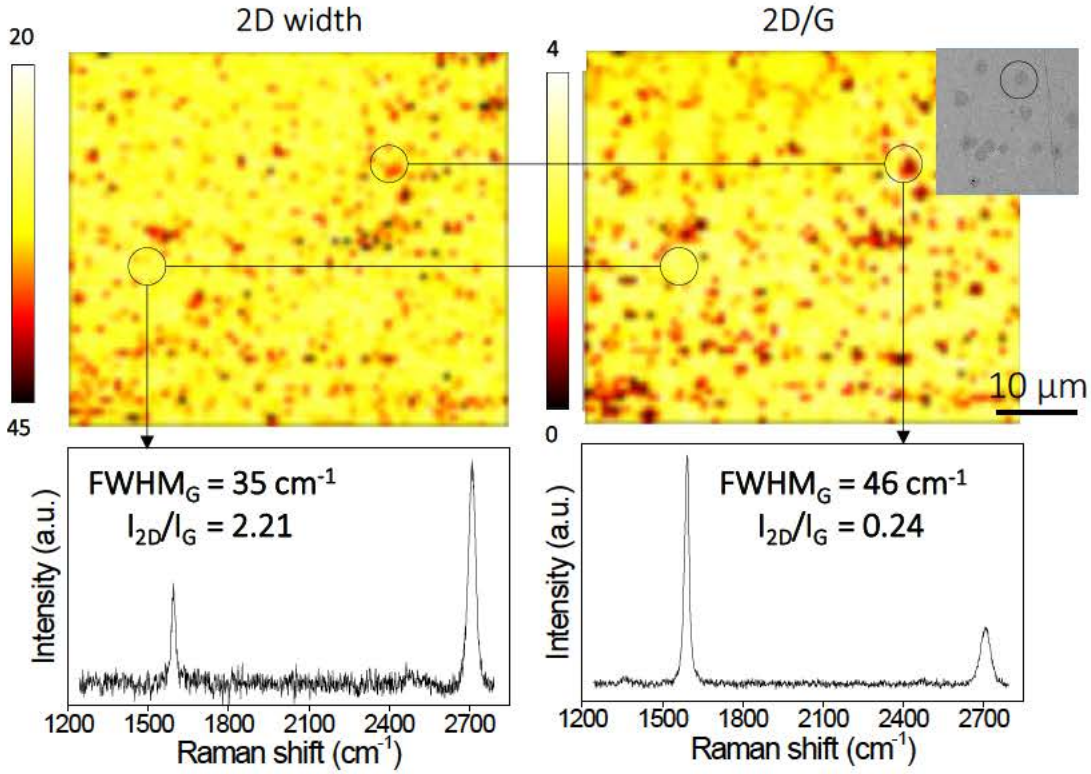

Figure 61 Raman mapping of the samples synthesized during 5 minutes, 1 sccm of C_2H_4 and 400 sccm of H_2 using a 99,999% purity copper. Monolayer graphene regions are shown in light yellow and few-layer graphene up to ~4 layers are detected by the increasing orange-to-red [218]. The crystals of few-layer graphene of about 1-2 μm are detected by SEM (inset) and Raman mapping (orange and red regions).

6.5. Summary

In this chapter, it was studied the synthesis of carbon thin films on top of copper foils by the chemical vapor deposition using different gas conditions. Carbon film thicknesses from 5–237 nm were obtained by tuning the gas flow rates from 40–540 sccm and ethylene concentration from 0.04–0.5. The resulting carbon film thicknesses were proportional to the ethylene concentration and inversely

proportional to the gas flow. Transmission electron microscopy and Raman spectroscopy showed that the carbon films were formed by randomly oriented curved graphene nanocrystallites which showed order in ranges up to 3 nm, which resembles the fullerene-like fragments that form glass-like carbons.

Raman results demonstrated that, as the CVD progresses and carbon film thickness increases, the carbon is deposited with lower degree of order (amorphous), so higher crystallinity was achieved in contact to the copper foil. Consequently, thinner films are more crystalline than the thicker films, which were composed of a thin and crystalline region underneath a thick and amorphous region. It was also demonstrated the synthesis of monolayer graphene with our custom-made atmospheric pressure CVD furnace, and a highly pure copper catalyst improves the graphene quality, on top of which the graphene deposition is more controllable.

7

Glass-like carbon thin films: Physical characterization and polymer-assisted transfer by thermal shocks

7.1. Glass-like carbon films

Since the in-depth characterization of graphene properties in 2004 [20], there has been a renewed interest in carbon nanomaterials as thin films for a wide variety of applications, such as energy production/storage, biocompatible scaffolds, and electronics, among others [41], [53], [221], [222]. In the previous Chapter we have demonstrated the synthesis of glass-like carbon thin films of different thicknesses, which may found applications as a multifunctional surface.

Glass-like forms of carbon are a good example of disordered sp^2-hybridized carbon materials. The structure of glass-like carbons consists of nearly 100% sp^2-hybridized carbon atoms, which forms randomly oriented fullerene-like fragments of different sizes, depending on the intensity of the heat treatment used for their production [3], [31], [32], [204]–[206]. At bulk state, they show glass-like appearance and combine interesting properties such as high temperature stability, extreme resistance to chemical corrosion, high hardness, low density, and high impermeability to both gases and liquids [2], [31], [32]. Interestingly, glass-like carbon thin films can also be produced by pyrolizing a photoresist resin [28], which are transparent as transparent as graphene films of similar thickness. Interesting functional materials such as flexible neuroelectronic implants for dopamine sensing were recently obtained by pyrolizing a photoresist resin [52]. Carbon materials with a similar amorphous structure can also have an exceptional specific surface area due to their high density of edge defects, which are of great interest for energy-storage applications [12], [54].

Also, the embedded nanocrystallites within amorphous carbon matrixes can induce strong paramagnetism [226]–[229], which is ascribed to the presence of a spin magnetic moment at the graphene layer edges. In summary, the presence of nanoscale crystals in carbon materials may have advantages for advanced applications over the more crystalline forms of carbon such as graphene or nanotubes.

Now, we can highlight several facts that make our production of glass-like carbon films competitive against graphene, and encourage the study of their applicability. On the one hand, the larger thickness of our glass-like carbon film compared to monolayer graphene makes it easier to visualize and to manipulate, and its amorphous nature is easier to replicate. In this regard, it is known that graphene grain boundaries and defects are not possible to be fully controlled during CVD. But probably the most important advantage, as it will be shown in this Chapter, is the partial delamination of our glass-like carbon films right after CVD due to the large thermal expansion coefficient mismatch between the carbon film and the copper catalyst foil.

Electrical and optical properties of the glass-like carbon films are characterized in this Chapter, and compared to other carbon-based thin films in the framework of transparent and flexible electrodes. Surface wettability is also studied and related to ongoing research on biocompatibility applications. Finally, the production process of the glass-like carbon thin films is completed by studying a new non-destructive and highly scalable transfer process to polymer films by thermal shocks.

7.2. Physical properties of glass-like carbon film composites

7.2.1. Electrical conductivity and optical transmittance

Transparent and flexible conducting films are of increasing importance for several applications such as electronic devices and photovoltaics. Currently, transparent conductive oxides like indium tin oxide (ITO) dominates the industry, however they are rigid and brittle [40]–[42]. Carbon nanomaterials like graphene films are

generating great expectations as alternatives [43], since they are produced by inexpensive starting materials (like hydrocarbons and polymers), and are showing superior film mechanical properties, flexibility/durability, and high levels of in-plane conductivity. The electrical conductivity and optical transmittance of the thinnest carbon films (<20 nm) are presented in this chapter, as well as a comparison with other carbon-based films recently reported in the literature.

The thinner carbon films (<20 nm) were spin-coated with PMMA (495PMMA A Resists, Microchem). Copper was etched away (using Sigma Aldrich 667528), and finally the carbon thin film/PMMA was electrically characterized (**Figure 62**). The sheet resistance of the samples was measured by using contactless conductivity equipment LEI88 (Lehighton Electronics Inc.). Each measurement was performed at least 20 times, hence the uncertainty interval for each sample. Optical transmission measurements were performed by using a spectroscopic reflectometry–transmission equipment on a Canon microscope (Sentech FTP). Measurements were obtained by using a ×10 microscope objective that provided a spot with a diameter of around 20 μm.

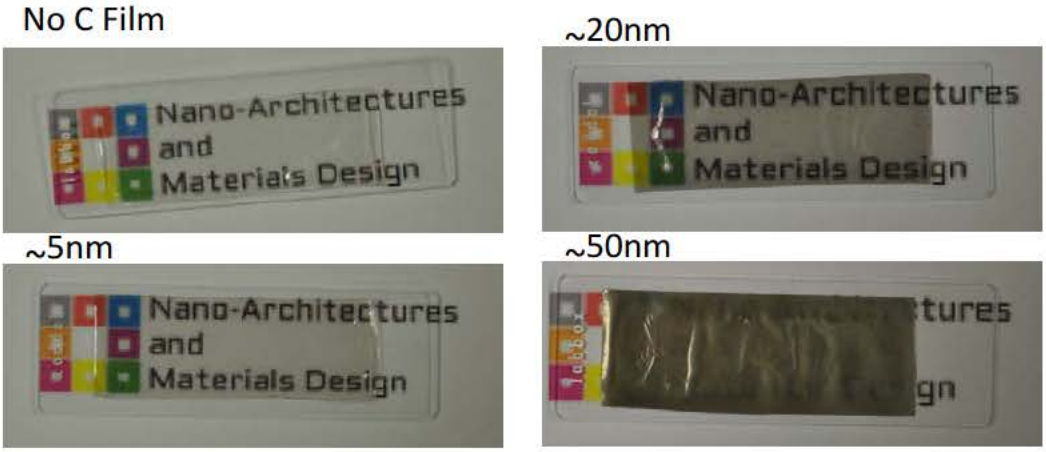

Figure 62 Carbon films with different thicknesses transferred to PMMA.

The sheet electrical resistance (R_s) and transmittance (T) at 550 nm decrease with the thickness of the film (**Figure 63**a,b respectively). As expected, thicker films are more conductive and less transparent. Limit values are $R_s = 7.836 \pm 1.500$ kΩ at T = 85,7% (for 5 nm carbon film) and $R_s = 4.298 \pm 0.140$ kΩ/□ at T = 58.65% (for 18-nm-

thick carbon film). These results are compared to those of equivalent N-layer graphene (**Figure 63**a). Electrical conductivity of N-layer graphene depends on charge carrier density ($n=3,4 \cdot 10^{12}$ cm^{-2}), electron mobilities ($\mu=20000$ cm^{2}V^{-1}s^{-1}) and electron charge ($e=1,6 \cdot 10^{-19}$ C) as proposed by Bonaccorso et al [41], following the next equation:

$$\sigma_{DC\ (N\ layers)} = (n\ \mu\ e) \cdot N\ layers = 0,01088\ S/layer \cdot (N\ layers) \quad (7.1)$$

being the sheet resistance $R_s = 1/\sigma_{DC\ (N\ layers)}$ about one order of magnitude lower than our glass-like carbon films. The electrical conductivities (σ_{DC}) of the carbon films synthesized in this work were calculated to be $\sigma_{DC}=8.7 \times 10^3 - 2.5 \times 10^4$ S/m. Comparing with the literature, these values are lower than bulk highly oriented pyrolytic graphite (2.50×10^6 S/m), similar to bulk glass-like carbon and pyrolyzed photoresist thin films, and well above those of amorphous carbon (10^2 S/m) [29], [230]. The large error obtained in some measurements is attributed to damage during the transfer of the carbon film to PMMA by acid etching.

Regarding graphene transmittance (**Figure 63**b), it follows the equation:

$$T = (1-\pi\alpha)^N \quad (7.2)$$

where ($\alpha = e^2/\hbar c \approx 1/137$ is the fine structure constant, c the speed of light, and N the graphene number of layers [26], [231]). For N-layer graphene thickness, it has been assumed a distance between graphene layers of 0.35 nm [42]. Interestingly, most of the carbon films obtained are more transparent than the equivalent-thick graphene.

Figure 64 shows some results of previous studies on amorphous carbon films synthesized from 400ºC to 1100ºC on different substrates. Some of them were deposited directly on insulating substrates like SiO_2 or sapphire, obtaining values up to $R_s = 100$ kΩ/□ at T=93% by controlling the thickness of the film with the synthesis time at 950ºC and 20 Torr. of pressure [232], or up to 6 kΩ/□ and 80% at 1100ºC [29], [233]. Others studied the deposition at 1000ºC on copper foils resulting in 0.717 kΩ/□ at 41.4%, 1.6 kΩ/□ at 80% or 610 kΩ/□ at 96% [234]–[236]. All these results are collected in **Figure 64** and compared to theoretical graphene [41].

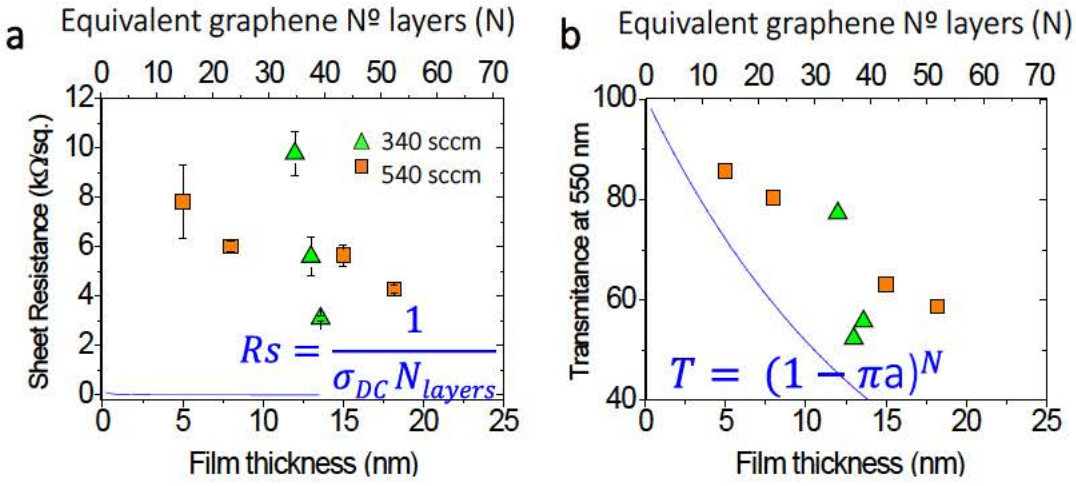

Figure 63. Electrical and optical performance of carbon films. a) The sheet resistance (R_s) and b) transmittance at 550 nm (T) decreases with the thickness of the films, showing limiting values of R_s=7.836±1.500 kΩ/□ coupled with T=85.66% (for a 5-nm-thick carbon film), and R_s=4.298±0.140 kΩ/□ at T=58.65% (for 18-nm-thick carbon film). Blue lines correspond to theoretical graphene values.

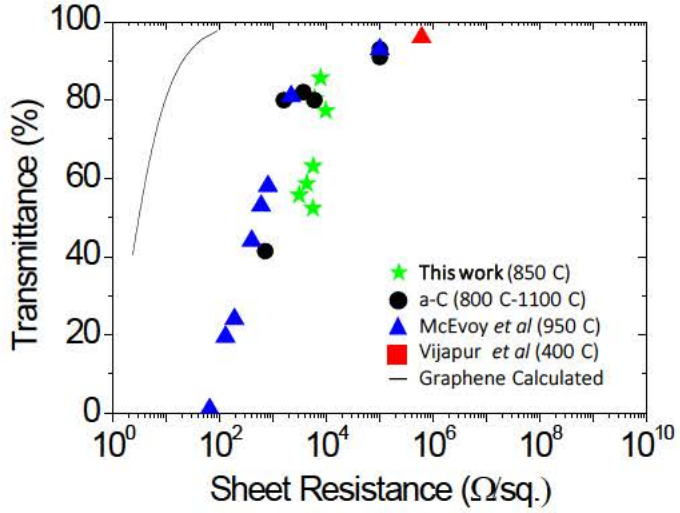

Figure 64. Figure of Merits of amorphous carbon films compared by R_s and T values. A wide range of R_s and T values on carbon films can be obtained by varying the synthesis temperature and the thickness of the film.

The optoelectronic properties of our carbon films are compared with those reviewed by De et al [42]. The authors summarized in **Figure 65**a,b the transmittance (at 550 nm) and sheet resistance of CVD continuous graphene and graphene-based composites such as those produced with graphene oxide / chemically modified, liquid

exfoliated and synthetic graphene flakes. We have incorporated in this figure the data obtained on our continuous carbon film/PMMA composite. It is clear that our films show similar performance of liquid exfoliated graphene composites as well as those obtained with reduced graphene oxide, but an inferior electrical conductivity compared to graphene (~$3 \cdot 10^5$ S/m).

A good measure for the suitability of a material for transparent electrode applications is given by the σ_{DC}/σ_{OP} ratio, which incorporates both electrical (σ_{DC}) and optical (σ_{OP}) conductivities:

$$\boldsymbol{\sigma}_{DC} / \boldsymbol{\sigma}_{OP} = Z_0 / 2R_s (T^{-1/2} - 1) \qquad (7.3)$$

where Z_0 is the characteristic impedance of vacuum (*ca.* 377 Ω), T the transmittance at 550 nm, and R_s its sheet resistance. Our best value is σ_{DC}/σ_{OP}~0.3 with a carbon film thickness of ~5 nm, meanwhile best values found in the literature have shown an impressive performance of σ_{DC}/σ_{OP}=8900 with 0.5Ω/□ at T=94% by designing a graphene/metal grid structures [237], well above the minimum industry of σ_{DC}/σ_{OP}~35 to replace ITO in transparent electrode applications.

Figure 65. Figure of Merits of our carbon films compared to CVD graphene and composites made out of graphene flakes (optical conductivity (a) and electrical conductivity (b)). The carbon thin films synthesized in the present work show similar performance to that of liquid exfoliated graphene composites, as well as those obtained with reduced graphene oxide (RGO) (a). The optical performance of our films is in the range of graphene (dashed lines), but the electrical conductivity is one order of magnitude below.

7.2.2. Wettability

The glass-like carbon thin films prepared in this work can also be used to design multifunctional surfaces for antimicrobial or biocompatible materials. On the one hand, adhesion of microorganisms has to be avoided in food processing and storage applications, but may result beneficial in other applications such as wastewater treatment bioreactors or biopolymer degradation. Biocompatibility of surfaces is determined by their topography and physicochemical properties, and has been associated to their hydrophobic-hydrophilic nature [238]. Interestingly, hydrophobic surfaces may turn hydrophilic by applying external stimuli such as electrical potential or ultraviolet irradiation (UV). Such treatments are thought to cause the adsorption and dissociation of water molecules and generate surface hydroxyl groups, and has been demonstrated with graphene and CNT films [239], [240].

Here, we studied the surface wettability by means of water contact angle of our glass-like carbon films (5-nm-thick films). It is demonstrated the hydrophobic-to-hydrophilic transition when carbon films are irradiated using different UV sources. Results relating the biocompatibility of the irradiated glass-like carbon surfaces are presented by means of microbial colonization in a peer-review publication [238].

Preparation of glass-like carbon/PMMA composites. As synthesized the carbon film of about 5 nm thickness were transferred into a polymer film following the next sequence: the carbon film/copper is gently flattened using two clean glass holders. Three drops of a PMMA (495PMMA A Resists, Microchem) were homogeneously placed on top of the carbon film/copper using a plastic disposable pipette. PMMA drops are distributed along the surface following the doctor blade technique using a laboratory weighting paper. We let them dry on air (2h) and repeated the process 2 more times. Once the PMMA is dried, the composite PMMA/carbon film/copper is placed on a $FeCl_3$ – HCl copper etching solution (Sigma Aldrich 667528) with the PMMA facing down. The sample must be totally submerged. After 2 hours, the whole copper etchant was replaced for a new fresh one, and let it etch for additional 24 hours. Next, we removed the copper etchant and clean the sample with deionised water replacing the water 5 times, and let it clean in a deionised water bath for additional 24 hours. After the cleaning process, PMMA/copper film was “fished” from

the deionised water with a clean glass holder. The whole sample was cut in slices with a clean stainless steel blade (10x15 mm approx, and 6 samples are obtained from each CVD). Those cut samples were submerged in new deionised water and "fished" with covering glass (0.13-0.16 mm thickness, Labbox). The samples were dried on a vacuum oven at 50ºC for 2 hours.

Surface topography analysis. Surface topography of the carbon film/PMMA composite was characterised by AFM at ambient conditions using a Park XE150. The images were acquired by non-contact mode using a non-contact cantilever (PPP-NCHR, Park System), with a tip set point of about ~30-40 nm and amplitudes between ~25-45 nm with a scan rate of 0.50 Hz. The obtained images (512 x 512 pixels and areas of 10 μm^2 and 2 μm^2) were processed and analysed using XEI software (version 1.7.1).

Ultraviolet irradiation. Prior to irradiation, carbon films were heated at 50°C for 2 hours under vacuum of 10 kPa). UV irradiation of glass-like carbon films was performed at room temperature (~20°C) under two different atmospheres of relative humidity, a dry (30% ± 5% RH) and wet (80% ± 5% RH). At least 5 minutes of preconditioning were applied before irradiation. The equipment used for irradiating the carbon films were: (1) A 15 W Heraeus Noblelight TNN 15/32 low-pressure mercury vapour lamp emitting at 254 nm with a secondary peak at 185 nm. (2) Vilber-Lourmat Bio-Lin BLX-254 Crosslinker equipped with 5 x 8 W 254 nm T-8C lamps. (3) A diode pumped passively Q-switched solid state laser FQSS 266-200 (CryLas, Germany) emitting pulses (< 1.5 ns) at 266 nm > 200 µJ at 20 MHz. The selection of these different UV sources aims at studying the effect of the more energetic vacuum UV light (100-200 nm), mostly produced in the low-pressure mercury lamp compared to the other sources, because it is thought that can photolyse water molecules into hydrogen atoms and hydroxyl radicals.

Wettability measurements. The wettability of carbon films was tested as soon as possible after irradiation using an optical contact angle meter (Krüss DSA25 Drop Shape Analysis System) at room temperature using the sessile drop technique.

Irradiation and water contact angle studies were carried out in collaboration with the Department of Chemical Engineering, University of Alcalá, Madrid, Spain.

Water contact angle of transparent glass-like carbon films was measured before and after irradiation with different UV doses. **Figure 66**a shows the effect of irradiation at different UV doses on the water contact angle measured in transparent glass-like carbon films. For non-irradiated glass-like carbon films, water contact angle resulted > 80º, indicating a relatively hydrophobic surface. Water contact angle decreased sharply upon irradiation from 99.0º ± 3.4º up to 22.8º ± 2.5º when irradiated with the low-pressure lamp under wet conditions, indicating a hydrophilic nature. This decrease was much slower when using the "ozone-free" lamps, and no significant effect was observed for irradiation using the 266 nm solid-state laser.

After irradiation, glass-like carbon films were stored under laboratory conditions (1 atm, 20ºC) to investigate the recovery of water contact angle. The results (**Figure 66**b) showed that during the first 24 h following irradiation (first measure after 1 h of irradiation), the samples recovered most of their hydrophobicity, with contact angle values increasing up to the 81º–89º range. After 24 hours, all samples displayed a water CA > 90º, close to the values of non-irradiated carbon films.

Carbon films have been shown to display important differences in wettability, switching from hydrophilicity to super-hydrophobicity [241]. Previous works suggests that oxygen chemisorption would lead to hydrophilic surface moieties, such as hydroxyl groups. Water molecules would physically adsorb at the surface, which results in a reduced water contact angle, thus reversibility can be explained by desorption of surface water.

We have analysed the surface of the transferred carbon film on PMMA before and after UV irradiation with the low-pressure mercury lamp, in order to identify possible changes on surface roughness that may contribute to the wettability transition. First of all, we analysed the surface features in the copper foil. The copper foil developed roughness in the form of nanoparticles up to 300 nm after synthesis (**Figure 67**a), which was transferred into the carbon film/PMMA composite in the form of wholes of the same size (**Figure 67**b).

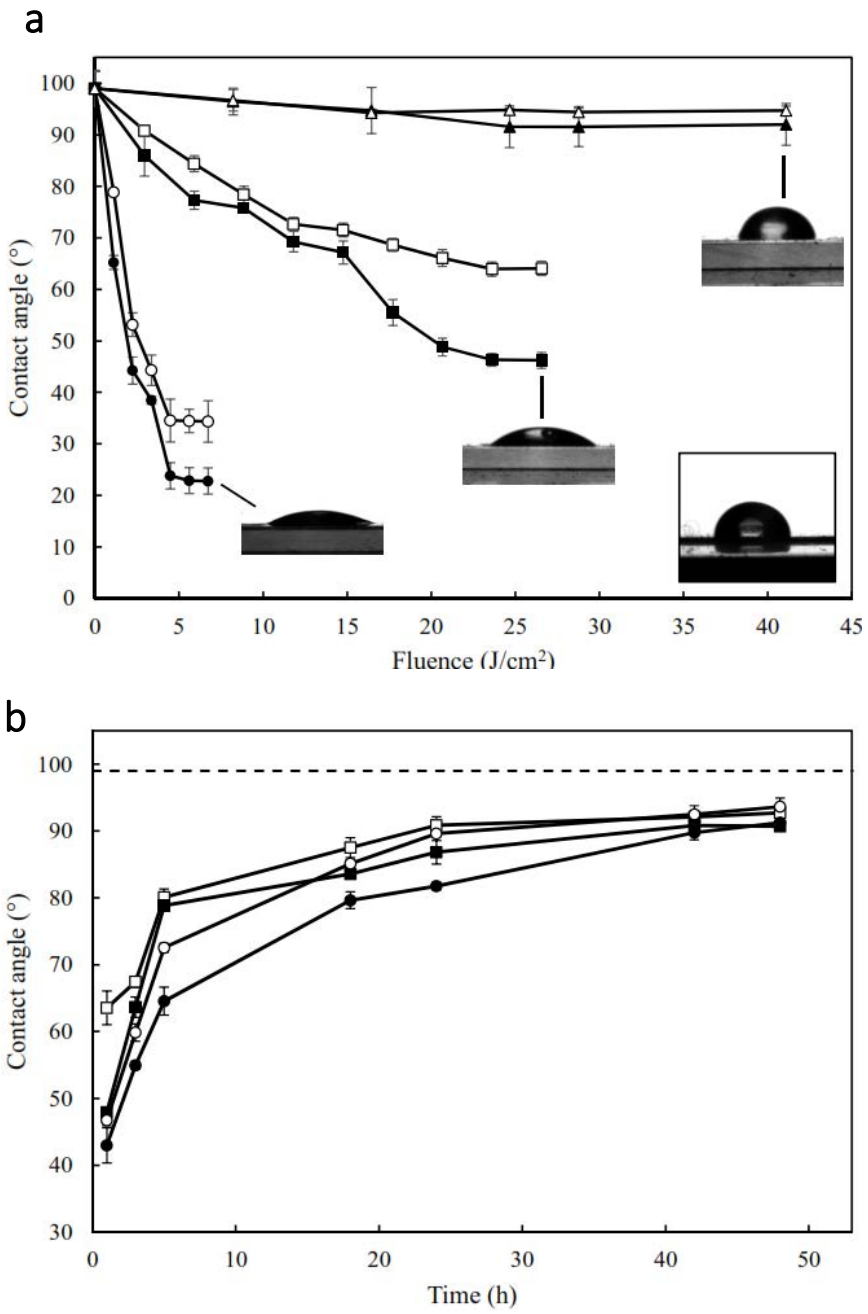

Figure 66 (a) Water contact angles of transparent glass-like carbon films for different irradiation devices and UV doses. Low-pressure mercury lamp (○, ●), irradiation chamber (□, ■), laser (Δ,▲). Empty symbols: dry air (~30% RH), filled symbols: wet air (~80% RH). Inset at the bottom right: glass-like carbon after vacuum treatment and before irradiation. (b) Evolution of water contact angles of irradiated glass-like carbon films for different times under ambient conditions.

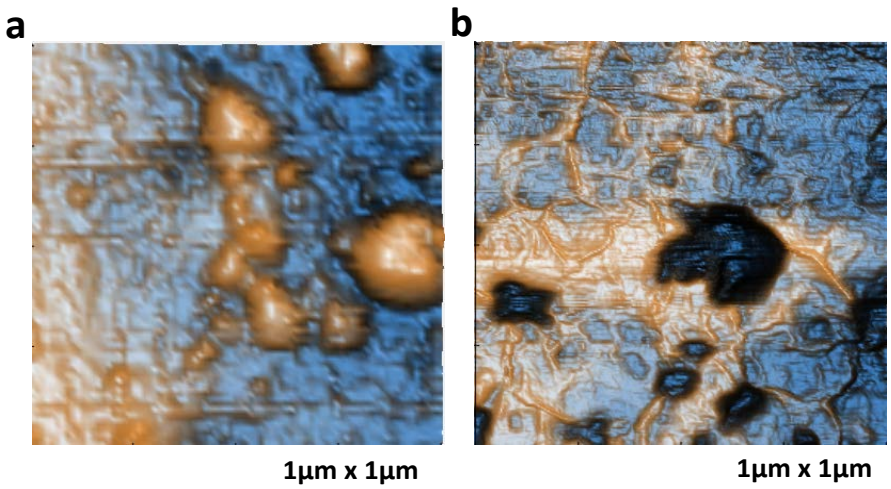

Figure 67 The copper surface features (a) are transferred into the carbon film/PMMA composite (b).

Figure 68 shows the evolution of a 10 µm² surface before irradiation (a), right after irradiation with the low-pressure mercury lamp under dry conditions, and the same are 96 h after this irradiation, when contact angles is completely recovered.

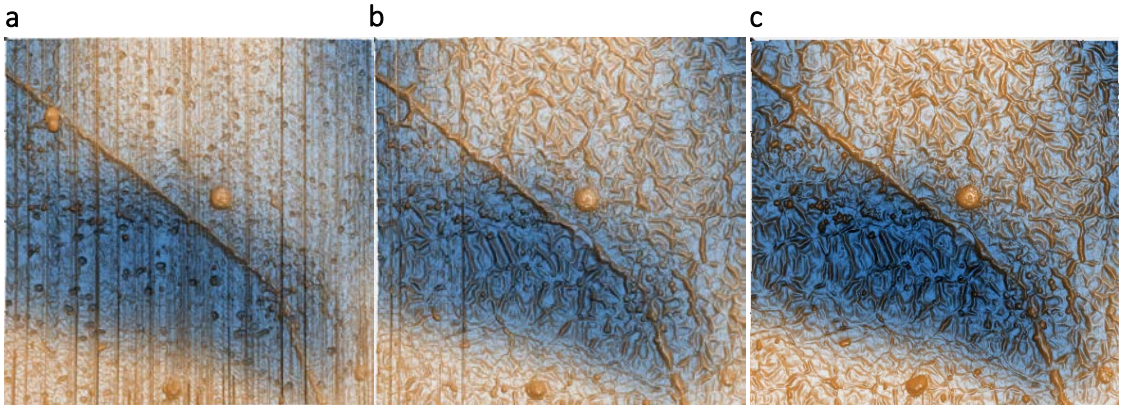

Figure 68 Evolution of a 10 µm² surface before irradiation (a), right after irradiation with the low-pressure mercury lamp under dry conditions, and the same area 96 h after this irradiation. Areas of 10 x 10 µm. Vertical and horizontal lines are typical AFM artefacts.

The surface before irradiation showed the same surface features presented in **Figure 67** corresponding to nanoparticles up to 300 nm, and after irradiation several globular and vermicular features appeared (b), and some of the cavities of non-irradiated samples almost disappeared. AFM analysis of the same region 96 h after irradiation (c) did not show any difference compared to the surface

right after irradiation. Thus, it can be concluded that hydrophobicity recovery is not due to surface roughness evolution.

A deeper analysis (**Figure 69**) showed that the globular and vermicular features detected after UV treatments derived from original surface features presented in the carbon film/PMMA composite after transfer (**Figure 69**a, c). These features seemed to swell and smooth because of the irradiation (**Figure 69**b, d). UV treatment in wet air seems to show smoother and more swollen features than those irradiated in dry air.

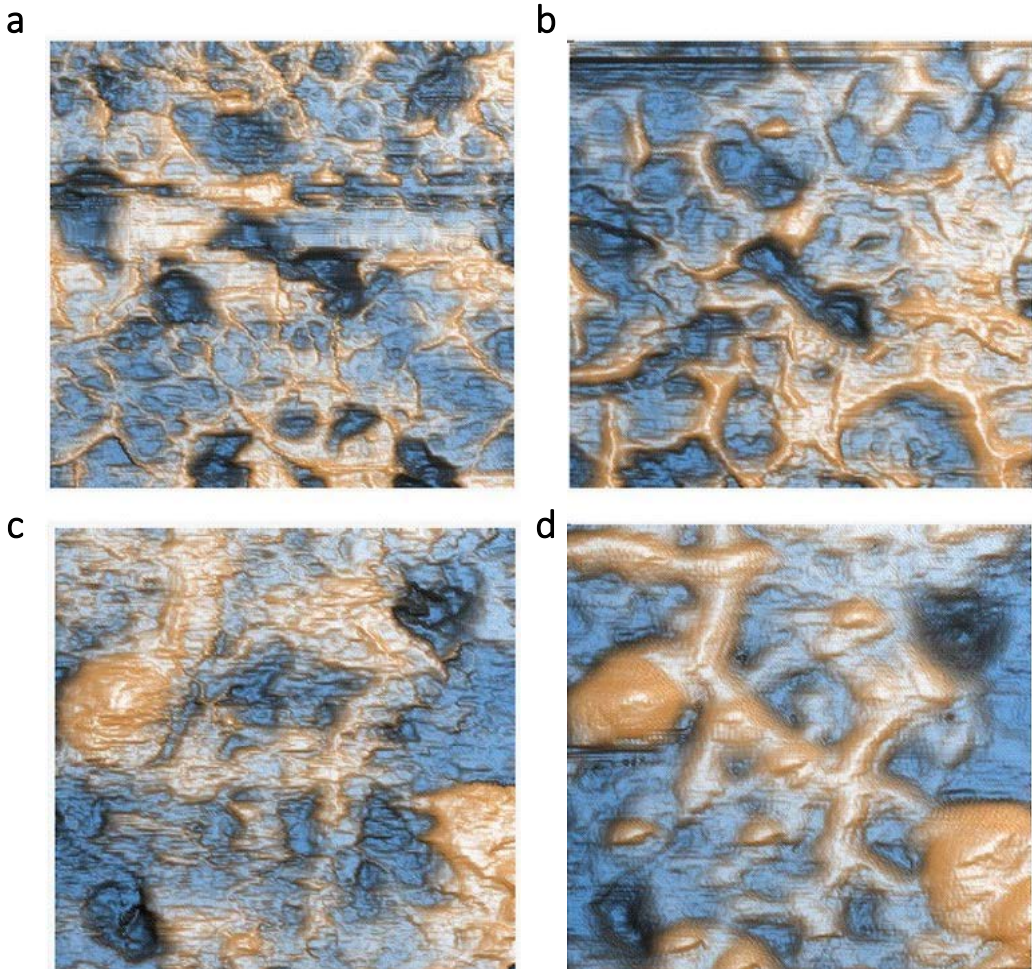

Figure 69 AFM analysis of the surface of carbon film/PMMA composites before UV treatments (a, c) and after UV dry treatment (b) and UV wet treatment (d). Vertical and horizontal lines are typical AFM artefacts (AFM areas of 1 x 1 µm).

7.3. Polymer-assisted transfer by thermal shock delamination

Carbon films synthesized on copper foils by CVD, such as graphene or the glass-like carbon thin films presented in Chapter VI, need to be transferred from the copper catalyst foil to the device where it will be applied. The preparation of carbon thin film/PMMA composites followed in Section 7.2, consisted on depositing a protecting polymer film (PMMA) and dissolving the copper catalyst by chemical etching [43], which destroys the copper foils. Several non-destructive transfer processes compatible with continuous production of graphene and carbon thins films have been proposed [242], [243]. The most direct process is the peel-off of polymer/graphene film from the copper [244]–[247], whose effectivity strongly depends on the polymer-graphene adhesion [248]. Other process was proposed by simultaneously applying physical pressure, high temperature and a voltage [249]. On the other hand, the use of liquids which penetrate the interface between graphene and copper are also effective, using hot deionized water [250] or the electrochemical delamination using an electrolysis-like setup [196], [251]–[255].

Here a new delamination process of PMMA/carbon thin films from the copper catalyst is presented, which consists on the use of cold thermal shocks to induce their separation by thermal contractions. The effectivity of the delamination depends upon the polymer characteristics (mainly Young modulus, thermal expansion coefficient and thickness), the thermal gradient during cool down, and the energy adhesion of the carbon film to the copper foil. This process is perfectly compatible with current continuous production systems and roll-to-roll schematics found in the literature [119], [121], [123].

7.3.1. Experimental procedure

Synthesis of carbon thin films by CVD. The synthesis process by CVD is described in Section 6.2, using copper foils of 20×20 mm^2. The synthesis conditions to obtain carbon thin films of different thicknesses were performed (~ 2.5 nm, 5 nm and 20 nm) by using different gas concentrations ($Ar/H_2/C_2H_4$ (sccm) = 500/20/20 for 2.5 minutes, 500/20/20 for 5 minutes, 300/120/120 for 5 minutes).

Polymer application. Poly(methyl-methacrylate) (PMMA; 495PMMA A Resists, Microchem) was directly drop-casted using a micropipette to obtain different PMMA thicknesses (140, 280 and 350 µl which resulted in thickness approximately of 20, 40, 50 µm measuring 10 samples with a digital calliper). Since the drop-casting process does not generate a homogenous PMMA film thickness, which tends to accumulate in the edges of the copper foils due surface tension, a hot press was used to improve the film thickness (120ºC, and 100 kg of pressure). This process also improves the adhesion of the PMMA to the carbon film.

Experiments using polyethylene films of 300 µm thickness were also performed (linear low density polyethylene, Dow), as well as additional ones by using a drop-casting polyurethane solution (TPU) as an adhesive between the carbon film and the polyethylene (2 g of polyurethane pellets on 200 ml of acetone). All the polymers used in these experiments are summarized in the next table.

Table 8 Summary of the preparation process followed to produce polymer films.

	Film production			**Film application**		
Polymer	**Process**	**values**	**thickness**	**Process**	**values**	**thickness**
PMMA	Commercial 5% solution on anisole 495PMMA A, Microchem			drop casting + hot press	140 µl 280 µl 350 µl	~20 µm ~40 µm ~50 µm
PE	Hot press	175ºC 500T	300 µm	hot press	160ºC 100 kg	~300 µm
TPU + PE	PE Hot press	175ºC 500T	300 µm	Drop casting TPU (140 µl) + PE hot press	100ºC 100 kg	~300 µm
	TPU	2 g of TPU pellets on 200 ml of acetone				

Thermal shock delamination. Thermal shocks were carried out on top of cold stainless steel plates (60x40x20mm approximately), by dropping the sample (PMMA/Carbon film/Copper foil) with the copper in contact to the cold surface (**Figure 70**a). Stainless steel plates were cooled down to -160ºC in a liquid N_2 bath and -80ºC using dry ice bricks. Electrical resistance of the transferred films were measured with a multimetre between two copper electrodes separated 18 mm.

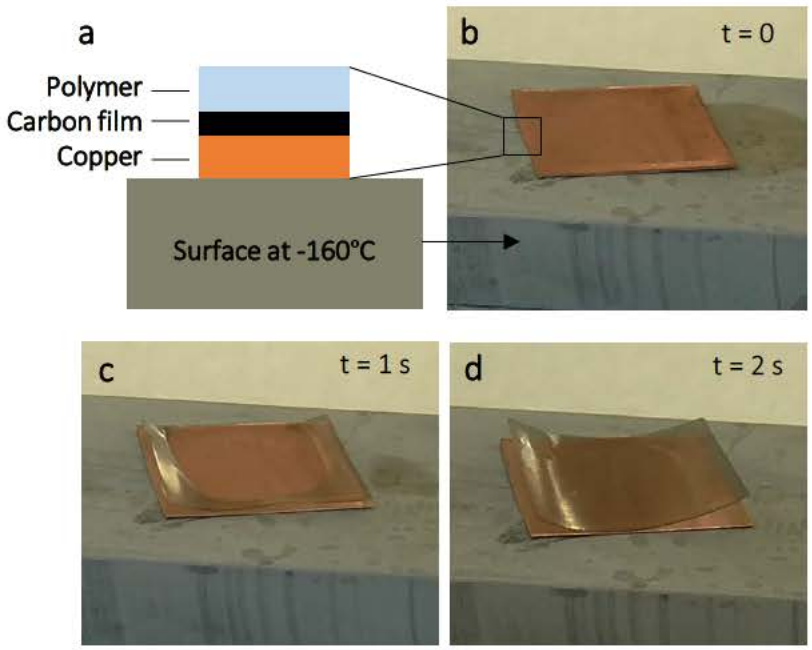

Figure 70 a) Thermal shock delamination process of a PMMA (40 μm)/carbon film (20 nm). b) Interaction of copper with a cold surface (approximately -160°C) at the beginning of the thermal shock. c) Advancing delamination at approximately 1 second, and d) complete delamination of polymer/carbon composite from the copper catalyst at 2 seconds.

7.3.2. Carbon film thickness and autodelamination

Carbon thin films and copper foils are poorly adhered due to their low chemical interaction. As a consequence, the glass-like carbon films spontaneously autodelaminates during cool down right after the CVD from 850°C to room temperature, which is produced by the mismatch between thermal expansion coefficients of amorphous carbon and copper. The resulting autodelamination was observed under the optical microscope and AFM, where ridges were clearly visible on 80-nm-thick carbon films (**Figure 71**a,b). AFM analysis indicated the formation of ridges up to 1,5 μm (peak-to-valley) (**Figure 71**b).

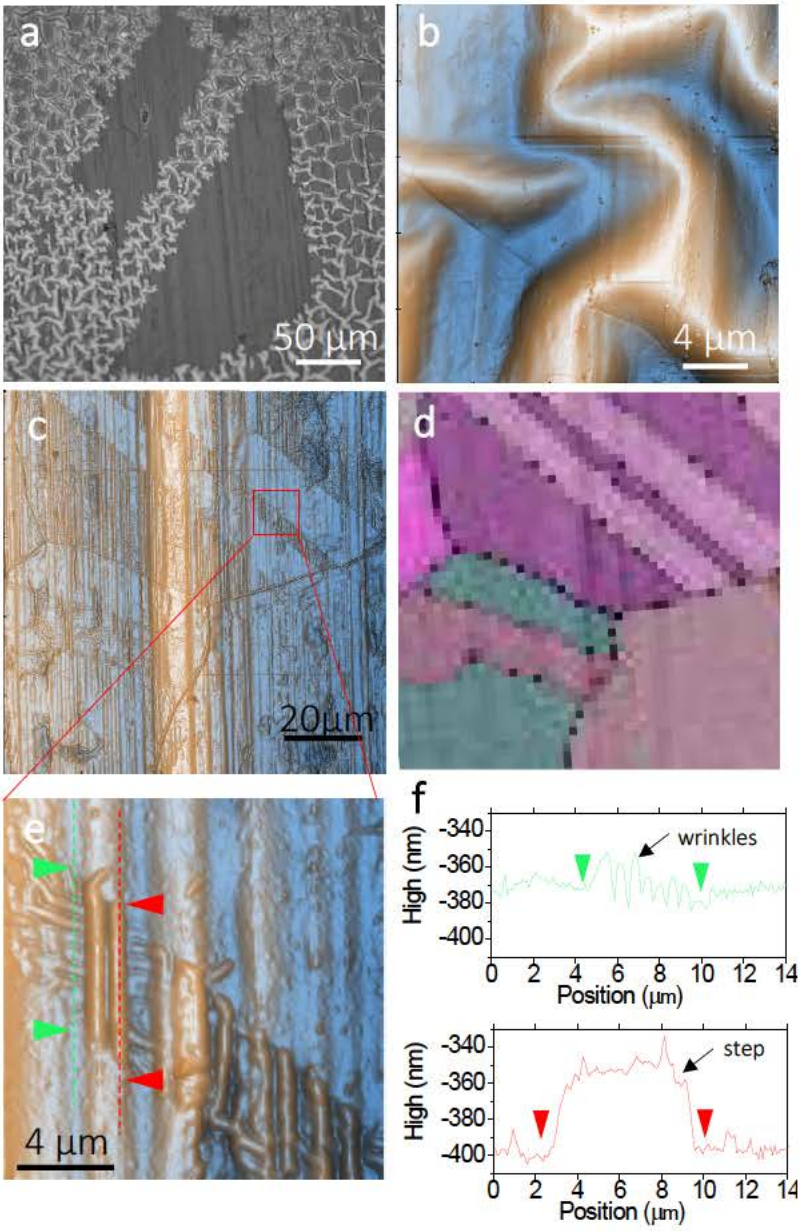

Figure 71 Delamination of the carbon film (~80 nm) deposited on copper foils (optical and AFM images a) and b) respectively). Correlation between the 14-nm-thick carbon film wrinkles (AFM on c, e) and copper crystal orientation (EBSD, d). Wrinkles diminish in the twins inside a copper grain as identified in images c and d.

A similar AFM analysis was performed on as-synthesized thinner carbon films (14-nm-thick synthesis condition on Chapter VI) where ridges were not observable under the optical microscope. A varying roughness of the carbon film (autodelaminated regions) is correlated with the crystal structure of the copper catalyst underneath, identified by electron backscattered diffraction (EBSD). Wrinkles on this sample

(**Figure 71**c) were clearly related to the presence of twins on the copper below (**Figure 71**d). The AFM magnification of **Figure 71**e highlights the wrinkles of about 20 nm between twins (green dashed line) and a step of delaminated carbon film of about 60 nm (red dashed line). These experiments demonstrate the different extent of autodelamination depending on the carbon film thickness.

7.3.3. Transfer assessment and thermal shock parameters

The electrical resistance of delaminated samples by thermal shocks were measured and compared to the copper acid etching transfer baseline (**Figure 72**). Transfer of 20-nm-thick carbon films with the -160ºC thermal shock resulted in an enhancement of the electrical resistance from 1.4 kΩ (baseline) to 1.8 kΩ and 2.3 kΩ when using 20 μm and 40 μm thick PMMA. A better transfer was obtained using 50 μm thick PMMA, which resulted in 1.3 kΩ. Thermal shocks on -80ºC surfaces resulted in 2.7 kΩ, 1.9 kΩ and 2 kΩ by increasing the PMMA film thickness.

Since the 5-nm-thick carbon films are more attached to the copper foil as demonstrated in the last section, they break during the thermal shocks using high thermal gradients (-160ºC). As a consequence, an increase of electrical resistance is observed in those samples, which increased from 3.6 kΩ (baseline) to 13.1 kΩ, 9.9 kΩ and 8.7 kΩ by increasing the PMMA thickness. A more effective transfer was obtained when using low thermal gradients (-80ºC), with values of 5.5 kΩ, 6.2 kΩ and 4.3 kΩ.

Finally, the 2.5-nm-thick carbon films could only be delaminated when using thick PMMA and high temperature gradients (-160ºC), however large areas of carbon film remains attached to the copper foil resulting in a poor transfer.

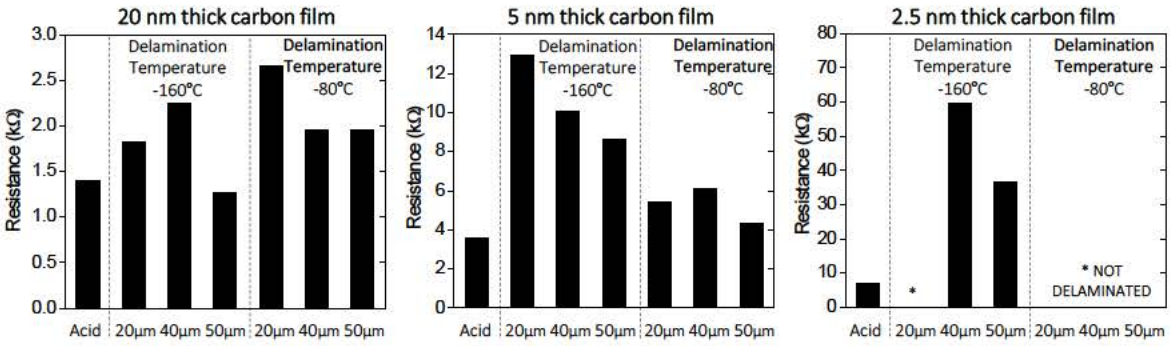

Figure 72 Electrical resistances of transferred samples by thermal shock compared to baseline (copper etching). 20-nm-thick carbon films were effectively transferred to PMMA films regardless the PMMA film thickness and thermal gradient. Transfer of 5-nm-thick carbon films show a dependency on PMMA thickness and thermal gradient, and finally 2.5 nm thick carbon films are poorly or not transferred do to their higher energy of adhesion.

It can be concluded that i) thin carbon films are more difficult to delaminate due to their higher adhesion to copper, which is related to the autodelamination of carbon films right after CVD. ii) Carbon films below 5-nm-thick breaks during the process or are not delaminated and iii) PMMA thick films (50 µm) seems to be more effective during thermal shocks, especially in the case of 5-nm-thick carbon film and high thermal gradients.

A key parameter during mechanical transfer of thin films from CVD copper catalyst is the carbon-to-polymer adhesion. We performed a last experiment on 2.5 nm-thick-carbon films using polyethylene films (300 µm thickness) with/without a polyurethane adhesive, which are known to offer better adhesion to graphene [248]. Carbon films could be transferred even by direct peeling (12 kΩ and 8 kΩ compared to 6.8 kΩ baseline), but a better transfer was obtained on thermal shocks at -160°C (7.3 kΩ 8.2 kΩ). The application of a polyurethane adhesive solution (TPU-PE) seems to improve the transfer of the carbon film compared to PMMA films. Despite polymer-assisted carbon film transfer by thermal shocks is a very fast transfer process and are highly scalable compared to others such as electrochemical delamination, further research has to be done to increase its efficiency, paying special attention to the polymer/carbon adhesion behaviour.

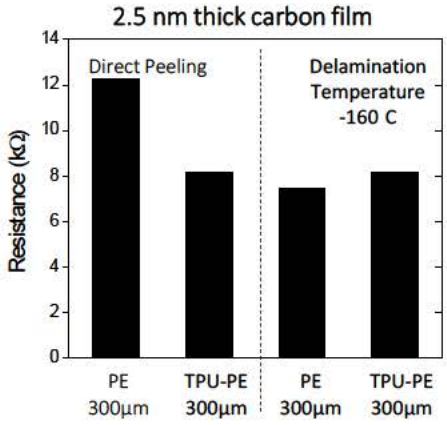

Figure 73 Electrical resistances of transferred samples by thermal shock and direct peeling using polyethylene films (PE) and a polyurethane adhesive solution between the carbon film and polyethylene (TPU-PE). 2.5-nm-thick carbon films can be transferred from copper foils even by direct peeling, and an effective transfer is obtained on thermal shocks at -160°C. The application of a polyurethane adhesive solution seems to improve the transfer of the carbon film.

7.4. Summary

Glass-like carbon films down to 5 nm of thickness (synthesis process explained in Chapter VI), provides an optical transmittance up to 86% of visible light and electrical conductivities up to 10^4 S/m, well above that of amorphous carbon and similar to that of bulk glass-like carbons. Due to the short range crystal order of our carbon films, this performance is far from that provided by highly crystalline and continuous CVD graphene films, thus they are not competitive against graphene in applications where a high conductivity and transparency is demanded.

However, other functional surface-related applications do not demand the high levels of crystallinity provided by graphene, and a short range crystalline order may be enough. In this regard, we have demonstrated the possibility to tune the hydrophobic/hydrophilic nature of our glass-like carbon films, which can be useful as antimicrobial or biocompatible membranes in food processing or water treatment applications. This represent an alternative application of transparent carbon thin films which can provide multifunctionality to superior structures. Two facts make our production process more scalable compared to graphene: the easier and low cost production process of a 5-nm-thick amorphous films compared to one-atom-thick

monocrystalline film, and the possibility to transfer them from the copper catalyst by an ultrafast thermal shock delamination process. These two advantages bring transparent and flexible carbon films close to market whose applications, complementary to graphene films, are yet to be discovered.

8
Conclusions and future work

Carbon is a very versatile element, and is able to form a variety of crystalline and amorphous materials which are currently in an extensive use in engineering. Carbon fibres are a good example of crystalline structures offering outstanding mechanical properties for polymer reinforcement in aerospace applications, as carbon black and glass-like carbons are examples of amorphous carbons used as fillers in the tire industry or as electrodes in electrochemistry. The recent in-depth characterization of graphene [20] has renewed the interest in carbon nanomaterials and related nanostructures which are proposed for a wide variety of applications such as electronics, energy production/storage, biomedical, among others. However, main issues in maintaining carbon nanomaterial properties and performance upon up-scaling, mass production or integration are still to be solved before they can display their expected industrial relevance. For the time being, the cheapest nanocarbon-based materials like carbon nanotube (CNT) powders in batteries, automotive parts and large-area coatings are the first available in the market, while devices requiring highly ordered CNTs (arrays, fibres or films) or graphene films will appear at a longer term.

Nanocarbons with different morphologies and crystallinities can be produced by catalytic chemical vapor deposition (CVD). It consists on the thermal decomposition of hydrocarbons (carbon source) over metal catalysts, and offers high controllability, scalability and adaptability to fabricate on-demand carbon nanomaterials like thin films, fibres, arrays and other highly organized structures. Several schemes were recently proposed demonstrating the continuous synthesis of graphene/polymer composites film at rates of 10 cm/min using copper foils catalysts [119], [121], as well as CNT fibres and forests from iron nanoparticles with similar synthesis rates [75], [115]–[117].

In this thesis, it was proposed the use of a custom-made CVD reactor and commercial bulk metals like powders and foils as catalysts for the production of carbon nanomaterials at large scales. Such a straightforward approach reduces/eliminates the catalyst preparation processes that in some cases requires expensive and hard-to-scale microfabrication techniques. Despite the ease and simplification of the CVD process by using commercial bulk metals, a major challenge was found related to the control of the growing nanostructure since bulk metals evolves under CVD conditions either in composition and morphology. In fact, bulk metals with high carbon solubility may suffer fragmentation, which in some cases resulted beneficial for the in-situ production of metal nanoparticles and growth of nanofibres. On the contrary, metals with low carbon solubility like copper offer a more stable surface, and are more appropriate for the synthesis of carbon thin films. Thus, by selecting the adequate metal catalyst (morphology and composition) and the CVD conditions (gas concentration and temperature) it is possible to produce a wide variety of carbon nanostructures with different morphologies and qualities.

From the point of view of metal-carbon interaction and carbon nanostructure growth mechanism, the design of bulk metal catalysts should take into account the number of alloy elements, the presence of grain boundaries, the carbon solubility and morphology, and the possible formation of new elements and their stability at CVD conditions. A fundamental difference based on catalyst surface stability was demonstrated by the comparative study of pure nickel and $Fe_{64}Ni_{36}$ powders. As a single element, pure nickel surfaces are more stable at CVD conditions (especially at 530ºC and 680ºC) and better withstand the effect of carbon deposition in comparison to $Fe_{64}Ni_{36}$ powders, which suffer fragmentation most likely due the higher density of grain boundaries and the carbide formation. This different behaviour has important implications in the morphology of the carbon fibres produced, since the diameter of nickel catalyst remains constant (1–10 μm) giving rise to fibres of the same diameter, meanwhile the fragmentation of $Fe_{64}Ni_{36}$ particles into nanoparticles leads to the growth of nanofibres. Interestingly, the behaviour of nickel and $Fe_{64}Ni_{36}$ powders converges when synthesis temperature is increased up to 830ºC, at which the enhancement of carbon solubility and diffusivity in the metal leads to graphite inward growth, and the further fragmentation of both nickel and $Fe_{64}Ni_{36}$ powders. These experiments showed that commercially available powders are good candidates

to produce carbon nanomaterials with different morphologies at large scales. Main products are multidirectional ~100 μm-long carbon fibres up to 5 μm in diameter, a wide variety of carbon nanofibres, nanotubes and nanocoils from 50 to 200 nm in diameter and metal-graphite core-shell structures up to 500 nm at yields above 400 (carbon to catalyst mass ratio) after 24h of synthesis. Some of these products are being investigated by our group as fillers for the reinforcement of polymers. As a future research line, the study of the magnetic nature of the metal-graphite core-shell nanoparticles obtained at high temperatures are proposed.

Stainless steel foils were the next catalyst used in this work. As the number of alloy elements is increased in stainless steel, so will the number of possible reactions with carbon, some of which will be harmful for the growth of carbon nanostructures. In addition to iron, which is the element which catalyses the growth on CNTs on stainless steel foils, other elements like chromium, manganese, silicon or oxygen may have important roles. In order to ensure the growth of CNTs, it is of main importance to favour the presence of iron in the stainless steel surface, which showed only to be present after oxidation-reduction pretreatments at 720ºC-780ºC. Higher temperatures favoured the accumulation of other stable elements like chromium, manganese, silicon or oxygen which forms carbides, oxides and spinels at the expense of desired iron. We have demonstrated for the first time the possibility to synthesize and isolate a hierarchical structure consisting on a CNTs array connected to a carbon thin film of about ~100 nm-thick, which simultaneously grew only between 720ºC-780ºC. As a future research line, it is proposed the use of this 3D structure as electrode in energy harvesting and storage applications.

The high interaction between catalyst and carbon can be reduced by selecting metals with low carbon solubility not forming carbides such as copper, which offers a stable surface at CVD conditions. The disadvantage of low interacting metals is that they do not readily dissociate the hydrocarbon during CVD, and amorphous carbon may be deposited instead. In fact, one of the major difficulties found during this work was to tune the gas concentration to enable the adequate deposition rate of a single monolayer graphene in our custom-made CVD reactor. In this regard, longer synthesis with deposition rates above those needed for graphene results in the deposition of amorphous carbon films with controllable thicknesses. By tuning the

gas flow rates from 40–540 sccm and ethylene concentration from 0.04–0.5, we have produced carbon films with controlled thickness from 5–237 nm. It is demonstrated that the carbon film thickness synthesized on copper foils is not only proportional to hydrocarbon concentration in the gas flowing, but it is also inversely proportional to the total flow rate, since it affects the residence time of carbon containing molecules and the probability of deposition.

Among all the materials produced during this thesis, we selected carbon thin films as the material offering more possibilities. Several facts make the production of our thickness-controlled carbon films competitive against graphene; their larger thickness makes them easier to visualize and to manipulate, they are easier to replicate due to their amorphous nature, and they are partially delaminated right after the CVD process, which helps their further transfer into a polymer film. We produced transparent composites films (carbon film/PMMA) which showed sheet resistances of R_s=7.836 ± 1.500 kΩ/□ and optical transmittances of T=85,7% (for 5-nm-thick carbon film) and R_s=4.298 ± 0.140 kΩ/□ at T=58.65% (for 18-nm-thick carbon film). These values are equivalent to electrical conductivities of $8.7 \times 10^3 – 2.5 \times 10^4$ S/m, which are lower than graphene (~$3 \cdot 10^5$ S/m) but similar to bulk glass-like carbon or pyrolysed photoresist thin films, and well above amorphous carbons (10^2 S/m). This performance is similar to that obtained in carbon-based nanocomposites using liquid exfoliated or reduced graphene oxides, but far away from current conductive oxides (ZnO, SnO and ITO) so they are not suitable alternatives as transparent electrodes in flat displays or thin-film solar cells.

Then, we characterized the surface wettability of 5-nm-thick carbon films, which is an interesting property in food processing, wastewater treatment or biopolymer degradation applications. In this regard, we have demonstrated that the surface wettability of 5-nm-thick carbon films can be tuned under ultraviolet light irradiation, which at the same time triggered the surface colonization by Escherichia Coli cells as demonstrated in our recent work [238]. Finally and related to the scalable production of carbon thin films, we have demonstrated the highly efficient carbon film polymer-assisted transfer process by ultrafast thermal shocks, by selecting the proper polymer and thermal gradient. This result is of major importance and represents a clear advantage compared to graphene production,

whose large scale transfer is an unsolved issue at the time of this work. We are currently simulating the delamination process to better understand and design scalable future processes. As a future research line, we stress here the possibilities arising from the use of carbon films with high density of defects, which already have been demonstrated as flexible neuroelectronic implants for dopamine sensing.

The study presented here demonstrates the production of different carbon nanomaterials by using four commercially available bulk metals as catalysts. A large number of metal are available in the market that, together with the use of different CVD gas concentrations and temperatures opens a wide window of possibilities to produce on-demand carbon nanomaterials.

References

[1] A. Krueger, *Carbon Materials and Nanotechnology*. Wiley-VCH Verlag GmbH & Co. KGaA, 2010.

[2] P. J. F. Harris, "New Perspectives on the Structure of Graphitic Carbons," *Critical Reviews in Solid State and Materials Sciences*, vol. 30, no. 4, pp. 235–253, Oct. 2005.

[3] G. Jenkins and K. Kawamura, "Structure of glassy carbon," *Nature*, vol. 231, pp. 175–176, 1971.

[4] M. F. L. De Volder, S. H. Tawfick, R. H. Baughman, and A. J. Hart, "Carbon Nanotubes: Present and Future Commercial Applications," *Science*, vol. 339, no. 6119, pp. 535–539, Feb. 2013.

[5] A. C. Ferrari *et al.*, "Science and technology roadmap for graphene, related two-dimensional crystals, and hybrid systems," *Nanoscale*, vol. 7, no. 11, pp. 4598–4810, 2015.

[6] S. Iijima, "Helical microtubules of graphitic carbon," *Nature*, vol. 354, no. 6348, pp. 56–58, Nov. 1991.

[7] L. Radushkevich and V. Lukyanovich, "O strukture ugleroda, obrazujucegosja pri termiceskom razlozenii okisi ugleroda na zeleznom kontakte," *Zurn Fisic Chim*, vol. 26, pp. 88–95, 1952.

[8] Y. Gogotsi, Ed., *Carbon nanomaterials*. Boca Raton, Fla.: CRC/Taylor & Francis, 2006.

[9] X. Wang *et al.*, "Fabrication of Ultralong and Electrically Uniform Single-Walled Carbon Nanotubes on Clean Substrates," *Nano Letters*, vol. 9, no. 9, pp. 3137–3141, Sep. 2009.

[10] T. W. Ebbesen, H. J. Lezec, H. Hiura, J. W. Bennett, H. F. Ghaemi, and T. Thio, "Electrical conductivity of individual carbon nanotubes," *Nature*, vol. 382, no. 6586, pp. 54–56, Jul. 1996.

[11] A. V. Savin, B. Hu, and Y. S. Kivshar, "Thermal conductivity of single-walled carbon nanotubes," *Physical Review B*, vol. 80, no. 19, Nov. 2009.

[12] P. Kim, L. Shi, A. Majumdar, and P. L. McEuen, "Thermal Transport Measurements of Individual Multiwalled Nanotubes," *Physical Review Letters*, vol. 87, no. 21, Oct. 2001.

[13] E. W. Wong, P. E. Sheehan, and C. M. Lieber, "Nanobeam Mechanics: Elasticity, Strength, and Toughness of Nanorods and Nanotubes," *Science*, vol. 277, no. 5334, p. 1971, Sep. 1997.

[14] M.-F. Yu, O. Lourie, M. J. Dyer, K. Moloni, T. F. Kelly, and R. S. Ruoff, "Strength and Breaking Mechanism of Multiwalled Carbon Nanotubes Under Tensile Load," *Science*, vol. 287, no. 5453, p. 637, Jan. 2000.

[15] S. Xie, W. Li, Z. Pan, B. Chang, and L. Sun, "Mechanical and physical properties on carbon nanotube," *Journal of Physics and Chemistry of solids*, vol. 61, no. 7, pp. 1153–1158, 2000.

[16] I. Martin-Gullon, J. Vera, J. A. Conesa, J. L. González, and C. Merino, "Differences between carbon nanofibers produced using Fe and Ni catalysts in a floating catalyst reactor," *Carbon*, vol. 44, no. 8, pp. 1572–1580, Jul. 2006.

[17] T. Ozkan, M. Naraghi, and I. Chasiotis, "Mechanical properties of vapor grown carbon nanofibers," *Carbon*, vol. 48, no. 1, pp. 239–244, Jan. 2010.

[18] D. Sebastián, A. G. Ruiz, I. Suelves, R. Moliner, and M. J. Lázaro, "On the importance of the structure in the electrical conductivity of fishbone carbon nanofibers," *Journal of Materials Science*, vol. 48, no. 4, pp. 1423–1435, Feb. 2013.
[19] E. Mayhew and V. Prakash, "Thermal conductivity of individual carbon nanofibers," *Carbon*, vol. 62, pp. 493–500, Oct. 2013.
[20] K. S. Novoselov, "Electric Field Effect in Atomically Thin Carbon Films," *Science*, vol. 306, no. 5696, pp. 666–669, Oct. 2004.
[21] J.-H. Chen, C. Jang, S. Xiao, M. Ishigami, and M. S. Fuhrer, "Intrinsic and extrinsic performance limits of graphene devices on SiO2," *Nat Nano*, vol. 3, no. 4, pp. 206–209, Apr. 2008.
[22] K. I. Bolotin *et al.*, "Ultrahigh electron mobility in suspended graphene," *Solid State Communications*, vol. 146, no. 9–10, pp. 351–355, Jun. 2008.
[23] Q. Bao *et al.*, "Atomic-layer graphene as a saturable absorber for ultrafast pulsed lasers," *Advanced Functional Materials*, vol. 19, no. 19, pp. 3077–3083, 2009.
[24] J. S. Bunch *et al.*, "Electromechanical Resonators from Graphene Sheets," *Science*, vol. 315, no. 5811, pp. 490–493, Jan. 2007.
[25] A. A. Balandin *et al.*, "Superior Thermal Conductivity of Single-Layer Graphene," *Nano Letters*, vol. 8, no. 3, pp. 902–907, Mar. 2008.
[26] R. R. Nair *et al.*, "Fine Structure Constant Defines Visual Transparency of Graphene," *Science*, vol. 320, no. 5881, pp. 1308–1308, Jun. 2008.
[27] J. Robertson, "Diamond-like amorphous carbon," *Materials Science and Engineering: R: Reports*, vol. 37, no. 4, pp. 129–281, 2002.
[28] M. Shamsa, W. L. Liu, A. A. Balandin, C. Casiraghi, W. I. Milne, and A. C. Ferrari, "Thermal conductivity of diamond-like carbon films," *Applied Physics Letters*, vol. 89, no. 16, p. 161921, 2006.
[29] R. U. R. Sagar, X. Zhang, C. Xiong, and Y. Yu, "Semiconducting amorphous carbon thin films for transparent conducting electrodes," *Carbon*, vol. 76, pp. 64–70, Sep. 2014.
[30] M. P. Manoharan, H. Lee, R. Rajagopalan, H. C. Foley, and M. A. Haque, "Elastic Properties of 4–6 nm-thick Glassy Carbon Thin Films," *Nanoscale Research Letters*, vol. 5, no. 1, pp. 14–19, Jan. 2010.
[31] P. J. F. Harris †, "Fullerene-related structure of commercial glassy carbons," *Philosophical Magazine*, vol. 84, no. 29, pp. 3159–3167, Oct. 2004.
[32] Z. Zhao *et al.*, "Nanoarchitectured materials composed of fullerene-like spheroids and disordered graphene layers with tunable mechanical properties," *Nature Communications*, vol. 6, p. 6212, Feb. 2015.
[33] K. R. Paton *et al.*, "Scalable production of large quantities of defect-free few-layer graphene by shear exfoliation in liquids," *Nature Materials*, vol. 13, no. 6, pp. 624–630, Apr. 2014.
[34] M. Garcia-Hernandez and J. Coleman, "Materials science of graphene: a flagship perspective," *2D Materials*, vol. 3, no. 1, p. 10401, 2016.
[35] P.-C. Ma, N. A. Siddiqui, G. Marom, and J.-K. Kim, "Dispersion and functionalization of carbon nanotubes for polymer-based nanocomposites: A review," *Composites Part A: Applied Science and Manufacturing*, vol. 41, no. 10, pp. 1345–1367, Oct. 2010.
[36] J. R. Potts, D. R. Dreyer, C. W. Bielawski, and R. S. Ruoff, "Graphene-based polymer nanocomposites," *Polymer*, vol. 52, no. 1, pp. 5–25, Jan. 2011.

[37] R. H. Hurt, M. Monthioux, and A. Kane, "Toxicology of carbon nanomaterials: Status, trends, and perspectives on the special issue," *Carbon*, vol. 44, no. 6, pp. 1028–1033, May 2006.
[38] J. Zhang *et al.*, "Carbon science in 2016: Status, challenges and perspectives," *Carbon*, vol. 98, pp. 708–732, Mar. 2016.
[39] J. J. Vilatela and D. Eder, "Nanocarbon Composites and Hybrids in Sustainability: A Review," *ChemSusChem*, vol. 5, no. 3, pp. 456–478, Mar. 2012.
[40] K. Ellmer, "Past achievements and future challenges in the development of optically transparent electrodes," *Nature Photonics*, vol. 6, no. 12, pp. 809–817, Nov. 2012.
[41] F. Bonaccorso, Z. Sun, T. Hasan, and A. C. Ferrari, "Graphene photonics and optoelectronics," *Nature Photonics*, vol. 4, no. 9, pp. 611–622, Sep. 2010.
[42] S. De and J. N. Coleman, "Are There Fundamental Limitations on the Sheet Resistance and Transmittance of Thin Graphene Films?," *ACS Nano*, vol. 4, no. 5, pp. 2713–2720, May 2010.
[43] S. Bae *et al.*, "Roll-to-roll production of 30-inch graphene films for transparent electrodes," *Nature Nanotechnology*, vol. 5, no. 8, pp. 574–578, Aug. 2010.
[44] "Graphene products: introduction and market status."
[45] A. Centeno *et al.*, "Graphene for tough and electroconductive alumina ceramics," *Journal of the European Ceramic Society*, vol. 33, no. 15–16, pp. 3201–3210, Dec. 2013.
[46] "www.fastcapsystems.com/ ,FastCap Systems Corporation." .
[47] D. J. Preston, D. L. Mafra, N. Miljkovic, J. Kong, and E. N. Wang, "Scalable Graphene Coatings for Enhanced Condensation Heat Transfer," *Nano Letters*, vol. 15, no. 5, pp. 2902–2909, May 2015.
[48] O. J. . Schueller, S. T. Brittain, and G. M. Whitesides, "Fabrication of glassy carbon microstructures by soft lithography," *Sensors and Actuators A: Physical*, vol. 72, no. 2, pp. 125–139, Jan. 1999.
[49] Y. Koval, A. Geworski, K. Gieb, I. Lazareva, and P. Müller, "Fabrication and characterization of glassy carbon membranes," *Journal of Vacuum Science & Technology B, Nanotechnology and Microelectronics: Materials, Processing, Measurement, and Phenomena*, vol. 32, no. 4, p. 42001, Jul. 2014.
[50] R. Rajagopalan, A. Ponnaiyan, P. J. Mankidy, A. W. Brooks, B. Yi, and H. C. Foley, "Molecular sieving platinum nanoparticle catalysts kinetically frozen in nanoporous carbon," *Chemical Communications*, no. 21, p. 2498, 2004.
[51] A. Merritt, R. Rajagopalan, and H. C. Foley, "High performance nanoporous carbon membranes for air separation," *Carbon*, vol. 45, no. 6, pp. 1267–1278, May 2007.
[52] J. J. VanDersarl, A. Mercanzini, and P. Renaud, "Integration of 2D and 3D Thin Film Glassy Carbon Electrode Arrays for Electrochemical Dopamine Sensing in Flexible Neuroelectronic Implants," *Advanced Functional Materials*, vol. 25, no. 1, pp. 78–84, Jan. 2015.
[53] P. Simon and Y. Gogotsi, "Capacitive Energy Storage in Nanostructured Carbon–Electrolyte Systems," *Accounts of Chemical Research*, vol. 46, no. 5, pp. 1094–1103, May 2013.
[54] L. Zhang *et al.*, "Porous 3D graphene-based bulk materials with exceptional high surface area and excellent conductivity for supercapacitors," *Scientific Reports*, vol. 3, Mar. 2013.

[55] M. Yudasaka, T. Komatsu, T. Ichihashi, and S. Iijima, "Single-wall carbon nanotube formation by laser ablation using double-targets of carbon and metal," *Chemical physics letters*, vol. 278, no. 1, pp. 102–106, 1997.
[56] W. Z. Li *et al.*, "Large-Scale Synthesis of Aligned Carbon Nanotubes," *Science*, vol. 274, no. 5293, pp. 1701–1703, Dec. 1996.
[57] A. J. Hart, "Chemical, mechanical, and thermal control of substrate-bound carbon nanotube growth," Massachusetts Institute of Technology, Cambridge, MA, USA, 2006.
[58] Y. Yan *et al.*, "Carbon nanotube catalysts: recent advances in synthesis, characterization and applications," *Chem. Soc. Rev.*, vol. 44, no. 10, pp. 3295–3346, 2015.
[59] J. P. Gore and A. Sane, "Flame synthesis of carbon nanotubes," *Carbon Nanotubes-Synthesis, Characterization, Applications*, no. 1, p. 16801, 2011.
[60] K. S. Novoselov *et al.*, "Two-dimensional atomic crystals," *Proceedings of the National Academy of Sciences of the United States of America*, vol. 102, no. 30, pp. 10451–10453, 2005.
[61] H. O. Pierson and H. O. Pierson, *Handbook of chemical vapor deposition*, 2nd ed. Norwich, NY: Noyes Publications, 1999.
[62] V. Jourdain and C. Bichara, "Current understanding of the growth of carbon nanotubes in catalytic chemical vapour deposition," *Carbon*, vol. 58, pp. 2–39, Jul. 2013.
[63] S. Hofmann, G. Csányi, A. C. Ferrari, M. C. Payne, and J. Robertson, "Surface Diffusion: The Low Activation Energy Path for Nanotube Growth," *Physical Review Letters*, vol. 95, no. 3, Jul. 2005.
[64] J. Robertson, "Heterogeneous catalysis model of growth mechanisms of carbon nanotubes, graphene and silicon nanowires," *Journal of Materials Chemistry*, vol. 22, no. 37, p. 19858, 2012.
[65] A. Shaikjee and N. J. Coville, "The role of the hydrocarbon source on the growth of carbon materials," *Carbon*, vol. 50, no. 10, pp. 3376–3398, Aug. 2012.
[66] G. A. López and E. J. Mittemeijer, "The solubility of C in solid Cu," *Scripta Materialia*, vol. 51, no. 1, pp. 1–5, Jul. 2004.
[67] K. Natesan and T. F. Kassner, "Thermodynamics of Carbon in Nickel, Iron-Nickel and Iron-Chromium-Nickel Alloys," *Metallurgical Transactions*, vol. 4, no. 11, pp. 2557–2566, 1973.
[68] J. Lahiri, T. S Miller, A. J Ross, L. Adamska, I. I. Oleynik, and M. Batzill, "Graphene growth and stability at nickel surfaces," *New Journal of Physics*, vol. 13, no. 2, p. 25001, Feb. 2011.
[69] R. Addou, A. Dahal, P. Sutter, and M. Batzill, "Monolayer graphene growth on Ni(111) by low temperature chemical vapor deposition," *Applied Physics Letters*, vol. 100, no. 2, p. 21601, 2012.
[70] L. L. Patera *et al.*, "*In Situ* Observations of the Atomistic Mechanisms of Ni Catalyzed Low Temperature Graphene Growth," *ACS Nano*, vol. 7, no. 9, pp. 7901–7912, Sep. 2013.
[71] H. K. D. H. Bhadeshia and R. W. K. Honeycombe, *Steels: microstructure and properties*, 3rd ed. Amsterdam ; Boston: Elsevier, Butterworth-Heinemann, 2006.
[72] C. Mattevi, H. Kim, and M. Chhowalla, "A review of chemical vapour deposition of graphene on copper," *J. Mater. Chem.*, vol. 21, no. 10, pp. 3324–3334, 2011.

[73] A. J. Hart, A. H. Slocum, and L. Royer, "Growth of conformal single-walled carbon nanotube films from Mo/Fe/Al2O3 deposited by electron beam evaporation," *Carbon*, vol. 44, no. 2, pp. 348–359, Feb. 2006.

[74] M. S. Motta, A. Moisala, I. A. Kinloch, and A. H. Windle, "The Role of Sulphur in the Synthesis of Carbon Nanotubes by Chemical Vapour Deposition at High Temperatures," *Journal of Nanoscience and Nanotechnology*, vol. 8, no. 5, pp. 2442–2449, May 2008.

[75] V. Reguero, B. Alemán, B. Mas, and J. J. Vilatela, "Controlling Carbon Nanotube Type in Macroscopic Fibers Synthesized by the Direct Spinning Process," *Chemistry of Materials*, vol. 26, no. 11, pp. 3550–3557, Jun. 2014.

[76] B. Mas *et al.*, "Group 16 elements control the synthesis of continuous fibers of carbon nanotubes," *Carbon*, vol. 101, pp. 458–464, May 2016.

[77] S. Helveg *et al.*, "Atomic-scale imaging of carbon nanofibre growth," *Nature*, vol. 427, no. 6973, pp. 426–429, Jan. 2004.

[78] S. Hofmann *et al.*, "In situ Observations of Catalyst Dynamics during Surface-Bound Carbon Nanotube Nucleation," *Nano Letters*, vol. 7, no. 3, pp. 602–608, Mar. 2007.

[79] A. Gohier, C. P. Ewels, T. M. Minea, and M. A. Djouadi, "Carbon nanotube growth mechanism switches from tip- to base-growth with decreasing catalyst particle size," *Carbon*, vol. 46, no. 10, pp. 1331–1338, Aug. 2008.

[80] X. Lepró, M. D. Lima, and R. H. Baughman, "Spinnable carbon nanotube forests grown on thin, flexible metallic substrates," *Carbon*, vol. 48, no. 12, pp. 3621–3627, Oct. 2010.

[81] A. Moisala, A. G. Nasibulin, and E. I. Kauppinen, "The role of metal nanoparticles in the catalytic production of single-walled carbon - a review," *Journal of Physics: Condensed Matter*, vol. 15, no. 42, pp. 3011–3035, 2003.

[82] C. T. Wirth *et al.*, "The Phase of Iron Catalyst Nanoparticles during Carbon Nanotube Growth," *Chemistry of Materials*, vol. 24, no. 24, pp. 4633–4640, Dec. 2012.

[83] Z. He, J.-L. Maurice, A. Gohier, C. S. Lee, D. Pribat, and C. S. Cojocaru, "Iron Catalysts for the Growth of Carbon Nanofibers: Fe, Fe $_3$ C or Both?," *Chemistry of Materials*, vol. 23, no. 24, pp. 5379–5387, Dec. 2011.

[84] M. Kumar and Y. Ando, *Carbon nanotube synthesis and growth mechanism*. INTECH Open Access Publisher, 2011.

[85] K. P. De Jong and J. W. Geus, "Carbon Nanofibers: Catalytic Synthesis and Applications," *Catalysis Reviews*, vol. 42, no. 4, pp. 481–510, Nov. 2000.

[86] G.-B. Zheng, K. Kouda, H. Sano, Y. Uchiyama, Y.-F. Shi, and H.-J. Quan, "A model for the structure and growth of carbon nanofibers synthesized by the CVD method using nickel as a catalyst," *Carbon*, vol. 42, no. 3, pp. 635–640, 2004.

[87] A. V. Melechko *et al.*, "Control of carbon nanostructure: From nanofiber toward nanotube and back," *Journal of Applied Physics*, vol. 102, no. 7, p. 74314, 2007.

[88] J. H. Xia, X. Jiang, C. L. Jia, and C. Dong, "Hexahedral nanocementites catalyzing the growth of carbon nanohelices," *Applied Physics Letters*, vol. 92, no. 6, p. 63121, 2008.

[89] H. Shiozawa *et al.*, "Microscopic insight into the bilateral formation of carbon spirals from a symmetric iron core," *Scientific Reports*, vol. 3, May 2013.

[90] G. E. Begtrup *et al.*, "Facets of nanotube synthesis: High-resolution transmission electron microscopy study and density functional theory calculations," *Physical Review B*, vol. 79, no. 20, May 2009.
[91] J. H. Xia, X. Jiang, and C. L. Jia, "The size effect of catalyst on the growth of helical carbon nanofibers," *Applied Physics Letters*, vol. 95, no. 22, p. 223110, 2009.
[92] J.-L. Maurice, D. Pribat, Z. He, G. Patriarche, and C. S. Cojocaru, "Catalyst faceting during graphene layer crystallization in the course of carbon nanofiber growth," *Carbon*, vol. 79, pp. 93–102, Nov. 2014.
[93] B. Yu, S. Wang, Q. Zhang, Y. He, H. Huang, and J. Zou, "Ni $_3$ C-assisted growth of carbon nanofibres 300 °C by thermal CVD," *Nanotechnology*, vol. 25, no. 32, p. 325602, Aug. 2014.
[94] X. Duan, J. Ji, G. Qian, X. Zhou, and D. Chen, "Recent advances in synthesis of reshaped Fe and Ni particles at the tips of carbon nanofibers and their catalytic applications," *Catalysis Today*, vol. 249, pp. 2–11, Jul. 2015.
[95] B. Yu *et al.*, "Temperature-dependent chemical state of the nickel catalyst for the growth of carbon nanofibers," *Carbon*, vol. 96, pp. 904–910, Jan. 2016.
[96] X. Li *et al.*, "Large-Area Synthesis of High-Quality and Uniform Graphene Films on Copper Foils," *Science*, vol. 324, no. 5932, pp. 1312–1314, Jun. 2009.
[97] K. Celebi *et al.*, "Evolutionary Kinetics of Graphene Formation on Copper," *Nano Letters*, vol. 13, no. 3, pp. 967–974, Mar. 2013.
[98] R. S. Weatherup, B. Dlubak, and S. Hofmann, "Kinetic Control of Catalytic CVD for High-Quality Graphene at Low Temperatures," *ACS Nano*, vol. 6, no. 11, pp. 9996–10003, Nov. 2012.
[99] A. Cabrero-Vilatela, R. S. Weatherup, P. Braeuninger-Weimer, S. Caneva, and S. Hofmann, "Towards a general growth model for graphene CVD on transition metal catalysts," *Nanoscale*, vol. 8, no. 4, pp. 2149–2158, 2016.
[100] R. S. Weatherup *et al.*, "Interdependency of Subsurface Carbon Distribution and Graphene–Catalyst Interaction," *Journal of the American Chemical Society*, vol. 136, no. 39, pp. 13698–13708, Oct. 2014.
[101] Y. Hao *et al.*, "The Role of Surface Oxygen in the Growth of Large Single-Crystal Graphene on Copper," *Science*, vol. 342, no. 6159, pp. 720–723, Nov. 2013.
[102] J. Jang *et al.*, "Low-temperature-grown continuous graphene films from benzene by chemical vapor deposition at ambient pressure," *Scientific Reports*, vol. 5, p. 17955, Dec. 2015.
[103] S. M. Kim *et al.*, "The effect of copper pre-cleaning on graphene synthesis," *Nanotechnology*, vol. 24, no. 36, p. 365602, Sep. 2013.
[104] J. D. Wood, S. W. Schmucker, A. S. Lyons, E. Pop, and J. W. Lyding, "Effects of Polycrystalline Cu Substrate on Graphene Growth by Chemical Vapor Deposition," *Nano Letters*, vol. 11, no. 11, pp. 4547–4554, Nov. 2011.
[105] G. H. Han *et al.*, "Influence of Copper Morphology in Forming Nucleation Seeds for Graphene Growth," *Nano Letters*, vol. 11, no. 10, pp. 4144–4148, Oct. 2011.
[106] "Nanomaterial Suppliers, www.nanowerk.com/nanotechnology/nanomaterial/suppliers_plist.php?subcat1=cnt." .
[107] "Graphene Manufacturers and Suppliers, www.nanowerk.com/graphene_manufacturers_and_suppliers.php."

[108] S. S. Wicks, R. G. de Villoria, and B. L. Wardle, "Interlaminar and intralaminar reinforcement of composite laminates with aligned carbon nanotubes," *Composites Science and Technology*, vol. 70, no. 1, pp. 20–28, Jan. 2010.
[109] M. J. Bronikowski, "Use of refractory-metal diffusion inhibitors to slow Ostwald ripening of catalytic metal particles: A route to ultra-long Carbon Nanotubes (CNT)," *Carbon*, vol. 107, pp. 297–303, Oct. 2016.
[110] E. R. Meshot, D. L. Plata, S. Tawfick, Y. Zhang, E. A. Verploegen, and A. J. Hart, "Engineering Vertically Aligned Carbon Nanotube Growth by Decoupled Thermal Treatment of Precursor and Catalyst," *ACS Nano*, vol. 3, no. 9, pp. 2477–2486, Sep. 2009.
[111] A. Ismach *et al.*, "Direct Chemical Vapor Deposition of Graphene on Dielectric Surfaces," *Nano Letters*, vol. 10, no. 5, pp. 1542–1548, May 2010.
[112] H. Ago *et al.*, "Epitaxial Chemical Vapor Deposition Growth of Single-Layer Graphene over Cobalt Film Crystallized on Sapphire," *ACS Nano*, vol. 4, no. 12, pp. 7407–7414, Dec. 2010.
[113] M. T. Pettes, H. Ji, R. S. Ruoff, and L. Shi, "Thermal Transport in Three-Dimensional Foam Architectures of Few-Layer Graphene and Ultrathin Graphite," *Nano Letters*, vol. 12, no. 6, pp. 2959–2964, Jun. 2012.
[114] M. Zhang, "Multifunctional Carbon Nanotube Yarns by Downsizing an Ancient Technology," *Science*, vol. 306, no. 5700, pp. 1358–1361, Nov. 2004.
[115] J. J. Vilatela Garcia, "Structure, Properties and Treatments of Carbon Nanotube Fibres (doctoral thesis).," 2009.
[116] R. Guzmán de Villoria, S. L. Figueredo, A. J. Hart, S. A. Steiner III, A. H. Slocum, and B. L. Wardle, "High-yield growth of vertically aligned carbon nanotubes on a continuously moving substrate," *Nanotechnology*, vol. 20, no. 40, p. 405611, Oct. 2009.
[117] R. Guzmán de Villoria, A. J. Hart, and B. L. Wardle, "Continuous High-Yield Production of Vertically Aligned Carbon Nanotubes on 2D and 3D Substrates," *ACS Nano*, vol. 5, no. 6, pp. 4850–4857, Jun. 2011.
[118] E. S. Polsen, M. Bedewy, and A. J. Hart, "Decoupled Control of Carbon Nanotube Forest Density and Diameter by Continuous-Feed Convective Assembly of Catalyst Particles," *Small*, vol. 9, no. 15, pp. 2564–2575, Aug. 2013.
[119] T. Hesjedal, "Continuous roll-to-roll growth of graphene films by chemical vapor deposition," *Applied Physics Letters*, vol. 98, no. 13, p. 133106, 2011.
[120] T. Yamada, M. Ishihara, J. Kim, M. Hasegawa, and S. Iijima, "A roll-to-roll microwave plasma chemical vapor deposition process for the production of 294mm width graphene films at low temperature," *Carbon*, vol. 50, no. 7, pp. 2615–2619, Jun. 2012.
[121] E. S. Polsen, D. Q. McNerny, B. Viswanath, S. W. Pattinson, and A. John Hart, "High-speed roll-to-roll manufacturing of graphene using a concentric tube CVD reactor," *Scientific Reports*, vol. 5, p. 10257, May 2015.
[122] T. Kobayashi *et al.*, "Production of a 100-m-long high-quality graphene transparent conductive film by roll-to-roll chemical vapor deposition and transfer process," *Applied Physics Letters*, vol. 102, no. 2, p. 23112, 2013.
[123] B. Deng *et al.*, "Roll-to-Roll Encapsulation of Metal Nanowires between Graphene and Plastic Substrate for High-Performance Flexible Transparent Electrodes," *Nano Letters*, vol. 15, no. 6, pp. 4206–4213, Jun. 2015.

[124] X.-H. Zhong *et al.*, "Continuous Multilayered Carbon Nanotube Yarns," *Advanced Materials*, vol. 22, no. 6, pp. 692–696, Feb. 2010.
[125] R. T. K. Baker, M. S. Kim, A. Chambers, C. Park, and N. M. Rodriguez, "The relationship between metal particle morphology and the structural characteristics of carbon deposits," *Studies in Surface Science and Catalysis*, vol. 111, pp. 99–109, 1997.
[126] C. E. Baddour, D. C. Upham, and J.-L. Meunier, "Direct and repetitive growth cycles of carbon nanotubes on stainless steel particles by chemical vapor deposition in a fluidized bed," *Carbon*, vol. 48, no. 9, pp. 2652–2656, Aug. 2010.
[127] X. H. Nguyen, Y. B. Lee, C. H. Lee, and D.-S. Lim, "Synthesis of sea urchin-like particles of carbon nanotubes directly grown on stainless steel cores and their effect on the mechanical properties of polymer composites," *Carbon*, vol. 48, no. 10, pp. 2910–2916, Aug. 2010.
[128] N. Sano, Y. Hori, S. Yamamoto, and H. Tamon, "A simple oxidation–reduction process for the activation of a stainless steel surface to synthesize multi-walled carbon nanotubes and its application to phenol degradation in water," *Carbon*, vol. 50, no. 1, pp. 115–122, Jan. 2012.
[129] C. E. Baddour and J.-L. Meunier, "Carbon Nanotube Synthesis on Stainless Steel for use in a Nanotube-Titanium Nitride Nanocomposite," in *Nanotechnology, 2008. NANO'08. 8th IEEE Conference on*, 2008, pp. 752–755.
[130] C. E. Baddour, F. Fadlallah, D. Nasuhoglu, R. Mitra, L. Vandsburger, and J.-L. Meunier, "A simple thermal CVD method for carbon nanotube synthesis on stainless steel 304 without the addition of an external catalyst," *Carbon*, vol. 47, no. 1, pp. 313–318, Jan. 2009.
[131] R. L. Vander Wal and L. J. Hall, "Carbon nanotube synthesis upon stainless steel meshes," *Carbon*, vol. 41, no. 4, pp. 659–672, Jan. 2003.
[132] V. Martínez-Hansen, N. Latorre, C. Royo, E. Romeo, E. García-Bordejé, and A. Monzón, "Development of aligned carbon nanotubes layers over stainless steel mesh monoliths," *Catalysis Today*, vol. 147, pp. S71–S75, Sep. 2009.
[133] C. Masarapu and B. Wei, "Direct Growth of Aligned Multiwalled Carbon Nanotubes on Treated Stainless Steel Substrates," *Langmuir*, vol. 23, no. 17, pp. 9046–9049, Aug. 2007.
[134] N. Sabeti Nejad, M. M. Larijani, M. Ghoranneviss, P. Balashabadi, and A. Shokouhy, "Direct growth of carbon nanotubes on Ar ion bombarded AISI 304 stainless steel substrates," *Surface and Coatings Technology*, vol. 203, no. 17–18, pp. 2510–2513, Jun. 2009.
[135] M. Hashempour, A. Vicenzo, F. Zhao, and M. Bestetti, "Direct growth of MWCNTs on 316 stainless steel by chemical vapor deposition: Effect of surface nano-features on CNT growth and structure," *Carbon*, vol. 63, pp. 330–347, Nov. 2013.
[136] N. Sano, T. Kodama, and H. Tamon, "Direct synthesis of carbon nanotubes on stainless steel electrode for enhanced catalyst efficiency in a glucose fuel cell," *Carbon*, vol. 55, pp. 365–368, Apr. 2013.
[137] M. Karwa, Z. Iqbal, and S. Mitra, "Scaled-up self-assembly of carbon nanotubes inside long stainless steel tubing," *Carbon*, vol. 44, no. 7, pp. 1235–1242, Jun. 2006.
[138] N. Hordy, N.-Y. Mendoza-Gonzalez, S. Coulombe, and J.-L. Meunier, "The effect of carbon input on the morphology and attachment of carbon nanotubes grown directly from stainless steel," *Carbon*, vol. 63, pp. 348–357, Nov. 2013.

[139] L. Camilli *et al.*, "The synthesis and characterization of carbon nanotubes grown by chemical vapor deposition using a stainless steel catalyst," *Carbon*, vol. 49, no. 10, pp. 3307–3315, Aug. 2011.
[140] C. Du and N. Pan, "CVD growth of carbon nanotubes directly on nickel substrate," *Materials Letters*, vol. 59, no. 13, pp. 1678–1682, Jun. 2005.
[141] P. Romero, R. Oro, M. Campos, J. M. Torralba, and R. Guzman de Villoria, "Simultaneous synthesis of vertically aligned carbon nanotubes and amorphous carbon thin films on stainless steel," *Carbon*, vol. 82, pp. 31–38, Feb. 2015.
[142] A. Dahal and M. Batzill, "Graphene–nickel interfaces: a review," *Nanoscale*, vol. 6, no. 5, p. 2548, 2014.
[143] M. L. Toebes, J. H. Bitter, A. J. Van Dillen, and K. P. de Jong, "Impact of the structure and reactivity of nickel particles on the catalytic growth of carbon nanofibers," *Catalysis Today*, vol. 76, no. 1, pp. 33–42, 2002.
[144] S. Motojima and Q. Chen, "Three-dimensional growth mechanism of cosmo-mimetic carbon microcoils obtained by chemical vapor deposition," *Journal of Applied Physics*, vol. 85, no. 7, p. 3919, 1999.
[145] A. Shaikjee and N. J. Coville, "The effect of substituted alkynes on nickel catalyst morphology and carbon fiber growth," *Carbon*, vol. 50, no. 3, pp. 1099–1108, Mar. 2012.
[146] C. Park and M. A. Keane, "Catalyst support effects in the growth of structured carbon from the decomposition of ethylene over nickel," *Journal of Catalysis*, vol. 221, no. 2, pp. 386–399, Jan. 2004.
[147] C. Park and R. T. K. Baker, "Carbon deposition on iron–nickel during interaction with ethylene–hydrogen mixtures," *Journal of Catalysis*, vol. 179, no. 2, pp. 361–374, 1998.
[148] S. Lim, S.-H. Yoon, Y. Korai, and I. Mochida, "Selective synthesis of thin carbon nanofibers: I. Over nickel–iron alloys supported on carbon black," *Carbon*, vol. 42, no. 8–9, pp. 1765–1781, Jan. 2004.
[149] L. I. Nasibulina *et al.*, "Direct synthesis of carbon nanofibers on the surface of copper powder," *Carbon*, vol. 48, no. 15, pp. 4559–4562, Dec. 2010.
[150] R. John, A. Ashokreddy, C. Vijayan, and T. Pradeep, "Single-and few-layer graphene growth on stainless steel substrates by direct thermal chemical vapor deposition," *Nanotechnology*, vol. 22, no. 16, p. 165701, 2011.
[151] Y. Xue *et al.*, "Synthesis of large-area, few-layer graphene on iron foil by chemical vapor deposition," *Nano Research*, vol. 4, no. 12, pp. 1208–1214, Sep. 2011.
[152] A. Röthlisberger, M. Seita, A. Reiser, E. Shawat, R. Spolenak, and G. D. Nessim, "Investigating the mechanism of collective bidirectional growth of carbon nanofiber carpets on metallic substrates," *Carbon*, vol. 63, pp. 498–507, Nov. 2013.
[153] H. J. Grabke, R. Krajak, and J. C. Nava Paz, "On the mechanism of catastrophic carburization:'metal dusting,'" *Corrosion Science*, vol. 35, no. 5, pp. 1141–1150, 1993.
[154] D. J. Young, J. Zhang, C. Geers, and M. Schütze, "Recent advances in understanding metal dusting: A review," *Materials and Corrosion*, vol. 62, no. 1, pp. 7–28, Jan. 2011.

[155] Z. Zeng and K. Natesan, "Relationship between the Growth of Carbon Nanofilaments and Metal Dusting Corrosion," *Chemistry of Materials*, vol. 17, no. 14, pp. 3794–3801, Jul. 2005.
[156] J. Zhang and D. J. Young, "Coking and Dusting of Fe–Ni Alloys in CO–H2–H2O Gas Mixtures," *Oxidation of Metals*, vol. 70, no. 3–4, pp. 189–211, Oct. 2008.
[157] E. Pippel, J. Woltersdorf, and R. Schneider, "Micromechanisms of metal dusting on Fe-base and Ni-base alloys," *Materials and corrosion*, vol. 49, no. 5, pp. 309–316, 1998.
[158] C. M. Chun, T. A. Ramanarayanan, and J. D. Mumford, "Relationship between coking and metal dusting," *Materials and Corrosion*, vol. 50, no. 11, pp. 634–639, 1999.
[159] Z. Yu *et al.*, "Large-scale synthesis of carbon nanofibers on Ni-Fe-Al hydrotalcite derived catalysts II effect of Ni Fe composition on CNF synthesis from ethylene and carbon monoxide," vol. 338, pp. 147–158, 2008.
[160] E. Pippel, J. Woltersdorf, and H. J. Grabke, "Microprocesses of metal dusting on iron-nickel alloys and their dependence on the alloy composition," *Materials and Corrosion*, vol. 54, no. 10, pp. 747–751, Oct. 2003.
[161] J. Zhang, A. Schneider, and G. Inden, "Characterisation of the coke formed during metal dusting of iron in CO–H2–H2O gas mixtures," *Corrosion Science*, vol. 45, no. 6, pp. 1329–1341, Jun. 2003.
[162] J. Zhang, P. Munroe, and D. J. Young, "Microprocesses in nickel accompanying metal dusting," *Acta Materialia*, vol. 56, no. 1, pp. 68–77, Jan. 2008.
[163] Q. Wei, E. Pippel, J. Woltersdorf, S. Bakshi, and H. J. Grabke, "Orientation dependence of metal dusting nanoprocesses on nickel single crystals." .
[164] C. M. Chun, J. D. Mumford, and T. A. Ramanarayanan, "Mechanisms of Metal Dusting Corrosion of Iron," *Journal of The Electrochemical Society*, vol. 149, no. 7, p. B348, 2002.
[165] G. D. Nessim *et al.*, "Low Temperature Synthesis of Vertically Aligned Carbon Nanotubes with Electrical Contact to Metallic Substrates Enabled by Thermal Decomposition of the Carbon Feedstock," *Nano Letters*, vol. 9, no. 10, pp. 3398–3405, Oct. 2009.
[166] A. C. Ferrari and D. M. Basko, "Raman spectroscopy as a versatile tool for studying the properties of graphene," *Nature Nanotechnology*, vol. 8, no. 4, pp. 235–246, Apr. 2013.
[167] J. Moulder, W. Stickle, P. Sobol, and K. Bomben, *Handbook of X-Ray Photoelectron Spectroscopy*. P.-E. Corporation, 1992.
[168] M. Weisenberger *et al.*, "The effect of graphitization temperature on the structure of helical-ribbon carbon nanofibers," *Carbon*, vol. 47, no. 9, pp. 2211–2218, Aug. 2009.
[169] M. Kawaguchi, K. Nozaki, S. Motojima, and H. Iwanaga, "A growth mechanism of regularly coiled carbon fibers through acetylene pyrolysis," *Journal of Crystal Growth*, vol. 118, no. 3, pp. 309–313, 1992.
[170] S. Motojima, M. Kawaguchi, K. Nozaki, and H. Iwanaga, "Growth of regularly coiled carbon filaments by Ni catalyzed pyrolysis of acetylene, and their morphology and extension characteristics," *Applied Physics Letters*, vol. 56, no. 4, p. 321, 1990.

[171] A. Grossmann, W. Erley, and H. Ibach, “Adsorbate-induced surface stress and surface reconstruction: oxygen, sulfur and carbon on Ni(111),” *Surface Science*, vol. 337, pp. 183–189, 1995.
[172] D. Sander, U. Linke, and H. Ibach, “Adsorbate-induced surface stress: sulfur, oxygen and carbon on Ni(100),” *Surface Science*, vol. 272, pp. 318–325, 1992.
[173] C. Klink, I. Stensgaard, F. Besenbacher, and E. L\a egsgaard, “An STM study of carbon-induced structures on Ni (111): evidence for a carbidic-phase clock reconstruction,” *Surface science*, vol. 342, no. 1, pp. 250–260, 1995.
[174] H. Meltzman, D. Chatain, D. Avizemer, T. M. Besmann, and W. D. Kaplan, “The equilibrium crystal shape of nickel,” *Acta Materialia*, vol. 59, no. 9, pp. 3473–3483, May 2011.
[175] J.-S. Hong, W. Jo, K.-J. Ko, N. M. Hwang, and D.-Y. Kim, “Equilibrium shape of nickel crystal,” *Philosophical Magazine*, vol. 89, no. 32, pp. 2989–2999, Nov. 2009.
[176] S. Hofmann, G. Csányi, A. Ferrari, M. Payne, and J. Robertson, “Surface Diffusion: The Low Activation Energy Path for Nanotube Growth,” *Physical Review Letters*, vol. 95, no. 3, Jul. 2005.
[177] S. Hofmann, C. Ducati, J. Robertson, and B. Kleinsorge, “Low-temperature growth of carbon nanotubes by plasma-enhanced chemical vapor deposition,” *Applied Physics Letters*, vol. 83, no. 1, p. 135, 2003.
[178] I. Denysenko and K. Ostrikov, “Ion-assisted precursor dissociation and surface diffusion: Enabling rapid, low-temperature growth of carbon nanofibers,” *Applied Physics Letters*, vol. 90, no. 25, p. 251501, 2007.
[179] S. Hong, Y.-H. Shin, and J. Ihm, “Crystal shape of a nickel particle related to carbon nanotube growth,” *Japanese journal of applied physics*, vol. 41, no. 10R, p. 6142, 2002.
[180] L. Baraton *et al.*, “On the mechanisms of precipitation of graphene on nickel thin films,” *EPL (Europhysics Letters)*, vol. 96, no. 4, p. 46003, Nov. 2011.
[181] C. Pham-Huu *et al.*, “About the octopus-like growth mechanism of carbon nanofibers over graphite supported nickel catalyst,” *Journal of Catalysis*, vol. 240, no. 2, pp. 194–202, Jun. 2006.
[182] P. Romero, R. Oro, M. Campos, J. M. Torralba, and R. Guzman de Villoria, “Vertically Aligned Carbon Nanotube-Carbon Film Nanostructures for Nanoegineered,” presented at the Carbon, Dresden, Germany, 2015.
[183] P. Romero, R. Oro, M. Campos, J. M. Torralba, and R. Guzman de Villoria, “Híbrido de Nanotubos de Carbono Verticalmente Alineados y Película de Carbono y su potencial uso en Mate-riales Compuestos,” presented at the XI Congreso Nacional de Materiales Compuestos, Matcomp’15, Madrid, Spain, 2015.
[184] I. Olefjord and L. Nyborg, “Surface Analysis of Gas Atomized Ferritic Steel Powder,” *Powder Metallurgy*, vol. 28, no. 4, pp. 237–243, 1985.
[185] I. Mészáros and J. Prohászka, “Magnetic investigation of the effect of α′-martensite on the properties of austenitic stainless steel,” *Journal of Materials Processing Technology*, vol. 161, no. 1–2, pp. 162–168, Apr. 2005.
[186] E. Almanza and L. E. Murr, “A comparison of sensitization kinetics in 304 and 316 stainless steels,” *Journal of materials science*, vol. 35, no. 13, pp. 3181–3188, 2000.
[187] H. J. T. Ellingham, “Transactions and communcations,” *J Soc Chem Ind*, vol. 63, no. 125.

[188] R. Oro, M. Campos, C. Gierl-Mayer, H. Danninger, and J. M. Torralba, "New Alloying Systems for Sintered Steels: Critical Aspects of Sintering Behavior," *Metallurgical and Materials Transactions A*, vol. 46, no. 3, pp. 1349–1359, Mar. 2015.

[189] E. Hryha, E. Dudrova, and L. Nyborg, "On-line control of processing atmospheres for proper sintering of oxidation-sensitive PM steels," *Journal of Materials Processing Technology*, vol. 212, no. 4, pp. 977–987, Apr. 2012.

[190] D. Chasoglou, E. Hryha, and L. Nyborg, "Effect of process parameters on surface oxides on chromium-alloyed steel powder during sintering," *Materials Chemistry and Physics*, vol. 138, no. 1, pp. 405–415, Feb. 2013.

[191] F. Bonnet, F. Ropital, Y. Berthier, and P. Marcus, "Filamentous carbon formation caused by catalytic metal particles from iron oxide," *Materials and Corrosion*, vol. 54, no. 11, pp. 870–880, Nov. 2003.

[192] M. Bedewy, E. R. Meshot, H. Guo, E. A. Verploegen, W. Lu, and A. J. Hart, "Collective Mechanism for the Evolution and Self-Termination of Vertically Aligned Carbon Nanotube Growth," *The Journal of Physical Chemistry C*, vol. 113, no. 48, pp. 20576–20582, Dec. 2009.

[193] P. Szakalos, R. Pettersson, and S. Hertzman, "An active corrosion mechanism for metal dusting on 304L stainless steel," *Corrosion Science*, vol. 44, no. 10, pp. 2253–2270, 2002.

[194] P. Szakálos, "Mechanisms and driving forces of metal dusting," *Materials and Corrosion*, vol. 54, no. 10, pp. 752–762, Oct. 2003.

[195] X. Li *et al.*, "Transfer of Large-Area Graphene Films for High-Performance Transparent Conductive Electrodes," *Nano Letters*, vol. 9, no. 12, pp. 4359–4363, Dec. 2009.

[196] F. Pizzocchero *et al.*, "Non-destructive electrochemical graphene transfer from reusable thin-film catalysts," *Carbon*, vol. 85, pp. 397–405, Apr. 2015.

[197] L. P. Biró and P. Lambin, "Grain boundaries in graphene grown by chemical vapor deposition," *New Journal of Physics*, vol. 15, no. 3, p. 35024, Mar. 2013.

[198] Q. Yu *et al.*, "Control and characterization of individual grains and grain boundaries in graphene grown by chemical vapour deposition," *Nature Materials*, vol. 10, no. 6, pp. 443–449, Jun. 2011.

[199] P. Romero, P. A. Postigo, E. Baquedano, J. Martinez, A. Bosca, and R. Guzman de Villoria, "Controlled synthesis of nanocrystalline glass-like carbon thin films with tuneable electrical and optical properties," *Chemical Engineering Journal*, Apr. 2016.

[200] A. C. Ferrari and J. Robertson, "Interpretation of Raman spectra of disordered and amorphous carbon," *Physical Review B*, vol. 61, no. 20, pp. 14095–14107, 2000.

[201] A. Sadezky, H. Muckenhuber, H. Grothe, R. Niessner, and U. Pöschl, "Raman microspectroscopy of soot and related carbonaceous materials: Spectral analysis and structural information," *Carbon*, vol. 43, no. 8, pp. 1731–1742, Jul. 2005.

[202] A. Cuesta, P. Dhamelincourt, J. Laureyns, M. A. alonso, and J. M. D. Tascón, "Raman Microprobe studies on carbon materials," *Carbon*, vol. 32, no. 8, pp. 1523–1532, 1994.

[203] L. Liang-Hsun, L. Huei-Cheng, S. Sham-Tsong, Y. Tsong-Jen, and L. Hung-Yi, "Effects of Ethylene-Ammonia Mixtures on Thermal Chemical vapor

deposition rates and mmicrostructures of carbon films," *ECS Journal of Solid State Science and Technology*, vol. 2, no. 11, 2013.
[204] P. J. F. Harris, "Fullerene-like models for microporous carbon," *Journal of Materials Science*, vol. 48, no. 2, pp. 565–577, Jan. 2013.
[205] C. L. Burket, R. Rajagopalan, and H. C. Foley, "Overcoming the barrier to graphitization in a polymer-derived nanoporous carbon," *Carbon*, vol. 46, no. 3, pp. 501–510, Mar. 2008.
[206] L. A. Pesin, "Review Structure and properties of glass-like carbon," *Journal of Materials Science*, vol. 37, no. 1, pp. 1–28, 2002.
[207] C. Thomsen and S. Reich, "Double resonant Raman scattering in graphite," *Physical Review Letters*, vol. 85, no. 24, p. 5214, 2000.
[208] P. May *et al.*, "Signature of the two-dimensional phonon dispersion in graphene probed by double-resonant Raman scattering," *Physical Review B*, vol. 87, no. 7, Feb. 2013.
[209] A. C. Ferrari *et al.*, "Raman Spectrum of Graphene and Graphene Layers," *Physical Review Letters*, vol. 97, no. 18, Oct. 2006.
[210] R. Pfeiffer, H. Kuzmany, P. Knoll, S. Bokova, N. Salk, and B. Günther, "Evidence for trans-polyacetylene in nano-crystalline diamond films," *Diamond and Related Materials*, vol. 12, no. 3–7, pp. 268–271, Mar. 2003.
[211] A. C. Ferrari and J. Robertson, "Origin of the 1 1 5 0 − cm − 1 Raman mode in nanocrystalline diamond," *Physical Review B*, vol. 63, no. 12, Mar. 2001.
[212] J. Wagner, M. Ramsteiner, C. Wild, and P. Koidl, "Resonant Raman scattering of amorphous carbon and polycrystalline diamond films," *Physical Review B*, vol. 40, no. 3, p. 1817, 1989.
[213] V. N. Vasilets *et al.*, "Characterization of doped diamond-like carbon films deposited by hot wire plasma sputtering of graphite," *Applied Physics A*, vol. 79, no. 8, Dec. 2004.
[214] B. Dischler, "Hard carbon coatings with low optical absorption," *Applied Physics Letters*, vol. 42, no. 8, p. 636, 1983.
[215] M. E. Schmidt, C. Xu, M. Cooke, H. Mizuta, and H. M. H. Chong, "Metal-free plasma-enhanced chemical vapor deposition of large area nanocrystalline graphene," *Materials Research Express*, vol. 1, no. 2, p. 25031, May 2014.
[216] Z. Luo *et al.*, "Effect of Substrate Roughness and Feedstock Concentration on Growth of Wafer-Scale Graphene at Atmospheric Pressure," *Chemistry of Materials*, vol. 23, no. 6, pp. 1441–1447, Mar. 2011.
[217] W. T. Tsen *et al.*, "Tailoring Electrical Transport Across Grain Boundaries in Polycrystalline Graphene," *Science*, vol. 336, no. 6085, pp. 1143–1146, 2012.
[218] Y. Hao *et al.*, "Probing Layer Number and Stacking Order of Few-Layer Graphene by Raman Spectroscopy," *Small*, vol. 6, no. 2, pp. 195–200, Jan. 2010.
[219] I. Vlassiouk *et al.*, "Large scale atmospheric pressure chemical vapor deposition of graphene," *Carbon*, vol. 54, pp. 58–67, Apr. 2013.
[220] I. Vlassiouk *et al.*, "Role of Hydrogen in Chemical Vapor Deposition Growth of Large Single-Crystal Graphene," *ACS Nano*, vol. 5, no. 7, pp. 6069–6076, Jul. 2011.
[221] H. Qian, E. S. Greenhalgh, M. S. P. Shaffer, and A. Bismarck, "Carbon nanotube-based hierarchical composites: a review," *Journal of Materials Chemistry*, vol. 20, no. 23, p. 4751, 2010.

[222] K. Mukai *et al.*, "Highly Conductive Sheets from Millimeter-Long Single-Walled Carbon Nanotubes and Ionic Liquids: Application to Fast-Moving, Low-Voltage Electromechanical Actuators Operable in Air," *Advanced Materials*, vol. 21, no. 16, pp. 1582–1585, 2009.
[223] F. C. Cowlard and J. C. Lewis, "Vitreous carbon—a new form of carbon," *Journal of Materials Science*, vol. 2, no. 6, pp. 507–512, 1967.
[224] J. C. Lewis, B. Redfern, and F. C. Cowlard, "Vitreous carbon as a crucible material for semiconductors," *Solid-State Electronics*, vol. 6, no. 3, p. 251–IN4, 1963.
[225] M. Inagaki, C.-R. Park, J. Skowronski, and A. Morawski, "Glass-like Carbon Spheres—Activation, Porosity and Application Possibilities," *Adsorption Science & Technology*, vol. 26, no. 10, pp. 735–787, 2008.
[226] K. Kusakabe and M. Maruyama, "Magnetic nanographite," *Physical Review B*, vol. 67, no. 9, Mar. 2003.
[227] C. Wang and D. Diao, "Magnetic behavior of graphene sheets embedded carbon film originated from graphene nanocrystallite," *Applied Physics Letters*, vol. 102, no. 5, p. 52402, 2013.
[228] C. Wang, X. Zhang, and D. Diao, "Nanosized graphene crystallite induced strong magnetism in pure carbon films," *Nanoscale*, vol. 7, no. 10, pp. 4475–4481, 2015.
[229] A. V. Rode *et al.*, "Unconventional magnetism in all-carbon nanofoam," *Physical Review B*, vol. 70, no. 5, Aug. 2004.
[230] R. L. McCreery, "Advanced Carbon Electrode Materials for Molecular Electrochemistry," *Chemical Reviews*, vol. 108, no. 7, pp. 2646–2687, Jul. 2008.
[231] K. K. Kim *et al.*, "Enhancing the conductivity of transparent graphene films via doping," *Nanotechnology*, vol. 21, no. 28, p. 285205, Jul. 2010.
[232] N. McEvoy *et al.*, "Synthesis and analysis of thin conducting pyrolytic carbon films," *Carbon*, vol. 50, no. 3, pp. 1216–1226, Mar. 2012.
[233] T. Kaplas and Y. Svirko, "Direct deposition of semitransparent conducting pyrolytic carbon films," *Journal of Nanophotonics*, vol. 6, no. 1, pp. 61703–61703, 2012.
[234] T. Cui *et al.*, "Synthesis of nitrogen-doped carbon thin films and their applications in solar cells," *Carbon*, vol. 49, no. 15, pp. 5022–5028, Dec. 2011.
[235] T. Cui *et al.*, "Hybrid graphene/amorphous carbon films with tadpole-like structures for high-performance photovoltaic applications," *RSC Advances*, vol. 3, no. 44, p. 22295, 2013.
[236] S. H. Vijapur, D. Wang, and G. G. Botte, "The growth of transparent amorphous carbon thin films from coal," *Carbon*, vol. 54, pp. 22–28, Apr. 2013.
[237] T. Gao *et al.*, "Hierarchical Graphene/Metal Grid Structures for Stable, Flexible Transparent Conductors," *ACS Nano*, p. 150511133437001, May 2015.
[238] B. Jalvo, J. Santiago-Morales, P. Romero, R. Guzman de Villoria, and R. Rosal, "Microbial colonisation of transparent glass-like carbon films triggered by a reversible radiation-induced hydrophobic to hydrophilic transition," *RSC Adv.*, vol. 6, no. 55, pp. 50278–50287, 2016.
[239] Q. G. Jiang, Z. M. Ao, D. W. Chu, and Q. Jiang, "Reversible Transition of Graphene from Hydrophobic to Hydrophilic in the Presence of an Electric Field," *The Journal of Physical Chemistry C*, vol. 116, no. 36, pp. 19321–19326, 2012.

[240] J. Yang, Z. Zhang, X. Men, X. Xu, and X. Zhu, "Reversible Superhydrophobicity to Superhydrophilicity Switching of a Carbon Nanotube Film via Alternation of UV Irradiation and Dark Storage," *Langmuir*, vol. 26, no. 12, pp. 10198–10202, Jun. 2010.
[241] Y. Zhou *et al.*, "Control over the wettability of amorphous carbon films in a large range from hydrophilicity to super-hydrophobicity," *Applied Surface Science*, vol. 253, no. 5, pp. 2690–2694, Dec. 2006.
[242] Y. Chen, X.-L. Gong, and J.-G. Gai, "Progress and Challenges in Transfer of Large-Area Graphene Films," *Advanced Science*, vol. 3, no. 8, p. 1500343, Aug. 2016.
[243] A. V. Zaretski and D. J. Lipomi, "Processes for non-destructive transfer of graphene: widening the bottleneck for industrial scale production," *Nanoscale*, vol. 7, no. 22, pp. 9963–9969, 2015.
[244] C. Kim, J. Y. Woo, J. Choi, J. Park, and C.-S. Han, "Direct transfer of graphene without the removal of a metal substrate using a liquid polymer," *Scripta Materialia*, vol. 66, no. 8, pp. 535–537, Apr. 2012.
[245] E. H. Lock *et al.*, "High-Quality Uniform Dry Transfer of Graphene to Polymers," *Nano Letters*, vol. 12, no. 1, pp. 102–107, Jan. 2012.
[246] T. L. Chen, D. S. Ghosh, M. Marchena, J. Osmond, and V. Pruneri, "Nanopatterned Graphene on a Polymer Substrate by a Direct Peel-off Technique," *ACS Applied Materials & Interfaces*, vol. 7, no. 10, pp. 5938–5943, Mar. 2015.
[247] S. Y. Yang *et al.*, "Metal-Etching-Free Direct Delamination and Transfer of Single-Layer Graphene with a High Degree of Freedom," *Small*, vol. 11, no. 2, pp. 175–181, Jan. 2015.
[248] G. J. Fechine *et al.*, "Direct dry transfer of chemical vapor deposition graphene to polymeric substrates," *Carbon*, vol. 83, pp. 224–231, 2015.
[249] W. Jung, D. Kim, M. Lee, S. Kim, J.-H. Kim, and C.-S. Han, "Ultraconformal Contact Transfer of Monolayer Graphene on Metal to Various Substrates," *Advanced Materials*, vol. 26, no. 37, pp. 6394–6400, Oct. 2014.
[250] B. N. Chandrashekar *et al.*, "Roll-to-Roll Green Transfer of CVD Graphene onto Plastic for a Transparent and Flexible Triboelectric Nanogenerator," *Advanced Materials*, vol. 27, no. 35, pp. 5210–5216, Sep. 2015.
[251] Y. Wang *et al.*, "Electrochemical Delamination of CVD-Grown Graphene Film: Toward the Recyclable Use of Copper Catalyst," *ACS Nano*, vol. 5, no. 12, pp. 9927–9933, Dec. 2011.
[252] L. Gao *et al.*, "Repeated growth and bubbling transfer of graphene with millimetre-size single-crystal grains using platinum," *Nature Communications*, vol. 3, p. 699, Feb. 2012.
[253] T. Ciuk *et al.*, "Properties of Chemical Vapor Deposition Graphene Transferred by High-Speed Electrochemical Delamination," *The Journal of Physical Chemistry C*, vol. 117, no. 40, pp. 20833–20837, Oct. 2013.
[254] C. T. Cherian, F. Giustiniano, I. Martin-Fernandez, H. Andersen, J. Balakrishnan, and B. Özyilmaz, "'Bubble-Free' Electrochemical Delamination of CVD Graphene Films," *Small*, vol. 11, no. 2, pp. 189–194, Jan. 2015.
[255] X. Wang *et al.*, "Direct Delamination of Graphene for High-Performance Plastic Electronics," *Small*, vol. 10, no. 4, pp. 694–698, Feb. 2014.